Flow assisted assembly of multilayer colloidal crystals studied using confocal laser scanning microscopy

by

Laura T. Shereda

A dissertation submitted in the partial fulfillment
of the requirements for the degree of
Doctor of Philosophy
(Chemical Engineering)
in The University of Michigan
2010

Professor Ronald G. Larson, Co-Chair
Professor Michael J. Solomon, Co-Chair
Professor Nicholas A. Kotov
Assistant Professor Max Shtein

To my family for their love and support

Acknowledgements:

Even though graduate school at times feels lonely, a PhD thesis is rarely conducted in a vacuum. Over the past five years I have had the opportunity to work with many extraordinary people -both inside and outside the department - and have been blessed with a tremendous amount of support. Many people have contributed to my success both academically and through their support and I am grateful for the opportunity to thank them now.

My individual relationships with my advisors have had a profound effect on me. Ron hired me to work in his lab in 2002. From this project and the independence it provided, I found my love for research and the confidence that led me to apply to graduate school. He appreciated my sense of humor and never seemed to mind when I walked into his office unannounced with a question. When I became ill as an undergrad, he reacted with the concern of a parent as opposed to the distance expected from a professor. Ron is a brilliant, kind, and compassionate person, and I am very fortunate to have had the opportunity to work closely with him for the last several years.

Through the last five years, Mike has become a mentor to me. Besides being an outstanding professor, I have always admired his ethics and appreciated his professionalism and the high standards he held me too (though not always at the time). Mike embraced independence and my early-morning work schedule and appreciated my sense of humor and the person I am. When I spoke at conferences he introduced me to his

colleagues and the pride in the work I had done as well as the researcher I had become were evident. These were proud moments for me. In my time here, Mike taught me not only how to be a good researcher but about believing in myself, taking pride in my work, and being a good person with strong convictions.

I would also like to extend my most sincere thanks to Dr. Joseph McCune MD. I attribute a good amount of my success to him as he was instrumental in helping me to stay healthy, allowing me to achieve my dreams. He always emphasized my strengths and always made time for me whenever I needed anything, even if the situation was not critical. Thank you for going above and beyond what could be expected of a physician – I am forever grateful for your support.

The Brown family – Elizabeth, Dave, Genevieve, Isaac and Vivian have also helped me to succeed. Elizabeth always had time for me and helped me put my frustrations into perspective. I also thank the kids for the pictures they made for me to hang at my desk.

Without my best friend, Mike Anderson, I probably would not have made it this far or at least would not have been nearly as successful. He was there for me whenever I needed to talk or my experiments weren't working or I felt like I wasn't good enough. He listened to all of my rants about things breaking, experiments not working, and dealing with coworkers. He helped me to believe that I was smart and strong and could make me laugh at the worst of times. Additionally, he was always the first one to help me celebrate my successes.

Finally, I would like to thank my family. I want to thank my parents for pushing me to discover my true potential, passions, and realize my dreams. They have supported

me through my struggles even though they didn't always understand the choices I made. I always wanted to follow in my dads footsteps and I know is secretly pleased that one of his kids became an engineer. I am very proud

of my brothers, and sister – Rob, George, and Mary – for their academic pursuits and thank them for their support. Finally, I would also like to thank my dog Libby for always being happy to see me and for sitting with me while I wrote my thesis .

There are many more people who have contributed significantly to my success and I thank you all.

TABLE OF CONTENTS

LIST OF FIGURES

LIST OF TABLES

LIST OF APPENDICES

ABSTRACT

Flow assisted assembly of multilayer colloidal crystals studied using confocal laser scanning microscopy

by

Laura T. Shereda

Co-Chairs: Ronald G. Larson and Michael J. Solomon

Colloidal crystals are highly ordered particle arrays with potential applications including sensors, optical switches, and photonic materials. For production on an industrially viable scale, a process must be developed to form crystals with low defect densities, good long range order, and favorable kinetics.

Application of a field to a concentrated colloidal suspension accelerates crystal formation. Ackerson et al.[1] established that systems with stress-based Peclet numbers above one resulted in crystal formation. We investigate formation of colloidal crystals by studying structural changes that occur upon shearing using confocal microscopy. Charge-stabilized poly(methylmethacrylate) particles ($\Phi = 0.35$) suspended in dioctyl phthalate were used for experiments. After application of shear, assembled structures were immobilized by UV exposure. The full sample thickness was imaged using confocal

microscopy. Particle centroids were located in 3D by means of image processing[2] and local crystallinity was quantified by application of local bond order parameter criteria[3]. We present microstructural analysis of structures formed by both spin coating and uniform shear flow.

Spin coating produces spatiotemporal variation in the ordering of concentrated colloidal dispersions that is a universal function of the local reduced critical stress and macroscopic strain. Samples produced at Peclet numbers greater than one and macroscopic strains above two resulted in crystal formation. A plot of the cryrstalline fraction versus Peclet number yielded a sharp order to disorder transition at Peclet number of order unity. The effect of volume fraction on the Peclet number theory was studied. Results indicated that the theory applied to volume fractions within the crystalline regime.

Strain requirements for crystal formation of samples undergoing step strain deformation in a parallel plate geometry were investigated by applying stains of 1-300 to samples with fixed gaps of 150μm. We found the velocity profile to be non-linear across the gap. This inhomogeneity was strongly correlated with the movement of the crystalline boundary. A strain of 160 was required for full sample crystallization. The movement of the crystalline boundary was modeled as a 1-D crystallization and fitted as two linear regions. Fundamental knowledge gained from these studies will allow shear processes to be evaluated for industrial use.

1. Ackerson, B.J., *Shear induced order in equilibrium colloidal liquids*, in *Physica A*. 1991. p. 15-30.
2. Cerda, J.J., et al., *Shear effects on crystal nucleation in colloidal suspensions*, in *Physical Review E*. 2008. p. 16.

3. Crocker, J.C., D.G. Grier, and Ug, *Methods of digital video microscopy for colloidal studies.* Journal of Colloid and Interface Science, 1996. **179**(1): p. 298-310.
4. tenWolde, P.R., M.J. RuizMontero, and D. Frenkel, *Numerical calculation of the rate of crystal nucleation in a Lennard-Jones system at moderate undercooling.* Journal of Chemical Physics, 1996. **104**(24): p. 9932-9

CHAPTER 1

Introduction

1.1 Colloidal suspensions

Colloidal suspensions have been used to model atomic and molecular systems because they exhibit many of the thermodynamic and dynamic properties and phase transitions that occur in those systems, however, significantly longer relaxation times make colloids much easier to study than atomic systems[4]. Colloidal particles are generally defined as particles with a diameter on the scale of a few nanometers to a few microns. The size range is distinguished because when dispersed in solution these particles undergo Brownian motion and interact through attractive or repulsive potentials [5]. Brownian motion is important because this random motion allows particles to sample configuration space.

Colloidal particle systems are referred to as “soft matter” because their physical states are easily perturbed by thermal fluctuations on the order of the thermal energy present at room temperature. Because of their size and time scales colloidal systems are ideal for understanding phase changes including the freezing, melting, and glass transitions[6]. They also provide insight into phenomena such as gelation[7].

Colloidal systems are of both commercial and academic interest. Colloidal suspensions allow production of materials with unique textures and rheological properties. Colloids are found in many common household materials including adhesives[8], ceramic materials[9], foods[7], personal care products, toothpaste[10] and paint. /Ordered structures of colloids introduce additional potential applications[11, 12]. High quality colloidal crystals can be used in photonic materials, microelectronics, chemical sensors, anti-reflection coatings [13, 14], and synthetic opals. Particles in the colloidal size range are important building blocks for materials where the goal is to block a specific wavelength of light. By varying the interparticle spacing as well as the particle size, the wavelength of light reflected can be shifted preferentially, resulting in properties such as color changes and the creation of tunable photonic materials[15]. Ordered nanoparticles result in Bragg interference as opposed to the desired photonic effect.

Different crystal qualities and defect densities are required for various applications. Sensing can be achieved using samples that simply exhibit Bragg peaks or visible color changes, however, for photonic materials the defect density must be much lower. For example, in optical switching, the defect density governs the maximum switching speed. Current switches by Sato et al. [16] can switch states on the order of tens of microseconds, however, the many defects slow the process down. For creation of digital displays, switching needs to happen significantly faster.

1.2 Colloidal forces and interparticle interactions

The most basic of colloidal systems are hard sphere suspensions. In hard sphere systems the particles do not interact with one other and are infinitely repulsive on contact.

That is, they have the property of no overlap. The phase behaviors of the system are determined solely by the colloid volume fraction and at high volume fractions above the freezing transition ($\Phi > 0.494$) results in crystallization conversion to crystalline phases increases the number of possible particle packing configurations[17]. The phase diagram for crystallization of hard sphere systems has been extensively tested[18]. However, generally colloids in solution interact with one another. Attractive interactions result in gelation or aggregation and repulsive interactions can lead to crystalline ordering. Phase diagrams for repulsive spheres are different than those for hard spheres, with crystallization occurring at lower volume fractions and phases, some transient, not seen in hard sphere crystallization occur[19] Suspensions are affected by many forces including hydrodynamic, diffusive, gravitational, and electrostatic forces[20].

Because of their small size, when colloids are dispersed in solution, the large surface to volume ratio of the particles leads to a large contact areas with the solvent. This makes solvent and interparticle interactions a significant factor in determining the behavior of a colloidal suspension[21]. Additionally, excluded volume interactions – which are present in both hard sphere and repulsive sphere systems - occur in colloids with short-range repulsive interactions[22]. These interactions prevent particles from penetrating one another and prevent particle deformation, though in some systems they cause deformation.

Interparticle forces can be either attractive or repulsive in nature with attractive forces generally leading to aggregation. Each particle has its own characteristic potential which is a function of the distance of particle separation[20]. The potentials of particles in colloidal systems are on the order of k_BT[23]. The nature of the interactions present

determine the physical state of the suspensions for example aggregation or gelation in attractive systems and crystals in repulsive systems[24]. Additionally, a refractive index mismatch between particles and solvent may result in aggregation of particles due to van der Waals forces.

Brownian motion, the random motion of colloids in a fluid due to thermal effects, also exerts a force on the particles. The combined effect of these forces leads to the characteristic physical behavior of the system. Particle interactions can be tuned by increasing the number of free ions in the system, achieved by addition of organic salts to the solvent[25].

1.3 Colloidal crystallization

Colloidal dispersions display equilibrium fluid-crystal transitions [26]. The character of these transitions, including coexistence boundaries and nucleation rates, has been extensively compared to predictions of statistical thermodynamics [27]. Colloidal crystals are highly ordered arrays of particles which can be formed over a long range (to about a centimeter)[28]. Crystallization is a structural transition that occurs because under Brownian motion particles sample space outside of their lattice positions to form the lowest possible free energy state. Particles in ordered configurations have more free volume than disordered ones[6]. The contribution of polydispersity, finite size effects and interaction potential on crystallization have been explored[29].

Below a critical volume fraction, colloidal suspensions maintain a fluid-like structure at equilibrium. The degree to which crystals will form depends on the strength of the repulsive forces between the particles[i]. When repulsive forces are present in a

colloidal system, crystals form from suspensions with volume fractions below the hard sphere coexistence region. One way to address this point is to consider the effective volume fraction. The effective volume fraction is calculated by defining a new particle radius, r',

$$r' = r + K^{-1} \tag{5}$$

where K^{-1} is the Debye length and r is the radius determined by SEM. The Debye length is the scale over which particles screen out electric fields. The Debye length is calculated using conductivity measurements of the solvent. The effective volume fraction is calculated as usual using the scaled r' in place of r. Organic salts can be added to screen charges[25].

1.4 Field-assisted assembly

Methods for colloidal crystal fabrication include both top-down lithographical processing and methods of self and field-assisted assembly. Self-assembly – or equilibrium phase transition - processes are parallel, high throughput ways to deposit particles[30] that result in stable, low free energy structures[31]. In flows of suspensions of repulsive hard spheres, structure formation is determined by the balance among Brownian motion, hydrodynamic forces, and interparticle forces[32]. Methods of self-assembly include sedimentation[18], vertical deposition[33], magnetic[34, 35], and electric field assisted assembly[36], and flow-assisted methods such as shear flow[37] and spin coating[38]. Application of a field tends to accelerate crystallization, however,

many methods of self-assembly are limited by time scales, size restrictions, and inability to control the properties of 3-D structures formed. In the general case, colloidal crystallization is driven by flows with velocity fields that vary in space and time. In these systems, microstructure rearranges to accommodate hydrodynamic and interparticle forces and conditions[32]. In order to produce colloidal crystals on a scale that would be commercially viable, a method that produces high quality crystals with good long range order with favorable kinetics must be developed.

1.5 Assembly under shear flow

Since quiescent crystallization and sedimentation are slow, for practical applications, an increase in crystallization rate highly desirable[32]. Many types of flow systems have been explored for ordering colloidal suspensions. In particular, the effect of shear flow on colloidal suspensions has been studied extensively[17, 19, 39-41]. The effect of shear is governed by both shear rate and strain. Both simple and oscillatory shear have been shown to produce colloidal crystals under proper conditions including Peclet numbers above one [37].

The dimensionless Peclet number is a ratio of inertial to dispersion forces. For a uniform simple shear flow at fixed colloidal volume fraction, Ackerson and coworkers [42] discovered that a steady or oscillatory flow accelerates the production of colloidal crystal arrays provided that a dimensionless stress, the Peclet number (Pe), exceeds unity. Here $Pe = \frac{\tau_{21} a^3}{k_b T}$ where τ_{21} is the shear stress, a is the particle radius and $k_b T$ is the thermal energy.

Above the coexistence volume fraction, when Pe<1, the applied flow rate is not strong enough to overcome Brownian forces and crystallization occurs very slowly. At such flow rates particles are translated by flow by less than one particle diameter during the time they diffuse that same distance and hence the flow is unable to order them[32]. When an applied force dominates Brownian forces and the time scale of the flow that is less than the local diffusion time, microstructure is distorted. When Pe>1, however, the applied flow overcomes Brownian motion and significant microstructural reorganization occurs, for example into a randomly stacked configuration of sliding layers[40]. As the shear rate is increased further a variety of other microstructures are seen[19]. Application of oscillatory shear also results in a variety of microstructural transitions that depend on the shear rate and strain. In the high-Pe limit, strong convection progressively destroys 3D ordering.

The physical explanation of the dimensionless stress scaling for colloidal crystallization rests on an effective medium approximation [43]. In addition to modeling the onset of colloidal crystallization[40], the approximation successfully describes other features of concentrated colloidal suspensions, such as the onset of shear thinning [44] and shear thickening [45]. The stress based Peclet number for predicts crystallization in shear flow, however, formation of crystals under simple shear is limited by many factors including the domain size and long range ordering of the crystals produced. Spin coating is a non-uniform shear flow that shows promise for creation of colloidal crystals with good long range order. In order to understand the complicated spin coating flow, we apply the stress based Peclet number criteria to try to predict local order in spin coated samples.

1.6 Spin coating

Spin coating, a form of non-uniform shear, has also been used to fabricate colloidal crystals. Spin coating has long been used to deposit thin films of polymers on planar substrates and is used extensively in microlithography for manufacturing integrated circuits. It is a robust method that requires little equipment and produces uniform films, making it an excellent candidate for large scale fabrication of colloidal crystals. Jiang et al. [38] were the first to create multil ayer colloidal crystals by spin coating colloidal silica suspended in a viscous, non-volatile solvent. [46].

In addition to its important implications for materials processing, this discovery is significant colloid physics because it indicates that the action of complex physical processes such as evaporation are not a necessary condition for the production of colloidal crystal arrays on large scales. If spin coating could be used as a general tool for the production of colloidal crystal arrays, the potential for technological application of these structures is improved. However, this advance requires that we understand the operational parameters that must be used in spin coating to achieve ordered structures from a given particle suspension.

Early models of spin coating thin films were developed by Emslie et al. [47] and equations relating film thickness to spin speed were developed by Meyerhofer et al. [48]. In spin coating models, several assumptions are made including that (1) the substrate is mounted on a horizontal plane; (2) the initial liquid layer is radialy symmetric; (3) the effect of gravity is negligible due to the thinness of the film[47]. In spin coating, there is a balance of centrifugal and viscous forces. When the spin-coating substrate disc starts

spinning, much of the fluid is quickly flung off the edges by centrifugal force. The remaining film continues to thin due to radial outflow of the fluid. Spin coating flow of thin films has been approximated analytically using a quasi steady state version of the lubrication approximation with no-slip boundary conditions imposed on the solid-liquid interface.

Few studies of spin coating colloidal suspensions have been done. In colloidal suspensions, because the particles are charged, interparticle forces must be considered in addition to viscous and centrifugal forces. Here, we apply Ackerson et al.'s [49] findings for simple shear flow to the inhomogeneous, time-dependent flow of spin coating by hypothesizing that the steady-state local crystal quality in a complex flow is determined by a critical value of the *local* stress, $\frac{\tau_{rz}a^3}{k_bT}$. The local critical stress is a function of the axial and radial position, the time-varying height, h, of the spin coated film, the spin speed, the particle size and the thermal energy. If this hypothesis is valid, then knowledge of the fluid rheology is not necessary to determine local crystal quality in spin coating. This determination derives from the momentum balance for spin coating which yields a stress profile in equation (2) that is a function of only spin speed, film height and local position. Derivation of the spin coating Peclet number is given in chapter 2.

In order to assess the applicability of the stressed based Peclet number criteria to spin coating theory for predicting local order, it is necessary to directly visualize the sample microstructure to assess structure. We will achieve this using confocal microscopy.

1.7 Methods of studying colloidal crystals

Colloidal systems have been studied extensively using various scattering techniques including light, x-ray, and neutron scattering. Scattering is advantageous because measurements are fast and statistical uncertainties are small[23]. These methods provide information about global ensemble averaged structures existing at steady state. However, in complex systems, averaged information is not enough to understand the behavior of the system. Information about transient states and local structure cannot be accessed from scattering data. Additionally, structures and dynamic heterogeneities and defects can not be spatially mapped using light scattering[4].

Since the colloidal length scale is on the order of the wavelength of visible light[4] microscopy is an important method to study these systems. Optical and video microscopy have been used to study fluorescent colloidal systems. The disadvantage of these methods are that all parts of the optical path are excited leading to multiple scattering, and large amounts of noise making it impossible to resolve deep within a sample.

1.8 Direct visualization via confocal microscopy

Confocal laser scanning microscopy (CLSM) is a powerful to for assessing structure and dynamics in colloidal systems, allowing for investigation on the single particle level with high resolution without averaging[21]. Confocal microscopy is based on two important ideas: point by point illumination of the sample and rejection of out of plane light. In contrast to optical microscopy, confocal microscopy uses point illumination and a pinhole in an optically conjugate plane in front of the detector eliminates out-of-focus light. The aperture blocks light from other points in the sample

and allows imaging at precise locations deep within a sample. Two-dimensional images can be taken at small, evenly spaced intervals in the z direction and reconstructed into high quality three-dimensional projections. A schematic of a confocal microscope appears in Figure 1.

In confocal microscopy, a laser beam is directed by a dichroic mirror towards two mirrors – one scanning in the x direction and the other in the y direction. The light traveling through the dichroic mirror reflects light at the excitation wavelength and allows light in the emission band to pass through. The beam passes through a light source aperture where it is focused by the objective lens into a small focal volume and the fluorescent sample is excited. The scanning mirrors focus the light to a single point using the objective lens and mirrors move point to point to collect the data for the entire image in the selected focal plane. Scattered and reflected laser light and fluorescent light from the illuminated spot are re-collected by the objective lens. Emitted light travels back through the objective and the scanning mirrors, passes through the dichroic mirror, and focuses on the confocal pinhole. The light that passes through the pinhole is collected by a photomultiplier tube[23].

Photomultiplier tubes are extremely sensitive detectors that multiply the signal by several orders of magnitude. The detected light originating from an illuminated volume element within the specimen represents one pixel in the resulting image. As the laser scans over the plane of interest, a whole image is obtained pixel-by-pixel and line-by-line, and the brightness of a resulting image pixel corresponds to the relative intensity of detected light. The beam scans across the sample in the horizontal plane by using one or

more (servo controlled) oscillating mirrors. Slower scans provide a better signal-to-noise ratio, resulting in better contrast and higher resolution[4].

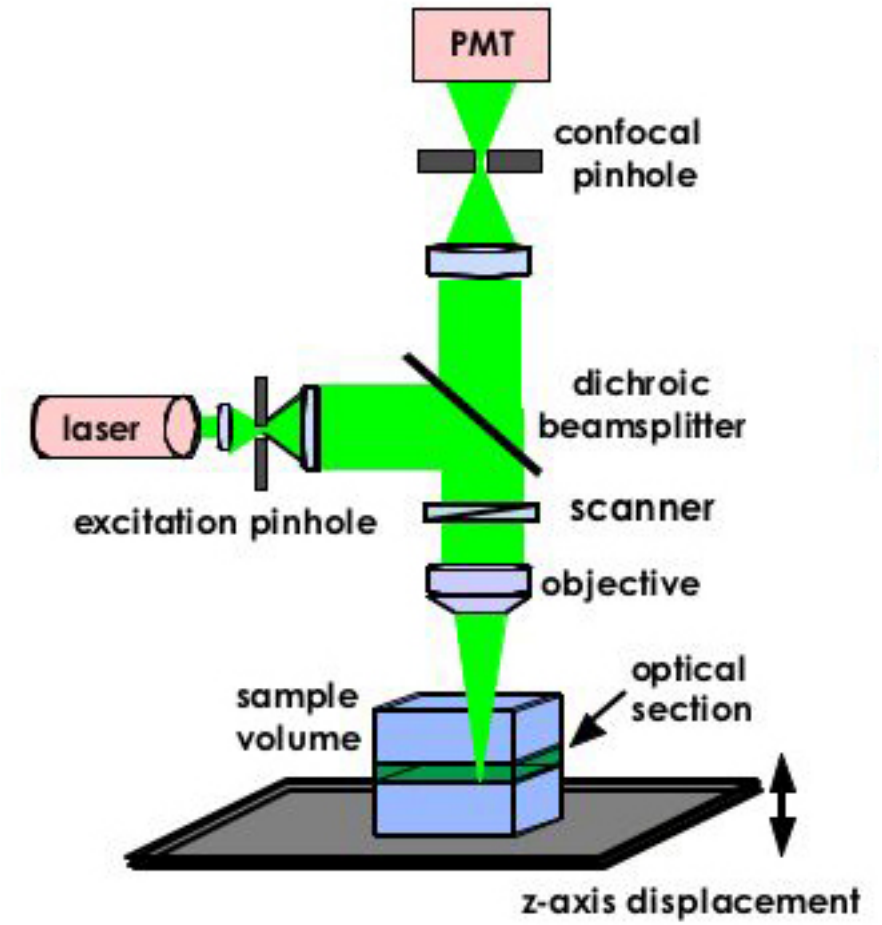

Figure 1. Schematic drawing of a laser scanning confocal microscope [47]

Information can be collected from different focal planes by raising or lowering the microscope stage. The computer can generate a three-dimensional picture of a specimen by assembling a stack of these two-dimensional images from successive focal planes[1]. In refractive index matched suspensions clear images can be taken for the entire working distance of the objective. For opaque specimens, images are superior to optical microscopy images because each 2D image incorporates only light from the focal plane whereas in optical microscopy the entire thickness the light can penetrate is shown.

1.9 Thesis outline

The overall goal of this dissertation is to characterize the microstructural response of dense colloidal suspensions to when subjected to a flow field and to gain an understanding of how microstructural transitions affect macroscopic properties. The two systems we explore are spin coating - a non-uniform shear flow - and simple uniform shear flow. Confocal microscopy is used to directly visualize both structure and dynamics in these systems. We use the Peclet number theory developed by Ackerson[39] to predict crystal formation under these flows. In chapter 2, particle synthesis and spin coating methods are described as well as image processing methods used to quantify local crystal quality from stacks of confocal images. Chapter 2 determines the critical stress and strain conditions necessary for crystal formation in spin coating. In chapter 3, minimum strain criteria for simple shear flows in the proper Peclet number range are established. Inhomogeneaties in the velocity profile are explored and correlated with movement of the crystalline boundary in the sample. Chapter 4 shows that in simple shear, application of a step strain deformation less than that required for full crystallization significantly

accelerates crystallization from the control. A templating hypothesis is proposed. Finally, chapter 5 establishes the range of volume fractions the Peclet number theory for spin coating can be used to predict local crystallization. Chapter 6 includes summary data and conclusions.

References:

1. **Dinsmore, A.D., et al., *Colloidosomes: Selectively permeable capsules composed of colloidal particles*, in *Science*. 2002. p. 1006-1009.**
2. **Davis, K.E., W.B. Russel, and W.J. Glantschnig, *Settling suspensions of colloidal silica - observations and x-ray measurements*, in *Journal of the Chemical Society-Faraday Transactions*. 1991. p. 411-424.**
3. **vanBlaaderen, A. and P. Wiltzius, *Growing large, well-oriented colloidal crystals*, in *Advanced Materials*. 1997. p. 833-&.**
4. **Mezzenga, R., et al., *Understanding foods as soft materials*, in *Nature Materials*. 2005. p. 729-740.**
5. **Baljon, A.R.C. and M.O. Robbins, *Energy dissipation during rupture of adhesive bonds*, in *Science*. 1996. p. 482-484.**
6. **Lewis, J.A., *Colloidal processing of ceramics*, in *Journal of the American Ceramic Society*. 2000. p. 2341-2359.**
7. **Lewis, R. and R.S. Dwyer-Joyce, *Interactions between toothbrush and toothpaste particles during simulated abrasive cleaning*, in *Proceedings of the Institution of Mechanical Engineers Part J-Journal of Engineering Tribology*. 2006. p. 755-765.**
8. **Hong, L., S.M. Anthony, and S. Granick, *Rotation in suspension of a rod-shaped colloid*, in *Langmuir*. 2006. p. 7128-7131.**
9. **Cush, R., D. Dorman, and P.S. Russo, *Rotational and translational diffusion of tobacco mosaic virus in extended and globular polymer solutions*, in *Macromolecules*. 2004. p. 9577-9584.**
10. **Whitesides, G.M. and M. Boncheva, *Beyond molecules: Self-assembly of mesoscopic and macroscopic components*, in *Proceedings of the National Academy of Sciences of the United States of America*. 2002. p. 4769-4774.**
11. **Horsch, M.A., Z. Zhang, and S.C. Glotzer, *Self-assembly of laterally-tethered nanorods*, in *Nano Letters*. 2006. p. 2406-2413.**
12. **Graham-Rowe, D., *Tunable structural colour*, in *Nature Photonics*. 2009. p. 551-553.**
13. **Kubo, S., et al., *Control of the optical properties of liquid crystal-infiltrated inverse opal structures using photo irradiation and/or an electric field*, in *Chemistry of Materials*. 2005. p. 2298-2309.**
14. **Blaak, R., et al., *Crystal nucleation of colloidal suspensions under shear*, in *Physical Review Letters*. 2004.**
15. **Pusey, P.N. and W. Vanmegen, *Phase-behavior of concentrated suspensions of nearly hard colloidal spheres,* in *Nature*. 1986. p. 340-342.**
16. **Chen, L.B., B.J. Ackerson, and C.F. Zukoski, *Rheologial consequences of microstructural transitions in colloidal crystals*, in *Journal of Rheology*. 1994. p. 193-216.**
17. **Russel, W.B. and W.R. Schowalter. 1989: Cambridge University Press.**
18. **Gasser, U., et al., *Real-space imaging of nucleation and growth in colloidal crystallization*, in *Science*. 2001. p. 258-262.**
19. **Larson, R.G., *The Structure and Rheology of Complex Fluids*. 1999, Oxford: Oxford University Press.**

20. **Prasad, V., D. Semwogerere, and E.R. Weeks, *Confocal microscopy of colloids*, in *Journal of Physics-Condensed Matter*. 2007. p. 25.**
21. **Hynninen, A.P., et al., *CuAu structure in the restricted primitive model and oppositely charged colloids*, in *Physical Review Letters*. 2006. p. 4.**
22. **Royall, C.P., M.E. Leunissen, and A. van Blaaderen, *A new colloidal model system to study long-range interactions quantitatively in real space*, in *Journal of Physics-Condensed Matter*. 2003. p. S3581-S3596.**
23. **Anderson, V.J. and H.N.W. Lekkerkerker, *Insights into phase transition kinetics from colloid science.* Nature, 2002. 416(6883): p. 811-815.**
24. **Auer, S. and D. Frenkel, *Prediction of absolute crystal-nucleation rate in hard-sphere colloids.* Nature, 2001. 409(6823): p. 1020-1023.**
25. **Velev, O.D. and S. Gupta, *Materials Fabricated by Micro- and Nanoparticle Assembly - The Challenging Path from Science to Engineering*, in *Advanced Materials*. 2009. p. 1897-1905.**
26. **Pronk, S. and D. Frenkel, *Large effect of polydispersity on defect concentrations in colloidal crystals*, in *Journal of Chemical Physics*. 2004. p. 6764-6768.**
27. **Jiang, P., *Large-scale fabrication of periodic nanostructured materials by using hexagonal non-close-packed colloidal crystals as templates*, in *Langmuir*. 2006. p. 3955-3958.**
28. **Wang, D.Y. and H. Mohwald, *Template-directed colloidal self-assembly - the route to 'top-down' nanochemical engineering*, in *Journal of Materials Chemistry*. 2004. p. 459-468.**
29. **Vermant, J. and M.J. Solomon, *Flow-induced structure in colloidal suspensions*, in *Journal of Physics-Condensed Matter*. 2005. p. R187-R216.**
30. **Jiang, P., et al., *Single-crystal colloidal multilayers of controlled thickness*, in *Chemistry of Materials*. 1999. p. 2132-2140.**
31. **Zahn, K., J.M. MendezAlcaraz, and G. Maret, *Hydrodynamic interactions may enhance the self-diffusion of colloidal particles*, in *Physical Review Letters*. 1997. p. 175-178.**
32. **Wen, W.J., L.Y. Zhang, and P. Sheng, *Planar magnetic colloidal crystals*, in *Physical Review Letters*. 2000. p. 5464-5467.**
33. **Hansen, J.P. and H. Lowen, *Effective interactions between electric double layers*, in *Annual Review of Physical Chemistry*. 2000. p. 209-242.**
34. **Solomon, T. and M.J. Solomon, *Stacking fault structure in shear-induced colloidal crystallization*, in *Journal of Chemical Physics*. 2006. p. 10.**
35. **Jiang, P. and M.J. McFarland, *Large-scale fabrication of wafer-size colloidal crystals, macroporous polymers and nanocomposites by spin-coating*, in *Journal of the American Chemical Society*. 2004. p. 13778-13786.**
36. **Ackerson, B.J., *Shear induced order and shear processing of model hard-sphere suspensions*, in *Journal of Rheology*. 1990. p. 553-590.**
37. **Ackerson, B.J., *Shear induced order in equilibrium colloidal liquids*, in *Physica A*. 1991. p. 15-30.**
38. **Ackerson, B.J. and T.A. Morris, *Shear induced order of concentrated dispersions,* in *Better Ceramics through Chemistry Iv*. 1990. p. 159-166.**

39. **Ackerson, B.J., *Shear Induced Order and Shear Processing of Model Hard-Sphere Suspensions.* Journal of Rheology, 1990. 34(4): p. 553-590.**
40. **W.B. Russel, D.A.S., W.R. Schowalter, *Colloidal Dispersions*. 1989, New York City: Press Syndicate of the University of Cambridge. 525.**
41. **Ackerson, B.J. and P.N. Pusey, *Shear-Induced Order in Suspensions of Hard-Spheres.* Physical Review Letters, 1988. 61(8): p. 1033-1036.**
42. **Bender, J. and N.J. Wagner, *Reversible shear thickening in monodisperse and bidisperse colloidal dispersions.* Journal of Rheology, 1996. 40(5): p. 899-916.**
43. **Jiang, P. and M.J. McFarland, *Large-scale fabrication of wafer-size colloidal crystals, macroporous polymers and nanocomposites by spin-coating.* Journal of the American Chemical Society, 2004. 126(42): p. 13778-13786.**
44. **Emslie, A.G., F.T. Bonner, and L.G. Peck, *Flow of a viscous liquid on a rotating disk*, in *Journal of Applied Physics*. 1958. p. 858-862.**
45. **Meyerhofer, D., *Characterisics of resist films produced by spinning*, in *Journal of Applied Physics*. 1978. p. 3993-3997.**
46. **Ackerson, B.J. and P.N. Pusey, *Shear-induced order in suspensions of hard-spheres*, in *Physical Review Letters*. 1988. p. 1033-1036.**
47. **Solomon, M.J. and M. Kogan, in *Encyclopedia of Condensed Matter Physics*.**

CHAPTER 2

Local stress control of spatiotemporal ordering of colloidal crystals in spin coating

2.1 Chapter summary

We show that spin coating, an unsteady, non-uniform, shear flow, produces spatiotemporal variation in the crystal order of concentrated colloidal dispersions that is a universal function of the local reduced critical stress and the macroscopic strain. The dependence of the crystal quality of model poly(methyl methacrylate) colloids on radial and axial position, spin speed and particle size is quantified by confocal microscopy. The coupling of flow-induced crystallization with the centrifugally-driven spin coating flow determines local crystal quality without a priori knowledge of the suspension rheology.

2.2 Introduction

Because of its speed and planarity, spin coating has excellent potential for colloidal crystal assembly. Spin coating has long been used to deposit thin films of polymers on planar substrates and is used extensively in microlithography for manufacturing integrated circuits. It is a robust method that requires little equipment

and produces uniform films, making it an excellent candidate for large scale fabrication of colloidal crystals [46]. In spin coating a thin liquid film is deposited on a substrate and rotated at rates between 200rpm and 1200rpm.. Excess fluid is flung off quickly and the liquid film rapidly levels. Generally non-Newtonian shear thinning fluids take more time to level than Newtonian samples but also result in films of uniform thickness. In spin coating a volatile solvent is often used and film properties are affected by the evaporation rate. In the experiments presented in this paper a non-volatile solvent is used in order to produce planar films and to control other film properties. The use on a non-volatile solvent also simplifies the spin coating model significantly. This could provide a path to applications such as inverted crystals.

Jiang et al.[46] were the first to create multilayer colloidal crystals by spin coating colloidal silica. If spin coating can be used as a general tool for the production of colloidal crystal arrays, then the potential for technological application of these structures is improved. However, this advance requires that we understand the operational parameters that must be used in spin coating to achieve ordered structures from a given particle suspension. Here we aim to develop this general framework**.**

To understand the dynamics of spin coating and to assess the effect of critical parameters we must be able to view the internal structure at various points during the spin coating process. Since it is impossible to view instantaneous structures on the spin coating apparatus we have developed a method to immobilize the structures at desired times in order to image them using confocal microscopy. Such stacks of confocal images can be analyzed using image processing techniques. In what follows a method of forming and immobilizing colloidal crystals will be presented. Both axial and radial

variation of crystal quality will be explored and a theory relating crystal quality to dimensionless Peclet number – the ratio of convective to dispersive forces - will be presented. Dependence of time and macroscopic strain will also be presented.

2.2.1 Spin coating fundamentals

Spin coating has been used for many years in various industries including the semiconductor industry to efficiently fabricate thin films of uniform thickness. In spin coating, a thin wafer is centered and aligned on a chuck and fixed to the surface by pulling a vacuum. The desired coating solution is dispensed on the wafer and the substrate is rotated at high speeds for a predetermined amount of time in order to produce a film with the desired thickness. Spin coating is especially useful in spreading viscous, high surface tension solutions that are otherwise difficult to use as coatings [46, 47].

2.2.2 Stress control of colloidal crystal formation

In the case of simple shear flow at fixed colloidal volume fraction, Ackerson and coworkers [49] discovered that the action of a steady or oscillatory flow accelerates the production of colloidal crystal arrays provided that a dimensionless critical stress, the Peclet number (Pe), is greater than unity. The Peclet number is defined as

$$Pe = \frac{\tau_{yx} a^3}{k_b T} \qquad (1.)$$

where τ_{yx} is the shear stress in the flow, a is the colloid radius and k_bT is the thermal energy.

Pe characterizes the balance of convection, which tends to distort the particle microstructure, and Brownian motion, which acts to restore the particles to their equilibrium configurations. Above the coexistence volume fraction, strong shear flow (Pe > 1) leads to the production of close-packed layers with relative abundances of hexagonal close-packed and face-centered cubic stacking that depend sensitively on Pe and, in oscillatory flow, strain amplitude [39, 49]. For high Peclet numbers, strong convection progressively destroys 3D ordering by shear melting [51].

2.2.3 Application of stress criteria to spin coating

To develop a universal description of the performance of spin coating, we exploit a remarkable coincidence between the driving force for local crystallization, which is stress-controlled, and the fluid physics of spin coating, which is also stress-controlled. This congruence allows crystal quality to be predicted independent of dispersion rheology. We hypothesize that the fundamental physics that contributes to the universal behavior is generally applicable to stress-controlled complex flows. In particular, velocity and velocity gradient fields will depend sensitively on the fluid rheology. These fields in turn will determine the time-dependence of the height profile of the thin film.

Although the well-studied Newtonian fluid dynamics of spin coating [52] are not applicable to the production of colloidal crystal arrays because the rheology of the colloidal dispersions is non-Newtonian, the underlying momentum balances used in such analyses are germane. For the case of no evaporation, radial symmetry and

viscous flow, application of the lubrication approximation yields the following momentum balance in cylindrical polar coordinates:

$$\frac{\partial \tau_{rz}}{\partial z} = \rho \omega^2 r \tag{2.}$$

Integration of the momentum balance yields the shear stress profile:

$$\tau_{rz} = \rho \omega^2 r(z - h) \tag{3.}$$

where ρ is the fluid density and ω is the rotation rate in s^{-1}. We see that the τ_{rz} depends on both radial, r, and axial, z, position. The total film thickness, h, depends on the local volumetric flow, which is directed radially [52]. Note that the flow is stress-controlled in the sense that the velocity field varies in time to accommodate a radial shear stress generated by the centrifugal force of the rotating spin coater.

The general form of the Peclet number is shown in equation 1. Substituting the calculated stress into the Pe equation we obtain an expression for the spin coating local Peclet number. The Peclet number is a function of ω, a, and position in the sample(r,z). Setting equation 4 equal to one gives us the critical condition for the spin coating Peclet number.

$$Pe = \frac{6\pi\rho\omega^2 r(h - z)a^3}{k_B T} \tag{4.}$$

2.3 Materials and methods

Particles used for all experiments were synthesized using methods from Antl et al.[53] and Pathmamanoharan et al.[54]. Synthesis protocol and experimental design are described in the sections below. Poly(methyl methacrylate) (PMMA) particles are also compatible with many organic solvents both volatile and non-volatile. PMMA particles

were selected because they can be synthesized in-house in a variety of sizes, with dye incorporated in the particles allowing for confocal visualization . Particle synthesis has two main stages: stabilizer synthesis and particle synthesis. Stabilizer synthesis is done in three parts: polymerization and lengthening of poly(12-hydroxystearic acid) chains, glycidyl methacrylate copolymerization with the poly(12-hydroxystearic acid) chains, and polymerization of methyl methacrylate and methacrylic acid copolymerize with each other and with the product from the previous step forming a poly(12-hydroxystearic acid)-g-poly(methyl methacrylate-co-glycidyl methacrylate) copolymer[53]. The particle synthesis is done in two steps: a dispersion polymerization and a locking step. These steps are discussed in detail in the sections below.

2.3.1 Purification of raw materials

Inhibitor was removed from methyl methacrylate using a pre-packed hydroquinone monomethyl ether column (Sigma). A separatory funnel was filled with methyl methacrylate and mounted above the column. Methyl methacrylate was added drop wise to the column and the filtered product was and stored in the refrigerator. The filtered methyl methacrylate has a shelf life > 2 years.

2,2'-azo-bis-isobutyronitle (ADIB) as received was mixed with acetone in an Erlenmeyer flask in the ratio of 1.5g ADIB/10mL acetone and dissolved by gently agitating the flask. The solution was pipetted into Teflon centrifuge tubes and placed in the freezer for 24 hours. After 24 hours the solution was removed from the freezer and centrifuged for 5 minutes at 7500rpm. After centrifuging, the solvent and impurities

were pipetted out and discarded. The ADIB crystals were dried in an amber glass jar for at least 24 hours and the recrystallized ADIB was stored under refrigeration.

2.3.2 Poly(12-hydroxystearic acid) stabilizer synthesis

Synthesis of poly(12-hydroxystearic acid) stabilized poly(methyl methacrylate) (PMMA) particles involved two distinct sets of reactions: the preparation of the stabilizer and the synthesis of the actual spheres. Stabilizer was made in large batches of approximately 2000g. Each batch of particles synthesized required approximately 2g of stabilizer and yielded about 37g of particles. The stabilizer synthesis, based on the work of Dohnt et al. [54], consisted of three steps. First 12-hydroxystearic acid (Fluka, 56640) was polymerized to form chains of poly(12-hydroxystearic acid) (PHSA). The polymer (PHSA) was melted under nitrogen in a 3-neck flask and methanesulfonic acid (Sigma, 47135-6) was added to catalyze the polymerization. The reaction proceeded to completion in 24 hours. The extent of reaction was verified by titrating a small sample of the PHSA product in an ethyl acetate (Sigma, 27098-9) and butyl acetate (Sigma, 40284-2) mixture with potassium hydroxide (Sigma, 31433-3) (KOH) and phenolphthalein (Fluka, 34696) as an indicator. If not enough 12-HSA was reacted the step one product was discarded and step one was repeated. The PMMA synthesis setup is shown in Figure 2.

Step II was performed immediately upon completion of step I. In this step, the PHSA chains were copolymerized with glycidyl methacrylate (Sigma, 15123-8). Toluene (Sigma, 27037-7), glycidyl methacyrlate, 1-dimethylaminododecane (Fluka, 39149), and t-butyl cathecol (Sigma, 12424-4) were added to the product from step I

and allowed to reflux for seven hours. A titration with an acid value of 0.32mg KOH/g stabilizer indicated the reaction had gone to completion.

In the final step PHSA chains were copolymerized with methyl methacrylate. The cooled product from step II was mixed with methyl methacrylate, glycidyl methacrylate, and 2-2' azo-di-bis-isobutyronitrile (Sigma, 44109-0) (ADIB). This solution was added dropwise to a refluxing mixture of ethyl and butyl acetate over 3.5 hours and allowed to reflux for six additional hours. The product was a viscous, honey colored liquid. After cooling, stabilizer was stored in the fridge.

2.3.3 Synthesis of 12-PHSA poly(methyl methacrylate) particles

Monodisperse fluorescent poly(12-hydroxystearic acid) stabilized poly (methyl methacrylate) particles (PMMA) were synthesized via dispersion polymerization in a two-step process based on methods by Antl et al.[53], Campbell and Bartlett[55], and Pathmamanoharan et. al [54]. Step one was a dispersion polymerization in a hexane and dodecane mixture where the two monomers- methyl methacrylate (Sigma, 30631-2) and methacrylic acid (Sigma, 39537-4) - were catalyzed with ADIB and polymerized in the presence of poly(12-hydroxystearic acid) stabilizer and Nile Red dye (Sigma, N3013-100mg). In order to make uniform particles the solvents and stabilizer were brought to reaction temperature (80°C) and held for 30 minutes before the remaining reactant mixture was added. The reactants were stirred vigorously with a large spatula for 5-10 seconds and the reaction was allowed to proceed for two hours. After approximately 10 minutes the solution became turbid indicating polymerization had occurred.

Once polymerization was complete the reaction temperature was increased and catalyst was added causing the methacrylic acid molecules in the PMMA chains to react with the glycidyl methacrylate in the stabilizer backbone. Hexane was evaporated off and replaced by dodecane using a Dean-Stark apparatus. This step is referred to as a "locking step" because the stabilizer backbone bonds covalently to the particles to form a steric layer approximately 14 nm thick. Figure 3a is a schematic diagram of a stabilized particle from reference [56]. A sample particle synthesis recipe is shown in A. Particles were cleaned by solvent replacement eight times in hexane, dried in a fume hood, and sized using scanning electron microscopy. Polydispersity, a measure of the heterogeneity of the sample was calculated for each batch of particles by dividing the standard deviation of the particle diameter by the mean particle diameter. To determine polydispersity, particles were dried and redispersed in hexane. A drop of the suspension was dispensed on an SEM stub and dried. A thin layer of platinum was sputter coated on the sample and it was imaged using a Philips XL30FEG scanning electron microscope at magnifications >8000. A sample SEM image of a batch of particles is shown in Figure 3b To determine the size distribution, radii of 100 or more particles were measured using ImageJ software (National Institutes of Health). The average value was determined to be the diameter of a dry particle. Because crystal formation rates depend on polydispersity only batches of particles with <5.0% polydispersity were used in crystallization experiments.

2.3.4 Properties of poly(methyl methacrylate) particles

The resulting PMMA particles have a density of 1.185 g/cm^3 [55] and a refractive index of 1.485 [57]. Refractive index is a measure of how the speed of a wave (light) is reduced inside a medium. These particles are ideal for our work because their refractive index is very close to that of many organic solvents indicating compatibility. The PMMA particles contained Nile Red dye (excitation 485, emission 525), which allowed for imaging by confocal microscopy using either a 488 nm or 543 nm laser. The particles are negatively charged and interact repulsively.

Dioctyl phthalate (DOP) was chosen for a solvent because it is viscous and non-volatile. Since crystallization is strongly dependent on volume fraction, the non-volatile nature removes the complication of evaporation from the system. Also, DOP has a refractive index very close to the PMMA particles (RI = 1.485).

2.3.5 Photopolymer and photoinitiator selection

After selecting the solvent system we needed to select a compatible photopolymer and photoinitiator. In spin coating, samples are subjected to large centrifugal forces that push liquid to the outer edge of the substrate, resulting in the formation of a meniscus. When the force was removed, the meniscus was no longer pinned on the outside edge of the sample and began to creep inward, distorting the sample microstructure. In order to study structure formed by spin coating it was necessary to devise a method to immobilize samples at the desired moment in time. This was achieved using free radical photopolymerization.

Photopolymer and photoinitiator selection were based on several criteria. First, each component needed to be compatible with the base colloidal system. Second,

components had to be non-volatile so they would not evaporate during spin coating, The photopolymer system also needed to cure nearly instantaneously when exposed to ultraviolet light and curing could not shrink or distort the microstructure. In order to realize a nearly instantaneous cure we investigated acryl terminated organic monomers. Solutions of several different non-volatile acryl-terminated monomers were mixed in a 1:5 ratio with DOP to determine which monomers were compatible with the system. Among the tested possibilities, propoxylated (6) trimethylolpropane triacrylate (CD 501, Sartomer) was selected because it was miscible with DOP, had good refractive index and density match ($\rho = 1.048$, RI = 1.4567) with the system and was non-volatile. To select a photoinitiator, solutions of several initiators were mixed with DOP in a ratio of 1:10 to determine system compatibility. The absorption spectrum of each compatible initiator was examined in order to find one with a strong absorption in the desired range of 350-365nm. Phosphine oxide (Irgacure 2100, Ciba Specialty) was selected because of strong absorption both at 365nm and 254nm (appendix B) giving flexibility for curing in addition to being non-volatile and having a compatible refractive index and with the base system ($\rho = 1.10$, RI ~1.4). The time for curing in the system described is < 1 second. Structures of the substances involved in the free radical polymerization are shown in Figure 4.

After selecting the monomer and initiator tests were performed to determine the minimum amount of polymer and initiator necessary to immobilize samples without microstructural distortion. Suspensions with varying amounts of photopolymer and initiator were spin coated for three minutes at 600 rpm. The samples were mounted on the confocal microscope and imaged both perpendicular to the substrate and parallel to

the substrate 30μm from the substrate surface. Samples were then exposed to UV light and the same two locations were imaged. The xy images before and after photopolymerization are shown in Figure 5a and Figure 5c respectively. These images were compared by visual inspection and fast Fourier transform (FFT) and it was determined that the microstructure was not deformed/distorted by photopolymerization. This is determined by examining the figure below and noting the before and after images are almost identical indicating that photopolymerization has not altered structure. 7% photopolymer and 1% initiator were selected for use.

Spin coated samples were exposed to a 15W 365nm light source. (UVP Blak-Ray* UV Benchtop Lamps, 95 0042 11) for 30 seconds to ensure complete photopolymerization. The whole area of the 25mm diameter circular sample was cured upon exposure with films up to 150μm thickness tested within one second of exposure.

2.3.6 Sample preparation

Suspensions for all experiments were 35% by volume PMMA (d_p = 1.05μm), 7.5% photopolymer (CD501, Sartomer), 1% photoinitiator (Irgacure 2100, Ciba Specialty) in cis-trans dioctyl phthalate (DOP) (Sigma, 525154) with 13μM tetrabutylammoniumchloride (TBAC) (Sigma, 1112-67-0) to screen charges. Before use DOP was filtered with a 0.2μm hydrophobic polypropylene membrane filter using a vacuum filtration apparatus made for viscous liquids (PALL, model VacuCap 90). Filtered DOP was combined with TBAC to make a 1mM stock solution. Stock solutions of 0.25mM, 0.1mM and 0.01mM TBAC in DOP were made by combining aliquots of the 1mM solution with pure DOP to achieve the desired concentrations. The particles,

photopolymer and initiator solutions, and DOP were weighed, vortex mixed, and then rolled on a Wheaton Benchtop Roller for at least 24 hours before use.

The well-mixed suspensions prepared above were dispensed onto 25mm diameter (#2 thickness) round glass cover slips (as supplied from Fisher Scientific) using a 50μL Hamilton gas-tight microsyringe. The substrate was tilted and rotated to spread the suspension, creating a film of uniform thickness. The sample was centered on the chuck and a vacuum was applied to the bottom of the substrate. The substrate was spun at a fixed rate for the desired amount of time.

2.3.7 Confocal laser scattering microscopy (CLSM) imaging

We used a Leica TCS DMIRE 2 inverted microscope with an xyz stage controlled by galvometric actuation to image spin coated samples. The glass coverslip was mounted onto a metal plate with a hole in the center using vacuum grease and positioned on the stage using the clips on the sample holder. A 100x objective (oil immersion, NA 1.4) was used for imaging. The Nile Red stained PMMA particles fluoresced under argon-ion laser at a wavelength of 488nm with an emission band set between 540-560nm. Sample volumes were imaged by taking stacks of two-dimensional images of size 25x25μm at equally separated z-heights (z = 0.081μm) by piezoelectric actuation of the galvanometric stage. Because interparticle spaces were filled with refractive index matched solvent all of the planes of the sample could be visualized up to the working distance of the objective, which extended about 150 microns above the substrate. Images were collected through the entire film thickness at

800Hz- an approximate acquisition rate of 823ms/image. A schematic diagram by Solomon et al. [58] and a typical xy image are shown in Figure 6.

2.3.8 Image processing and data analysis

Stacks of 2D confocal images were processed using an algorithm based on the work of Crocker and Grier[3]. Stacks of xy images (~400) a size of 512x512 pixels were converted from 8-bit tiff images to bin files. Subroutines were used to determine the location of particle centroids in the confocal images. A Gaussian filter was applied to each of the raw images to remove high frequency noise. Particle centroids were located in the filtered images by finding local brightness maxima in small three dimensional domains approximately the size of a particle diameter. A schematic of this process is shown in Figure 7.

Accuracy of the algorithm was confirmed both by visual inspection of overlay images (Figure 8) and by comparing the volume fraction of particles calculated from the weights of particles in the original solution and the volume fraction of particles found by the algorithm. For samples where $\Phi = 0.35$ from the volume fraction calculated using particles weights, the second method gave $\Phi = 0.35 \pm 0.01$.

2.3.9 Order analysis algorithm

After locating particle centroids, local structure was analyzed by defining a reaction coordinate sensitive to the overall degree of crystallinity but insensitive to both the type of structure (i.e. FCC vs. HCP) and orientation in space. A quantity based on

spherical harmonics, defines the local bond order parameter, q_6 [3] shown in equation 5 :

$$\tilde{q}_{lm}(i) = \sum_{j=1}^{N_b(i)} Y_{lm}(\hat{r}_{ij}) \frac{1}{N_b(i)} \qquad (5)$$

Where i is the reference particle, j is a neighboring particle, the coordination number N_b is the number of neighboring particles, and $Y_{lm}(\theta_{lm},\phi_{lm})$ are spherical harmonics evaluated at the polar and azimuthal angle. The m^{th} component of q_6 is represented by equation 6:

$$\tilde{q}_{6m}(i) = \frac{\bar{q}_{6m}(i)}{[\sum_{m=-6}^{6} |\bar{q}_{6m}(i)|^2]^{0.5}} \qquad (6)$$

To determine the local structure of a sample, each particle in the sample is determined to be crystalline or amorphous by calculating the bond coherence between the reference particle and each of its neighbors. Bond coherence is measured by the dot product of $q_6(i)$ and $q_6(j)$ shown below.

$$q_6(i) \bullet q_6(j) = \sum_{m=-6}^{6} \tilde{q}_{6m}(i) \tilde{q}_{6m}(j)^* \qquad (7$$

A bond is considered crystalline if q6(i)•q6(j) > 0.5. Particles with eight or more crystalline bonds are considered crystalline[3]. This measurement system has been used extensively in both experiments and simulations [6, 59].

2.3.9.1 Definition of neighbor particles

A neighbor particle was defined as a particle within a given distance, r_max, from the centroid of the reference particle. A first estimate of r_max was taken as the

first minimum of the pair correlation function g(r). A sample g(r) plot is shown in Figure 9.

For this system the first minimum occurs at 1.62μm. To determine the best value of r_max, the q_6 algorithm was run on a dense sample (ϕ=0.35) using several different values of r_max both above and below initial guess. The contact number distribution was plotted for each value of r_max. This is shown in Figure 10.

In a dense suspension, regardless of the degree of ordering, most particles should have twelve nearest neighbors [3]. We chose to use the first minimum of g(r) as r_max because the maximum of its coordination number distribution was at 12 and there were only a small amount of particles that had a coordination number greater than 12.

2.3.9.2 Definition of crystallinity

In literature, a particle is considered crystalline if it has eight or more crystalline bonds with its neighbors[3]. In order to confirm this definition we ran the q6 algorithm several times on the same sample, varying the definition of minimum number of crystalline bonds from 6-9. The number of crystalline particles as a function of z position in the sample were plotted in Figure 11.

Upon inspection, the shapes of the curves in Figure 11 were very similar, indicating that the number of crystalline bonds in a sample was not sensitive to variations in the definition of crystallinity. Th erefore, consistent with literature, we define a crystalline particle as a particle having eight or more crystalline bonds with its neighbors.

2.3.9.3 Assessing the accuracy of the q_6 algorithm

In order to use the q6 algorithm to determine crystal quality it was necessary to verify that the code could discriminate between amorphous and crystalline structures. To achieve this we analyzed a sample known to be amorphous and a crystalline structure and compared its coordination number distributions and number of crystalline bond distributions. Three dimensional renderings of these samples are shown in Figure 12. Figure 12b and Figure 12d are images taken perpendicular to the substrate of these samples.

2.3.9.4 Coordination number distribution

In dense solid and liquid systems, the coordination number is expected to be 12 on average. Using the first minimum of g(r) as r_max, the coordination number distribution for each sample were determined. Figure 13 shows the distributions for each sample.

2.3.9.5 Number of crystalline bonds distribution

The plot of the distribution of the number of crystalline bonds for both samples in figure 10 are shown in Figure 14. As expected, the distributions are very different for the two samples. For the crystalline sample most particles have 12 crystalline bonds with their neighbors however, even though the particles in the amorphous sample have the same number of neighbors, most particles have two or less crystalline bonds with its neighbors.

2.3.9.6 Differentiation of crystal vs. amorphous

Distributions of the coordination number and the number of crystalline bonds for a crystalline and an amorphous test case were generated and compared. Since the samples were made from the same suspension, it was expected that the coordination number distribution for both samples should be very similar. This was confirmed by Figure 13. The number of crystalline bonds distribution was expected to be very different for each sample. As expected in the crystalline sample the peak occurred at 12. In the amorphous sample, very few particles were considered crystalline and the peak of the distribution was 1-2. From these results, it was clear that the code could differentiate between crystalline and amorphous structures.

2.3.9.7 Determination of phase boundaries

In hard sphere systems phase boundaries are well established as a function of volume fraction. Below a volume fraction of Φ_L the sample structure will be liquid. For volume fractions between Φ_L and Φ_S the system coexists as solid and liquid where the fraction of each phase is determined using the lever rule. When the particle volume fraction exceeds Φ_S the structure will be crystalline until the particles jam at the glass transition. For hard sphere systems $\Phi_L = 0.494$ and $\Phi_S = 0.545$ [42]. However, the particles used for these experiments were charged so it was necessary to experimentally determine the phase boundaries for the system. The limits we needed to establish were the crystalline regime Φ_S, the coexistence range, and the volume fraction below which the structure remains liquid Φ_L. To determine these limits solutions with volume

fractions ranging from $0.15 < \Phi < 0.45$ were prepared. Approximately 200μL of each solution was dispensed in 3mm diameter glass capillaries mounted on a glass coverslip. At times of 0, 2, 12, and 24 hours, each sample was imaged perpendicular to the substrate and the phase was determined by visual inspection. Samples were also imaged after one week, two weeks, and one month in order to confirm steady state equilibrium had been reached. The coexistence region for this batch of particles was bounded by. $\Phi_L = 0.17$ and $\Phi_S = 0.225$. To compare this to the hard sphere system we found the number of hard sphere particles used to fill 0.494mL of a 1mL volume. Then we found out the number of particles needed to achieve a hard sphere volume fraction of 0.225, The Debye length was substituting (0.34μm+r) into the volume of a sphere equation in place of r. Solving this equation gave a Debye length of 4.07μm which seems too large when visually examining confocal images.

The criteria for selection of the volume fraction for spin coating experiments were that (1) crystals must form under spin coating and (2) there must be a significant difference in crystal formation time for the quiescent case and spin coating. The latter is to allow differences between flow-induced and equilibrium crystallization to be distinguished. We chose a particle volume fraction of $\Phi = 0.35$ for all experiments because it was in the crystalline regime and preliminary experiments indicated that samples would crystallize at this concentration in spin coating. To determine the rate of quiescent crystallization for $\Phi = 0.35$ solution, a sample was prepared as described above and allowed to quiescently crystallize. Stacks of xy images were taken every 2 hours for the 12 hours, and every 12 hours until 48 hours.

2.4 Experimental results

The overall goal of this study was to understand local crystal formation in spin coating - a complex, non-uniform shear flow – using a simple, stress-based model for uniform shear flow. In this section we use the Peclet number criteria established for simple shear flow[42] to determine critical parameters for crystallization in spin coating. Because of the stress and strain dependence of structure formation in simple shear, we examined factors determining the spin coating Peclet number (equation 4). In this section we report the steady state variability of local crystal quality as a function of both axial position and radial position in the sample. Additionally, we address the effect of spin speed and particle size as well as strain and processing time on local crystal quality.

2.4.1 Axial variation of crystal quality

The spin coating Peclet number (equation 4) derived in section 2.1.3 is a ratio of convective and dispersive forces. Equation 4 indicates that local crystal quality should depend on both radial and axial position in the sample. To determine axial variation, a sample initially 80μm thick was spin coated for 3 minutes at an angular velocity of ω = 600rpm and immobilized using photopolymerization. The sample was imaged at a radial position of 31.25 μm from the axis of rotation. Crystal quality was assessed using the algorithms outlined in section 2.2.7.

Figure 15a is a plot of average crystal quality as a function of z position in the sample. In all samples z = 0 is the substrate and z = h is the free surface and radial position, spin speed and duration are held constant. Error bars represent standard error

of the mean for six independent samples and are typical of all subsequent figures. From this plot, it is evident that at steady state crystal quality varies as a function of axial position in the sample. At a radial position of 0.0025mm, local crystallinity at the bottom 15% of sample is high (approximately 90%), however, at increasing z position the crystalline fraction rapidly decreases to zero. The inset of Figure 15a is an xz confocal image of a typical sample at these conditions imaged at r/R =0.0025. The three dashed lines in the inset correspond to the three axial positions indicated in by the arrows on the plot. Images 1,2, and 3 are xy images corresponding to the planes indicated by the dashed lines in Figure 15b. By visual inspection the xy images are in agreement with the percent crystallinity shown on the plot and xz image.

Positions of all particles in the image volume in Figure 15 are rendered in part c. Crystalline particles are purple and amorphous particles are green. The spatial location of the crystallization boundary in the rendering also agrees with Figure 15a and the inset.

The sharp axial transition that is observed is not purely a consequence of boundary-induced nucleation because its location varies strongly with radial position, spin speed, and duration. We know that the structure variation is due to spin coating because heterogeneous quiescent nucleation times for this sample were found to be 2 orders of magnitude greater than the 3 min duration of this experiment.

2.4.2 Radial variation of crystal quality

At a fixed spin speed, local steady state structure can be predicted for any radial position in a sample using the dimensionless Peclet number. Figure 16a is a plot of

Peclet number versus position in the sample. For spin coated samples (initial thickness 80μm) where ω = 600rpm and duration is 3 minutes, the thickness of the resulting film is ~40μm. The gradient on the plot represents the Peclet number at each position with blue being the lowest values and red being the highest.

Figure 16 quantifies both the radial and axial dependence of local crystal quality at seven different radial positions in the sample. Consistent with the monotonically increasing dependence of Pe on r in equation 4, the average crystallinity increases from 15% at the axis of rotation to 90% at the outer edge of the substrate. In some samples some crystallization also occurs at the free surface where z = h, however this ordering does not propagate more than a few microns into the sample except at very low spin speeds. Therefore, Figure 16 supports the r and z dependence in equation 4. Vertical dotted lines indicate radial positions where local crystal quality was assessed. Values at the top of each dotted line are the average crystalline fraction for samples at that radial position. Each value is the average of 5 independent samples.

The Peclet number prediction suggests that high levels of crystallinity should occur preferentially at the substrate since the stress is the greatest there. Additionally, as r increases, the height of the crystalline boundary should increase. The axis of rotation is located at Pe=0 and the free surface of the film is at z = h. Using Ackerson's criteria for crystallization[42], the critical Peclet number of unity is shown using the black curve. To the left of the curve, dispersive forces dominate and no crystals are expected to form on the order of time for spin coating. To the right, convective forces were dominant and the steady state structure was expected to be crystalline. Figure 16b,d,f are confocal images taken normal to the substrate for samples at three different radial

positions of 0.0, 0.31, and 0.625mm from the axis of rotation. Arrows point from the corresponding radial position on the plot to the xy images. Visual inspection of the images indicate that they are in agreement with the crystalline percentages shown. Figure 16c,e,g are plots of crystal quality as a function of axial position in the sample from the images directly above.

2.4.3 Peclet number dependence of crystal quality

As established in section 2.1.3 the spin coating Peclet number depends on the spin speed, radial and axial position in the sample, and particle size. We tested equation 4 further by measuring steady state crystallinity at different spin speeds (ω = 200, 350, 600, 1050rpm) and different particle sizes (d_p = 0.79μm, 1.05μm, 1.43μm). A list of experimental conditions are shown in table 1.

For each radial and axial position studied the crystalline fraction, X, is plotted versus the local Peclet number. All the data were combined in Figure 17. This figure strongly supports the hypothesis that in spin coating local crystallinity is controlled by Peclet number. In all cases, for values of Pe < 1, the crystalline fraction is negligible. For Pe > 1, X increases sharply and plateaus at X~0.85 which is fully crystalline within error margins. The high crystalline fraction persists to the highest Peclet number tested (~1000). Thus, Figure 17 provides both positive and contrapostive indications of the Pe = 1 disorder to order transition and we consequently conclude that equation 4 successfully predicts the dependence of local crystal quality on the parameters ω, r, z and a.

2.4.4 Strain and time dependence of crystal quality

The technique of structure immobilization by photopolymerization allowed for study of the time dependence of crystallization. In our experiments we observed that a transient period was required for the crystalline fraction to evolve. This transition depended strongly on spin speed. For example, at ω = 350rpm, ~12 minutes are required to achieve steady state. However, for a spin speed of ω = 1050rpm, steady state is reached in ~0.5 minutes. These times are much shorter than the time required for quiescent crystallization (~720 minutes) shown in Figure 18.

Figure 19 is a shows the dependence of crystal quality on macroscopic strain. Macroscopic strain is defined as the initial sample height divided by the final thickness of the spin coated film (h_0/h). This figure indicates that a macroscopic strain of ~2 is generally sufficient to reach a steady state flow as long as Peclet number is greater than unity. In steady state samples where strain < 2 and Pe > 1 samples remain amorphous.

Spin speed (rpm)	Radial position (mm)	Particle diameter (μm)
200	0.15	1.05
200	0.2	1.05
200	3.125	1.05
350	3.125	1.05
350	3.125	1.05
350	3.125	1.05
350	3.125	1.05
450	0.1	0.79
450	0.125	1.43
450	3.125	1.43
600	0	1.05
600	1.25	1.05
600	3.125	1.43
600	6.25	1.05
600	9.375	1.05
1050	3.125	1.05
1050	3.125	1.05
1050	3.125	1.05

Table 1: experimental design for verification of Peclet number study.

2.5 Discussion

In order for colloidal crystals to be commercially useful, a method must be developed for rapid production of large domain, high-quality crystals with good long range order. Spin coating has potential to be that method. Figure 18 shows that spin coating can be used to fabricate colloidal crystals in times on the order of minutes. Additionally, spin coated crystal formation occurs two orders of magnitude faster than quiescent crystallization. The need for large crystal domains is satisfied by spin coating and limited only by the size of the substrate the spin coater can accommodate. Crystals formed by spin coating have good local ordering shown by the experiments in this chapter and the overall high quality can be confirmed using FTIR and scattering techniques.

Recall that the overall goal of the experiments in this chapter was to understand crystal formation in spin coating using a model developed for simple shear flow. Because stress is not uniform in spin coating we initially expected to have to model spin coating with a sequence of complex transient flows, however, we found that the simple hypothesis of the order to disorder transition at a Peclet number of unity in simple shear is applicable to spin coating.

The results of the experiments in the previous sections confirm that local crystal quality in spin coated samples depended on both the stress-based Peclet number and macroscopic strain. Examining the spin coating Peclet number (equation 4), crystal formation was dependent on particle size, position in the sample, and spin speed. Each of these factors was varied independently and data were combined to produce Figure 17. The Peclet number transition was confirmed by the steep disorder to order transition

that occurred at a Peclet number of order one in figure 16. Therefore, the liquid to solid transition at a Peclet number of unity developed by Ackerson can be used to predict local crystallization in spin coating.

The simple result of the spin coating Peclet number is due to the coupling of two stress-controlled physical processes. At the macroscopic level spin coating is stress controlled because the flow is driven by centrifugal force rather than a moving boundary. Therefore, the local stress is only a function of the spin speed and the film thickness. At the microscopic level, flow-induced crystallization is also stress controlled [60]. Since equation 4 does not depend on the rheology of the system, this theory can be applied to high volume fraction suspensions whose behavior is traditionally difficult to predict because of the effects of aging, jamming, and slow crystallization due to limited diffusion.

Examining Figure 19, we found that crystallization occurs within strains of order 1 for Pe > 1. Because of high strains reported for crystallization in uniform shear , the low strain requirement for crystallization under spin coating came as a surprise. This implication of our study is interesting for future work because previous studies in homogeneous flows have required hundreds to thousands of cycles to form high quality crystalline samples [42].

This result argues that step strain deformation of similar magnitude would also be sufficient to generate colloidal crystallization (provided Pe > 1 and $\Phi > \Phi_C$). The results of the experiments in this chapter thus motivates us to examine the strain criteria for colloidal crystal formation under simple shear flow. This idea will be explored in chapter 3.

One potential source of e

Error in the experiments presented in this chapter is the issue of centering – both on the spin coater and confocal microscope. In microscopic observation of the structures formed, the center of the substrate is determined using the curvature. At low magnifications, the widest point of the arc on the circle can be found in the north, east, south, and west directions. From here the stage is moved to the center of the substrate. The resulting error by the tracking and movement of the confocal stage would be <5μm.

However, because the spin coater cannot be mounted directly on the confocal and analyzed, it is possible that the point found to be the center via confocal microscopy may not correspond to the actual axis of rotation on the spin coater. The wafer was centered on the spin coater using sets of concentric circles to aid in alignment the substrate. Another indicator of the accuracy of the centering was the meniscus (ring) that formed at the edge of the substrate during flow. Upon cessation of flow, if the ring appeared asymmetric in thickness or if the film was not fully covering the substrate in any way the sample was discarded. This eliminated gross errors in centering.

For experiments a substrate 1 inch in diameter was used. Examining Figure 16, at the spin speed of 600rpm with a final film thickness of 40μm, the film is essentially fully crystalline at a radial position of 1mm and Peclet number of order one. Applying this uncertainty to the data, if the axis of rotation on the spin coater was on the order of ±0.5mm from the actual center of the substrate, the Peclet number curves in Figure 17 would be shifted ±500, which would be a significant deviation from the theory. In order for the data to still follow the theory the error must only be of magnitude ±10μm – which is very small.

Because of the repeatability of our results and the small deviations of the curves from each other it appears the point determined to be the center on the confocal is very close to the axis of rotation during the actual experiment. Though this seems unlikely, the data indicate that the center of rotation coincided very closely with the center found by confocal microscopy.

In this chapter, we established that the critical stress criteria for uniform shear flow was applicable to spin coating – a complicated non-uniform shear flow. This gives the prospect for modeling other complex flow induced crystallization processes using simple models. Methods of confocal microscopy combined with fast structural quenching presented in this chapter can be used to study the dynamics of the flow in addition to steady state structures.

2.6 Conclusions

In conclusion, spin coating is a fast way to make high quality multilayer colloidal crystals over large domains. Through experiments we have established spin coating is a stressed controlled process with an order to disorder transition at a Peclet number of unity. Additionally, a strain of two or greater is required for crystal formation.

References

1. Dinsmore, A.D., et al., *Colloidosomes: Selectively permeable capsules composed of colloidal particles*, in *Science*. 2002. p. 1006-1009.
2. Davis, K.E., W.B. Russel, and W.J. Glantschnig, *Settling suspensions of colloidal silica - observations and x-ray measurements*, in *Journal of the Chemical Society-Faraday Transactions*. 1991. p. 411-424.
3. vanBlaaderen, A. and P. Wiltzius, *Growing large, well-oriented colloidal crystals*, in *Advanced Materials*. 1997. p. 833-&.
4. Mezzenga, R., et al., *Understanding foods as soft materials*, in *Nature Materials*. 2005. p. 729-740.
5. Baljon, A.R.C. and M.O. Robbins, *Energy dissipation during rupture of adhesive bonds*, in *Science*. 1996. p. 482-484.
6. Lewis, J.A., *Colloidal processing of ceramics*, in *Journal of the American Ceramic Society*. 2000. p. 2341-2359.
7. Lewis, R. and R.S. Dwyer-Joyce, *Interactions between toothbrush and toothpaste particles during simulated abrasive cleaning*, in *Proceedings of the Institution of Mechanical Engineers Part J-Journal of Engineering Tribology*. 2006. p. 755-765.
8. Hong, L., S.M. Anthony, and S. Granick, *Rotation in suspension of a rod-shaped colloid*, in *Langmuir*. 2006. p. 7128-7131.
9. Cush, R., D. Dorman, and P.S. Russo, *Rotational and translational diffusion of tobacco mosaic virus in extended and globular polymer solutions*, in *Macromolecules*. 2004. p. 9577-9584.
10. Whitesides, G.M. and M. Boncheva, *Beyond molecules: Self-assembly of mesoscopic and macroscopic components*, in *Proceedings of the National Academy of Sciences of the United States of America*. 2002. p. 4769-4774.
11. Horsch, M.A., Z. Zhang, and S.C. Glotzer, *Self-assembly of laterally-tethered nanorods*, in *Nano Letters*. 2006. p. 2406-2413.
12. Graham-Rowe, D., *Tunable structural colour*, in *Nature Photonics*. 2009. p. 551-553.
13. Kubo, S., et al., *Control of the optical properties of liquid crystal-infiltrated inverse opal structures using photo irradiation and/or an electric field*, in *Chemistry of Materials*. 2005. p. 2298-2309.
14. Blaak, R., et al., *Crystal nucleation of colloidal suspensions under shear*, in *Physical Review Letters*. 2004.
15. Pusey, P.N. and W. Vanmegen, *Phase-behavior of concentrated suspensions of nearly hard colloidal spheres*, in *Nature*. 1986. p. 340-342.
16. Chen, L.B., B.J. Ackerson, and C.F. Zukoski, *Rheological consequences of microstructural transitions in colloidal crystals*, in *Journal of Rheology*. 1994. p. 193-216.
17. Russel, W.B. and W.R. Schowalter. 1989: Cambridge University Press.
18. Gasser, U., et al., *Real-space imaging of nucleation and growth in colloidal crystallization*, in *Science*. 2001. p. 258-262.
19. Larson, R.G., *The structure and rheology of complex fluids*. 1999, Oxford: Oxford University Press.

20. Prasad, V., D. Semwogerere, and E.R. Weeks, *Confocal microscopy of colloids*, in *Journal of Physics-Condensed Matter*. 2007. p. 25.
21. Hynninen, A.P., et al., *Cuau structure in the restricted primitive model and oppositely charged colloids*, in *Physical Review Letters*. 2006. p. 4.
22. Royall, C.P., M.E. Leunissen, and A. van Blaaderen, *A new colloidal model system to study long-range interactions quantitatively in real space*, in *Journal of Physics-Condensed Matter*. 2003. p. S3581-S3596.
23. Anderson, V.J. and H.N.W. Lekkerkerker, *Insights into phase transition kinetics from colloid science.* Nature, 2002. **416**(6883): p. 811-815.
24. Auer, S. and D. Frenkel, *Prediction of absolute crystal-nucleation rate in hard-sphere colloids.* Nature, 2001. **409**(6823): p. 1020-1023.
25. Velev, O.D. and S. Gupta, *Materials fabricated by micro- and nanoparticle assembly - the challenging path from science to engineering*, in *Advanced Materials*. 2009. p. 1897-1905.
26. Pronk, S. and D. Frenkel, *Large effect of polydispersity on defect concentrations in colloidal crystals*, in *Journal of Chemical Physics*. 2004. p. 6764-6768.
27. Jiang, P., *Large-scale fabrication of periodic nanostructured materials by using hexagonal non-close-packed colloidal crystals as templates*, in *Langmuir*. 2006. p. 3955-3958.
28. Wang, D.Y. and H. Mohwald, *Template-directed colloidal self-assembly - the route to 'top-down' nanochemical engineering*, in *Journal of Materials Chemistry*. 2004. p. 459-468.
29. Vermant, J. and M.J. Solomon, *Flow-induced structure in colloidal suspensions*, in *Journal of Physics-Condensed Matter*. 2005. p. R187-R216.
30. Jiang, P., et al., *Single-crystal colloidal multilayers of controlled thickness*, in *Chemistry of Materials*. 1999. p. 2132-2140.
31. Zahn, K., J.M. MendezAlcaraz, and G. Maret, *Hydrodynamic interactions may enhance the self-diffusion of colloidal particles*, in *Physical Review Letters*. 1997. p. 175-178.
32. Wen, W.J., L.Y. Zhang, and P. Sheng, *Planar magnetic colloidal crystals*, in *Physical Review Letters*. 2000. p. 5464-5467.
33. Hansen, J.P. and H. Lowen, *Effective interactions between electric double layers*, in *Annual Review of Physical Chemistry*. 2000. p. 209-242.
34. Solomon, T. and M.J. Solomon, *Stacking fault structure in shear-induced colloidal crystallization*, in *Journal of Chemical Physics*. 2006. p. 10.
35. Jiang, P. and M.J. McFarland, *Large-scale fabrication of wafer-size colloidal crystals, macroporous polymers and nanocomposites by spin-coating*, in *Journal of the American Chemical Society*. 2004. p. 13778-13786.
36. Ackerson, B.J., *Shear induced order and shear processing of model hard-sphere suspensions*, in *Journal of Rheology*. 1990. p. 553-590.
37. Ackerson, B.J., *Shear induced order in equilibrium colloidal liquids*, in *Physica A*. 1991. p. 15-30.
38. Ackerson, B.J. and T.A. Morris, *Shear induced order of concentrated dispersions*, in *Better Ceramics through Chemistry Iv*. 1990. p. 159-166.
39. Ackerson, B.J., *Shear induced order and shear processing of model hard-sphere suspensions.* Journal of Rheology, 1990. **34**(4): p. 553-590.

40. W.B. Russel, D.A.S., W.R. Schowalter, *Colloidal dispersions*. 1989, New York City: Press Syndicate of the University of Cambridge. 525.
41. Ackerson, B.J. and P.N. Pusey, *Shear-induced order in suspensions of hard-spheres.* Physical Review Letters, 1988. **61**(8): p. 1033-1036.
42. Bender, J. and N.J. Wagner, *Reversible shear thickening in monodisperse and bidisperse colloidal dispersions.* Journal of Rheology, 1996. **40**(5): p. 899-916.
43. Jiang, P. and M.J. McFarland, *Large-scale fabrication of wafer-size colloidal crystals, macroporous polymers and nanocomposites by spin-coating.* Journal of the American Chemical Society, 2004. **126**(42): p. 13778-13786.
44. Emslie, A.G., F.T. Bonner, and L.G. Peck, *Flow of a viscous liquid on a rotating disk*, in *Journal of Applied Physics*. 1958. p. 858-862.
45. Meyerhofer, D., *Characteristics of resist films produced by spinning*, in *Journal of Applied Physics*. 1978. p. 3993-3997.
46. Ackerson, B.J. and P.N. Pusey, *Shear-induced order in suspensions of hard-spheres*, in *Physical Review Letters*. 1988. p. 1033-1036.
47. Solomon, M.J. and M. Kogan, in *Encyclopedia of Condensed Matter Physics*.
48. Ackerson, B.J., *Shear induced order anad shear processing of model hard-sphere suspensions*, in *Journal of Rheology*. 1990. p. 553-590.
49. Ackerson, B.J. and N.A. Clark, *Shear-induced melting*, in *Physical Review Letters*. 1981. p. 123-126.
50. Emslie, A.G., F.T. Bonner, and L.G. Peck, *Flow of a viscous liquid on a rotating disk.* Journal of Applied Physics, 1958. **29**(5): p. 858-862.
51. Antl, L., et al., *The preparation of poly(methyl methacrylate) lattices in nonaqueous media.* Colloids and Surfaces, 1986. **17**(1): p. 67-78.
52. Pathmamanoharan, C., K. Groot, and J.K.G. Dhont, *Preparation and characterization of crosslinked pmma latex particles stabilized by grafted copolymer.* Colloid and Polymer Science, 1997. **275**(9): p. 897-901.
53. Campbell, A.I. and P. Bartlett, *Fluorescent hard-sphere polymer colloids for confocal microscopy.* Journal of Colloid and Interface Science, 2002. **256**(2): p. 325-330.
54. Bosma, G., et al., *Preparation of monodisperse, fluorescent pmma-latex colloids by dispersion polymerization.* Journal of Colloid and Interface Science, 2002. **245**(2): p. 292-300.
55. Scully, P.J., et al., *Uvc laser photo-induced refractive index changes in poly-methyl-meth-acrylate and plastic optical fibres for application as sensors and devices.* 14th International Conference on Optical Fiber Sensors, 2000. **4185**: p. 854-857.
56. Solomon, M.J. and M. Kogan, *Confocal optical microscopy*, in *Encyclopedia of condensed matter physics*
2005, Oxford Academic Press.
57. tenWolde, P.R., M.J. RuizMontero, and D. Frenkel, *Numerical calculation of the rate of crystal nucleation in a lennard-jones system at moderate undercooling.* Journal of Chemical Physics, 1996. **104**(24): p. 9932-9947.
58. Blaaderen, v.
59. Ackerson, B.J., *Shear induced order anad shear processing of model hard-sphere suspensions.* Journal of Rheology, 1990. **34**(4): p. 553-590.

60. Shereda, L.T., R.G. Larson, and M.J. Solomon, *Local stress control of spatiotemporal ordering of colloidal crystals in complex flows.* Physical Review Letters, 2008. **101**(3).
61. Krishnamurthy, L.N., N.J. Wagner, and J. Mewis, *Shear thickening in polymer stabilized colloidal dispersions.* Journal of Rheology, 2005. **49**(6): p. 1347-1360.
62. Gasser, U., *Crystallization in three- and two-dimensional colloidal suspensions.* Journal of Physics-Condensed Matter, 2009. **21**(20): p. 24.
63. Ackerson, B.J., *Shear induced order in equilbrium colloidal liquids* in *Physica A*. 1991. p. 15-30.
64. Vermant, J. and M.J. Solomon, *Flow-induced structure in colloidal suspensions.* Journal of Physics-Condensed Matter, 2005. **17**(4): p. R187-R216.
65. Chen, L.B., B.J. Ackerson, and C.F. Zukoski, *Rheological consequences of microstructural transitions in colloidal crystals* Journal of Rheology, 1994. **38**(2): p. 193-216.
66. Wagner, N.J. and B.J. Ackerson, *Analysis of nonequilibrium structures of shearing colloidal suspensions.* Journal of Chemical Physics, 1992. **97**(2): p. 1473-1483.
67. Wu, Y.L., et al., *Melting and crystallization of colloidal hard-sphere suspensions under shear.* Proceedings of the National Academy of Sciences of the United States of America, 2009. **106**(26): p. 10564-10569.
68. Ackerson, B.J., *Shear induced order and shear processing of model hard-sphere suspensions*, in *Journal of Rheology*. 1990. p. 553-590.
69. Holmqvist, P., et al., *Crystallization kinetics of colloidal spheres under stationary shear flow.* Langmuir, 2005. **21**(24): p. 10976-10982.
70. Butler, S. and P. Harrowell, *Kinetics of crystallization in a shearing colloidal suspension*, in *Physical Review E*. 1995. p. 6424-6430.
71. Ackerson, B.J. and N.A. Clark, *Sheared colloidal suspensions*, in *Physica a-Statistical Mechanics and Its Applications*. 1983. p. 221-249.
72. Ackerson, B.J. and T.A. Morris, *Shear induced order of concentrated suspensions*, in *Better Ceramics through Chemistry Iv*. 1990. p. 159-166.
73. Ackerson, B.J., *Shear induced order in equilbrium colloidal liquids* in *Physica A*. 1991. p. 15-30.
74. Derks, D., et al., *Dynamics of colloidal crystals in shear flow.* Soft Matter, 2009. **5**(5): p. 1060-1065.
75. Gasser, U., *Crystallization in three- and two-dimensional colloidal suspensions*, in *Journal of Physics-Condensed Matter*. 2009. p. 24.
76. Cohen, I., et al., *Slip, yield, and bands in colloidal crystals under oscillatory shear.* Phys Rev Lett, 2006. **97**(21): p. 215502.
77. Derks, D., et al., *Dynamics of colloidal crystals in shear flow*, in *Soft Matter*. 2009. p. 1060-1065.
78. Ackerson, B.J. and P.N. Pusey, *Shear-induced order in suspensions of hard-spheres* Physical Review Letters, 1988. **61**(8): p. 1033-1036.
79. Davis, K.E., W.B. Russel, and W.J. Glantschnig, *Settling suspensions of colloidal silica - observations and x-ray measurements.* Journal of the Chemical Society-Faraday Transactions, 1991. **87**(3): p. 411-424.

80. Pusey, P.N. and W. Vanmegen, *Phase-behavior of concentrated suspensions of nearly hard colloidal spheres.* Nature, 1986. **320**(6060): p. 340-342.

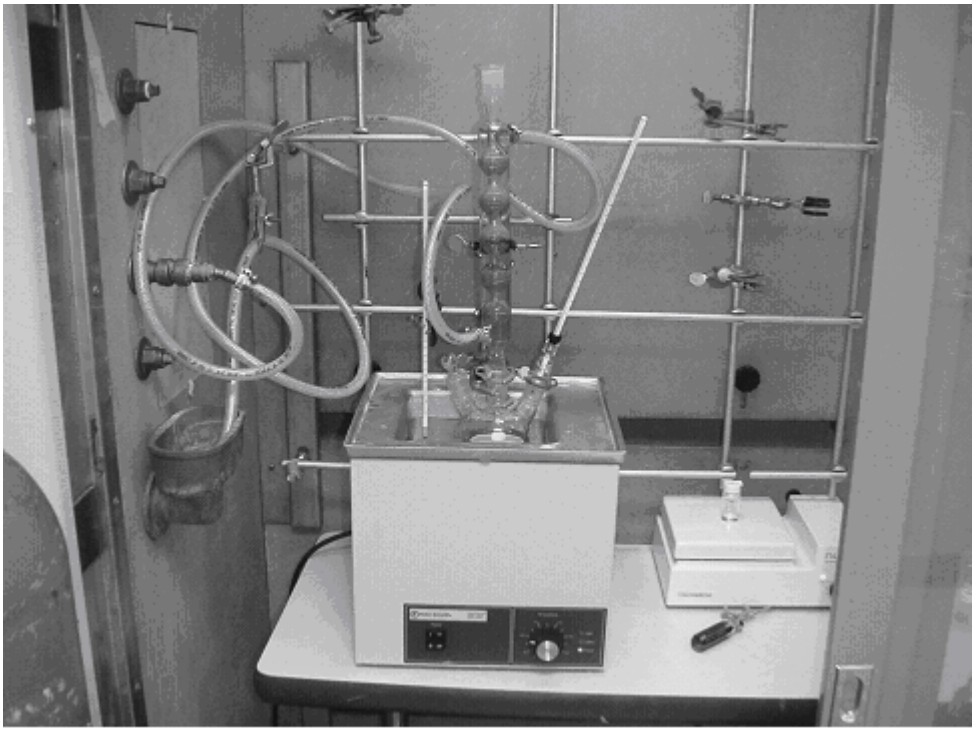

Figure 2. Setup for PMMA dispersion polymerization synthesis.

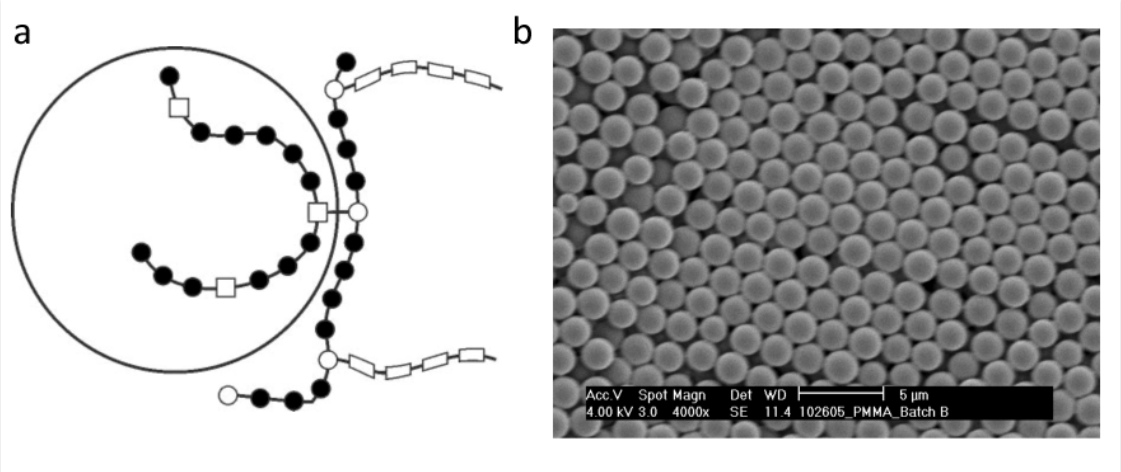

Figure 3. (a) Schematic representation of a PMMA-latex particle with poly(12-hydroxystearic acid) stabilizer, adapted from Bosma et. al[i]. Methyl methacrylate (●); methacrylic acid (□); glycidyl methacrylate (○); 12-hydroxystearic acid (▫);(b) SEM image of a typical batch of PMMA particles[10].

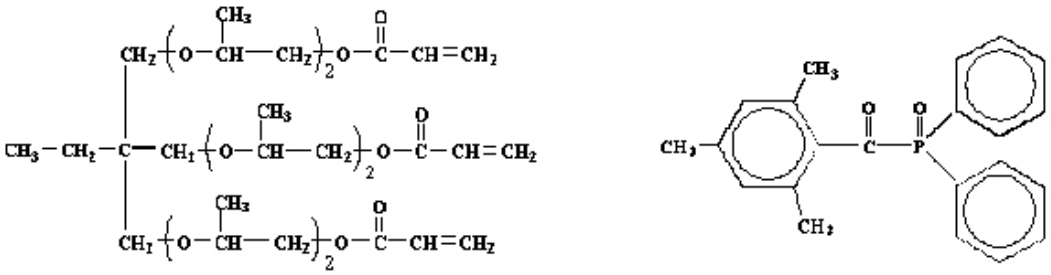

Figure 4. Chemical structure of (a) the photopolymer propoxylated (6) trimethylolpropane triacrylate (CD501, Sartomer) and (b) phosphine oxide (Irgacure 2100, Ciba Specialty) the initiator.

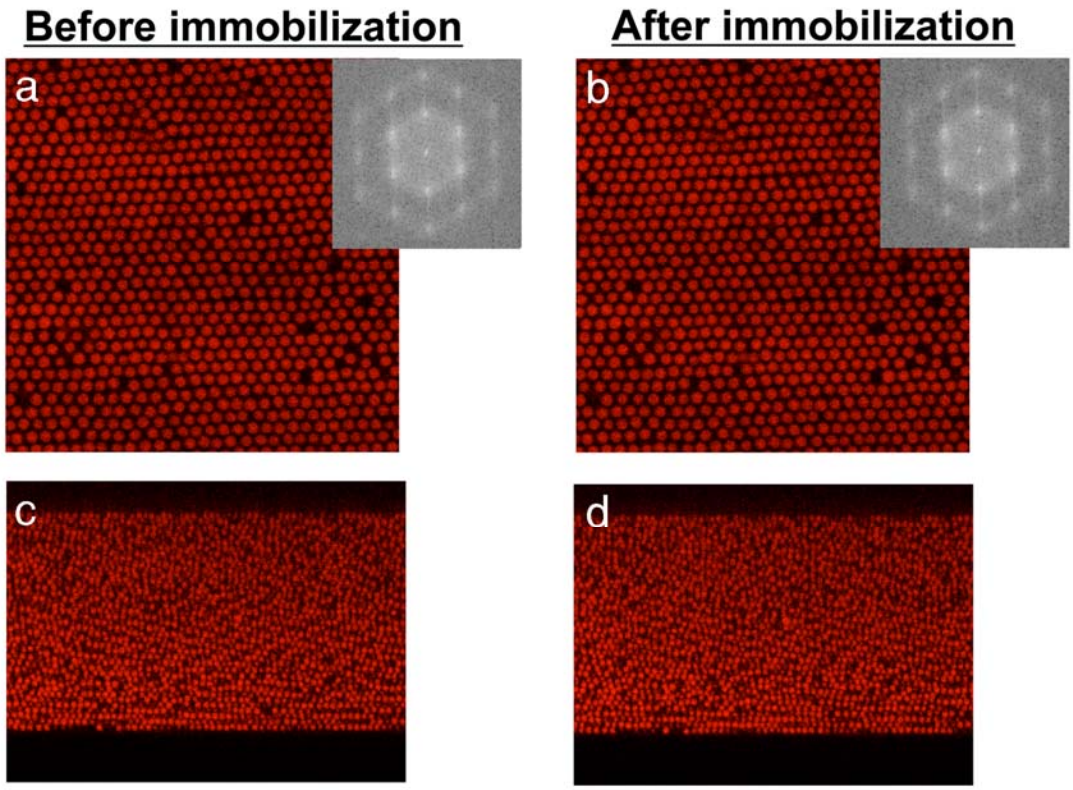

Figure 5. Evaluation of the photopolymerization process (a) xy confocal image 30µm above the substrate before photopolymerization (b) xy confocal image of the same location after photopolymerization.(c) xz confocal image (normal to the substrate) of full sample thickness before photopolymerization (b) xz confocal image of the same location after photopolymerization.

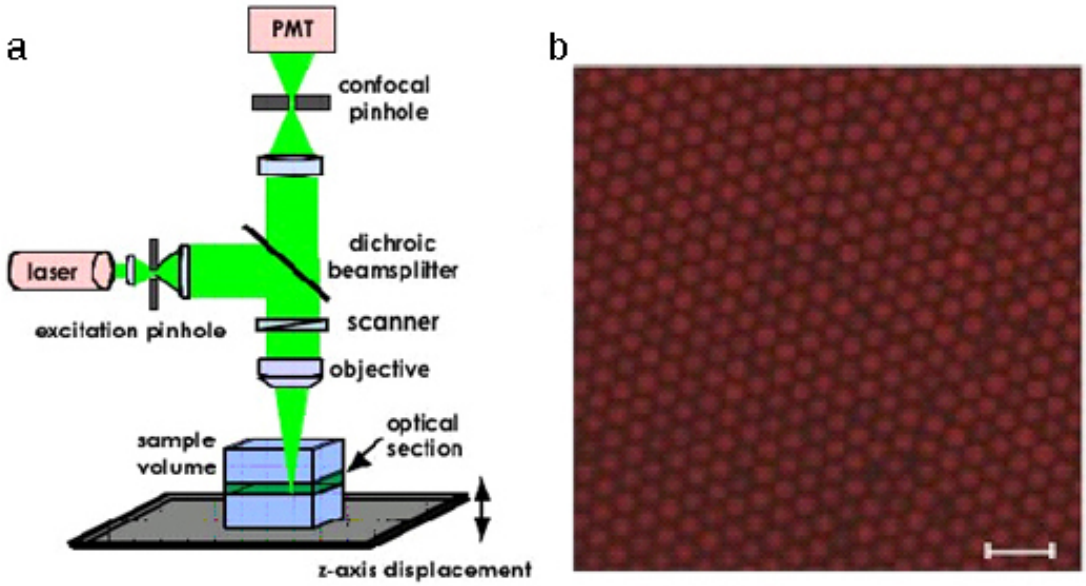

Figure 6. (a) schematic drawing of a scanning confocal microscope [12] (b) sample confocal image 30μm above the substrate.

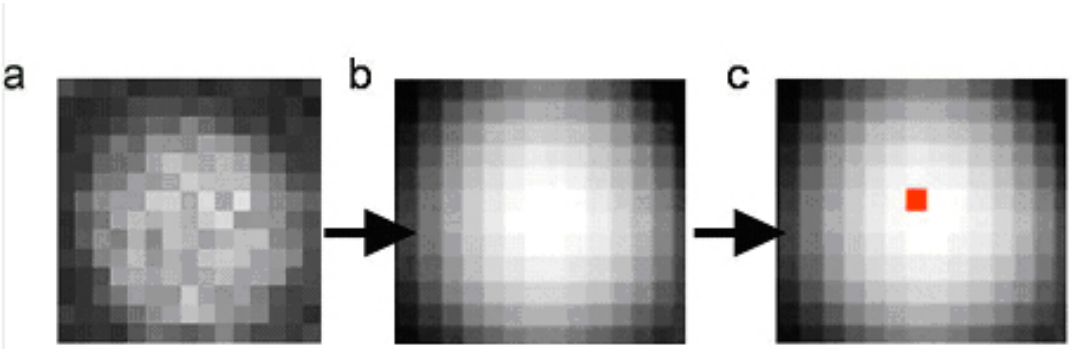

Figure 7. Particle location algorithm (a) raw confocal image (b) Gaussian filtered (c) centroid location.

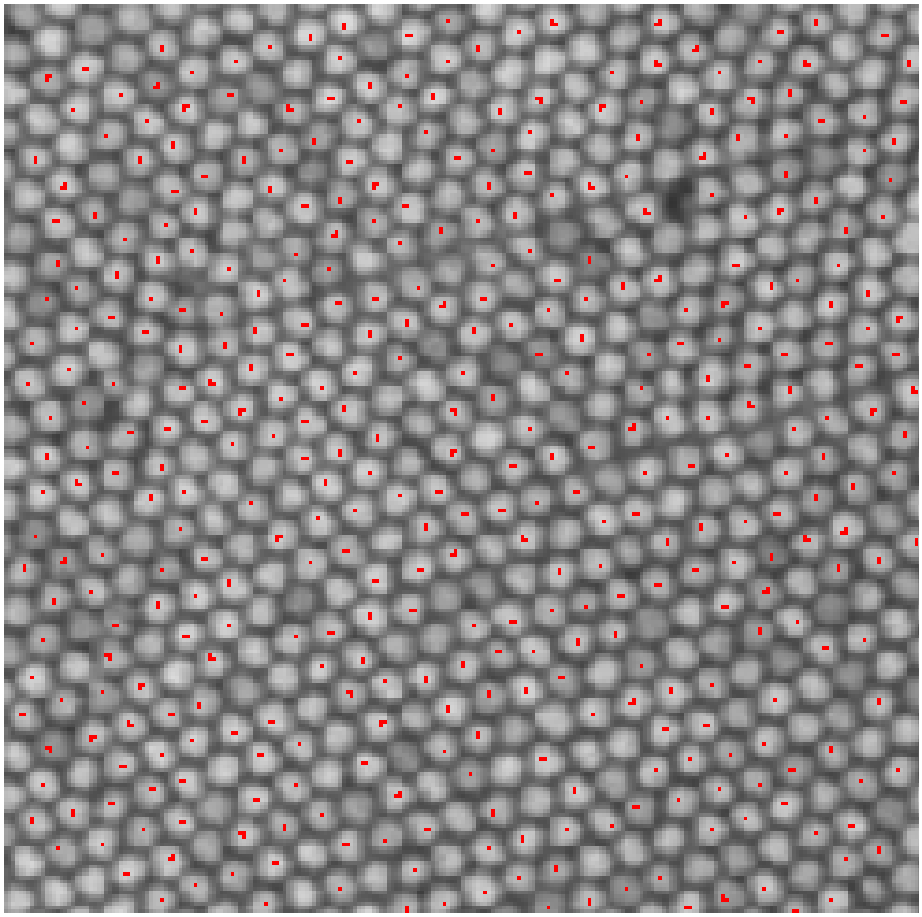

Figure 8. Overlay image of a typical xy confocal image. Red dots represent particle centroids located by the image processing algorithm.

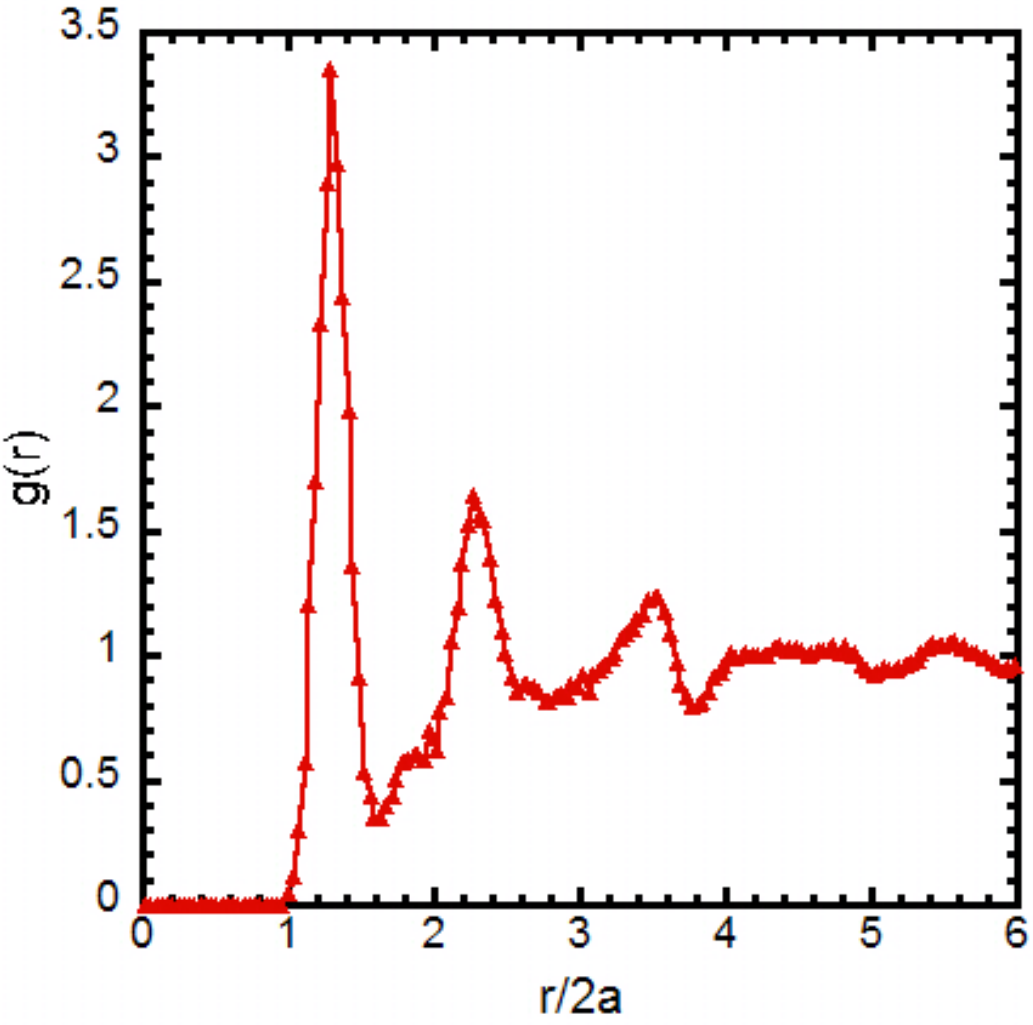

Figure 9. Plot of the pair correlation function for a typical sample

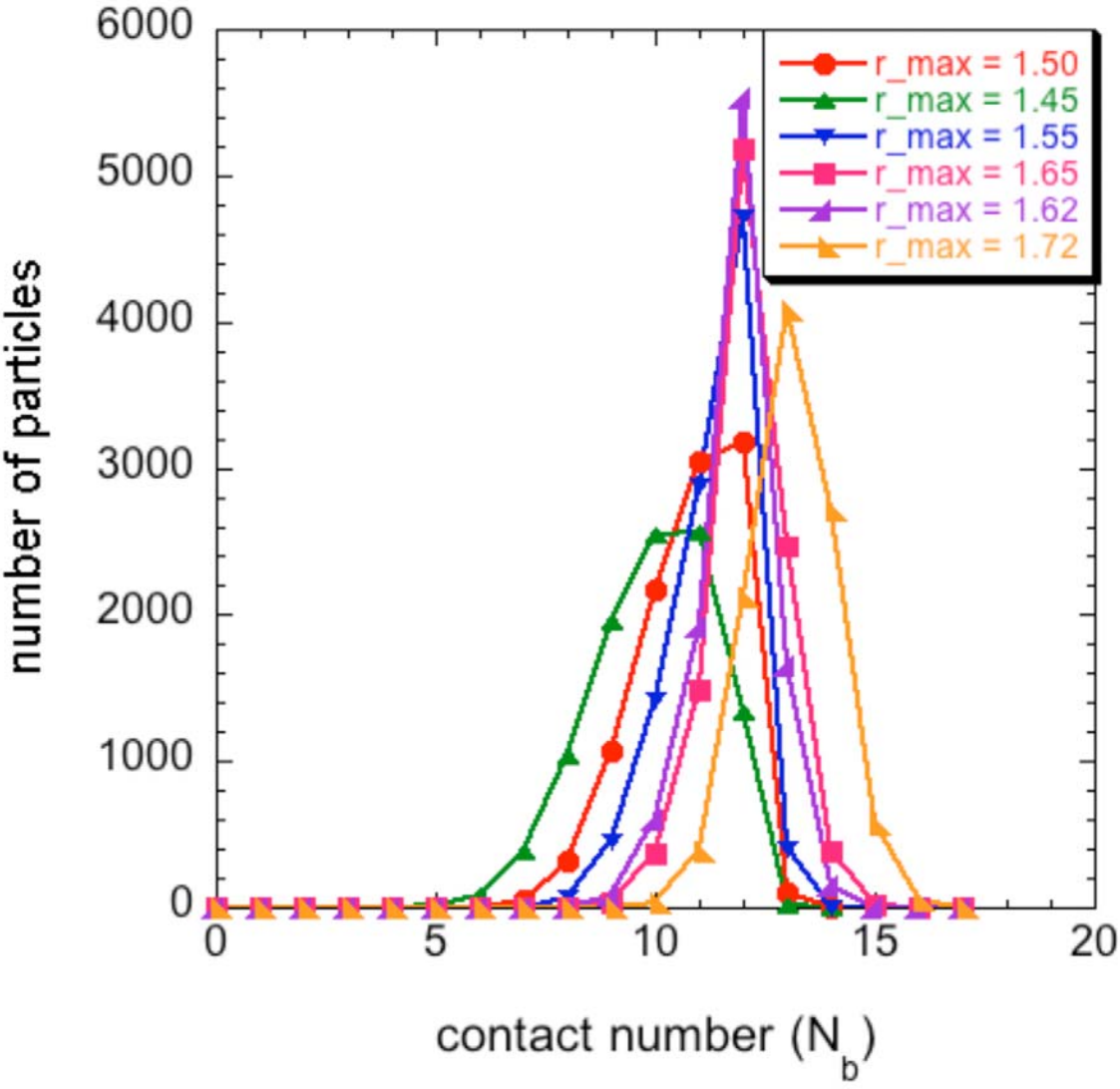

Figure 10. Selection of r_max. 1.62 is the first minimum of g(r)

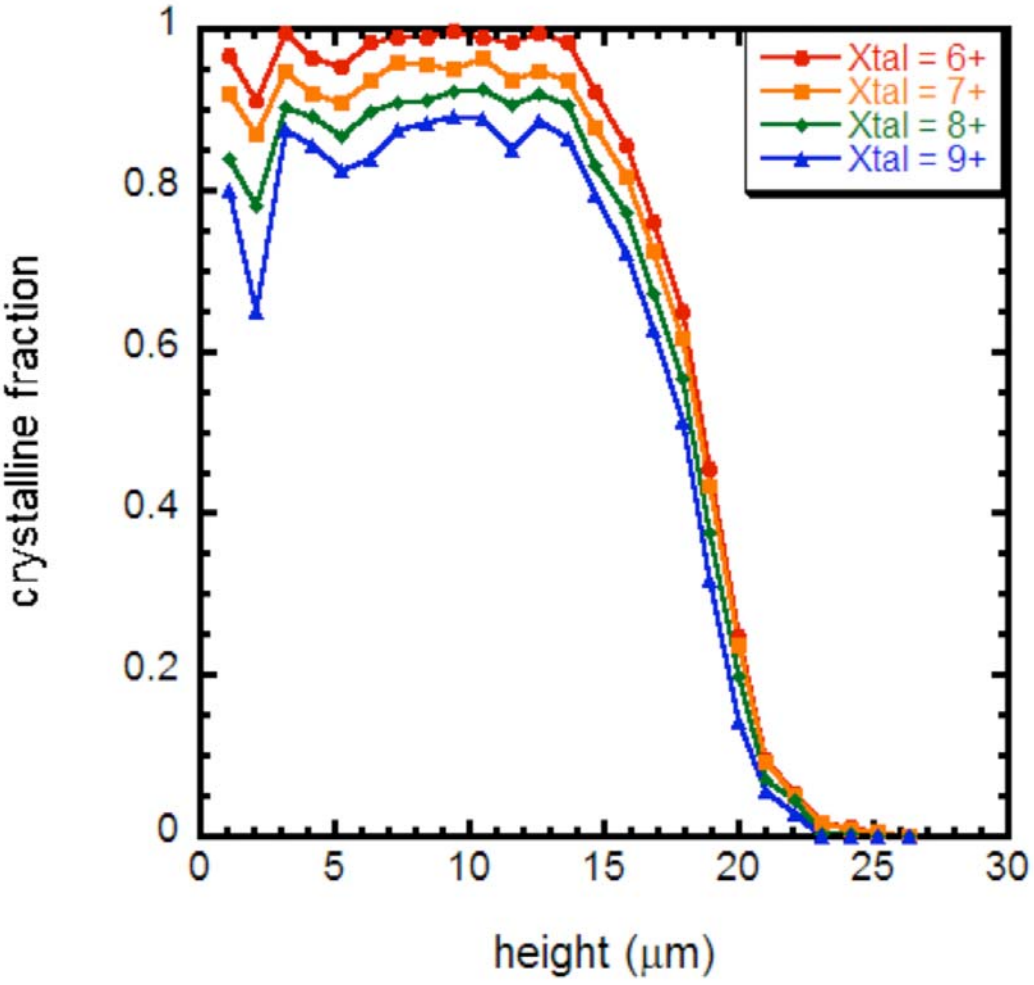

Figure 11. Number of crystalline bonds as a function of height in the sample for different definitions of crystallinity.

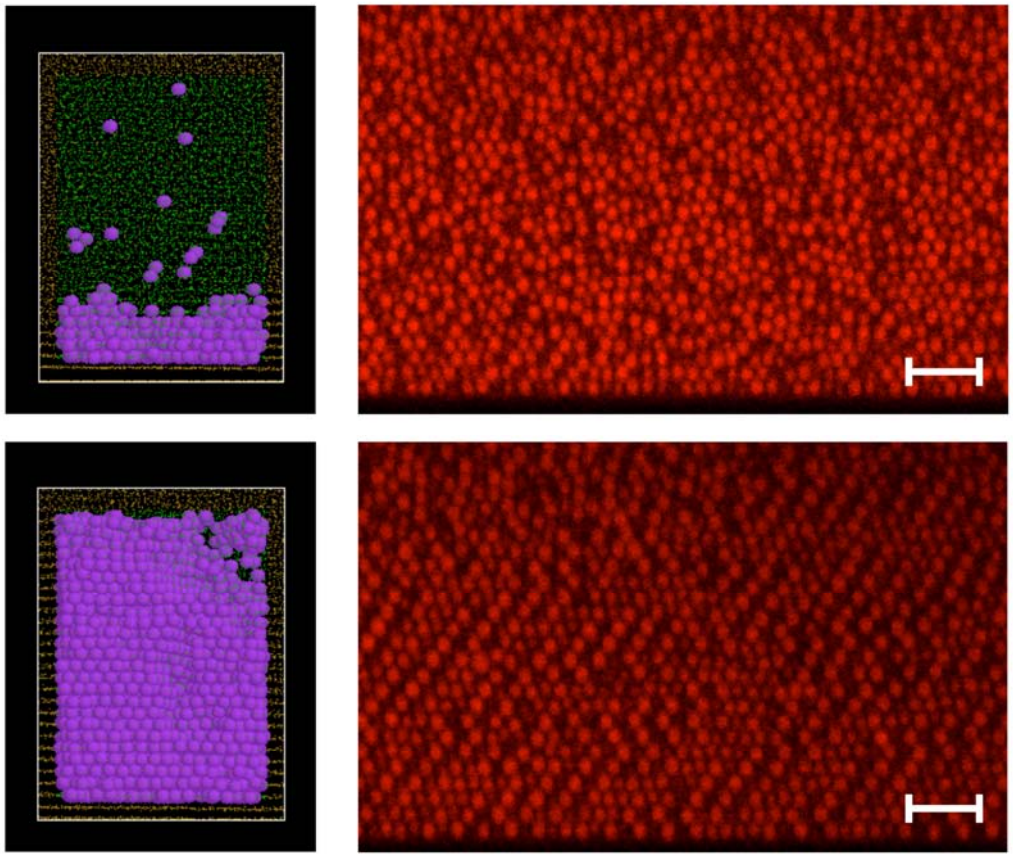

Figure 12. (a) Rasmol rendering of the amorphous sample (b) xz confocal image of amorphous sample (c) Rasmol rendering of the crystalline sample (d) xz confocal image of crystalline sample.

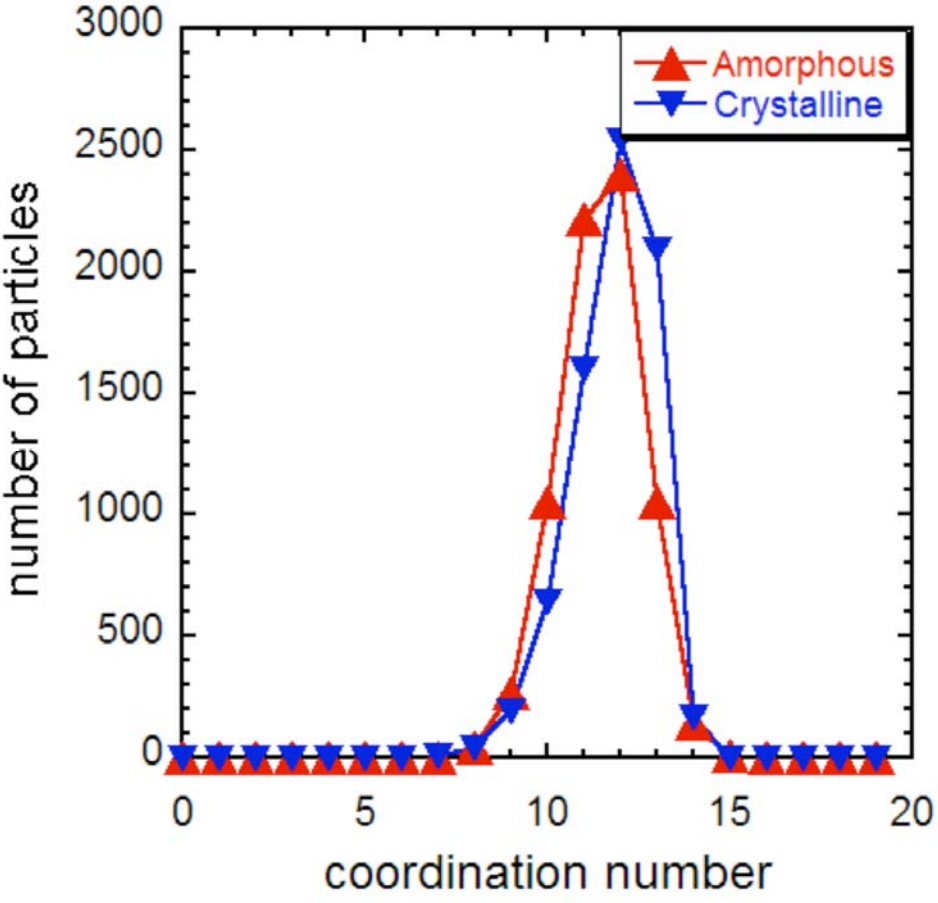

Figure 13. coordination number distribution for the amorphous and crystalline test cases shown in figure 11.

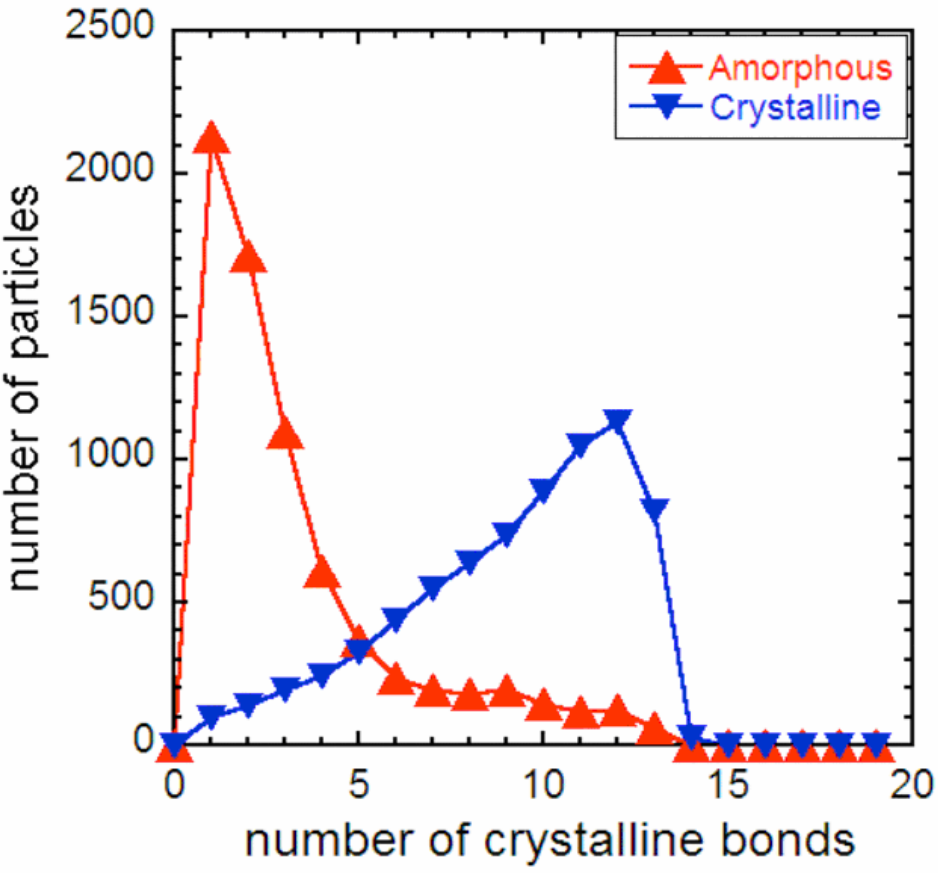

Figure 14. Number of crystalline bonds distribution for the amorphous and crystalline test cases shown in figure 11.

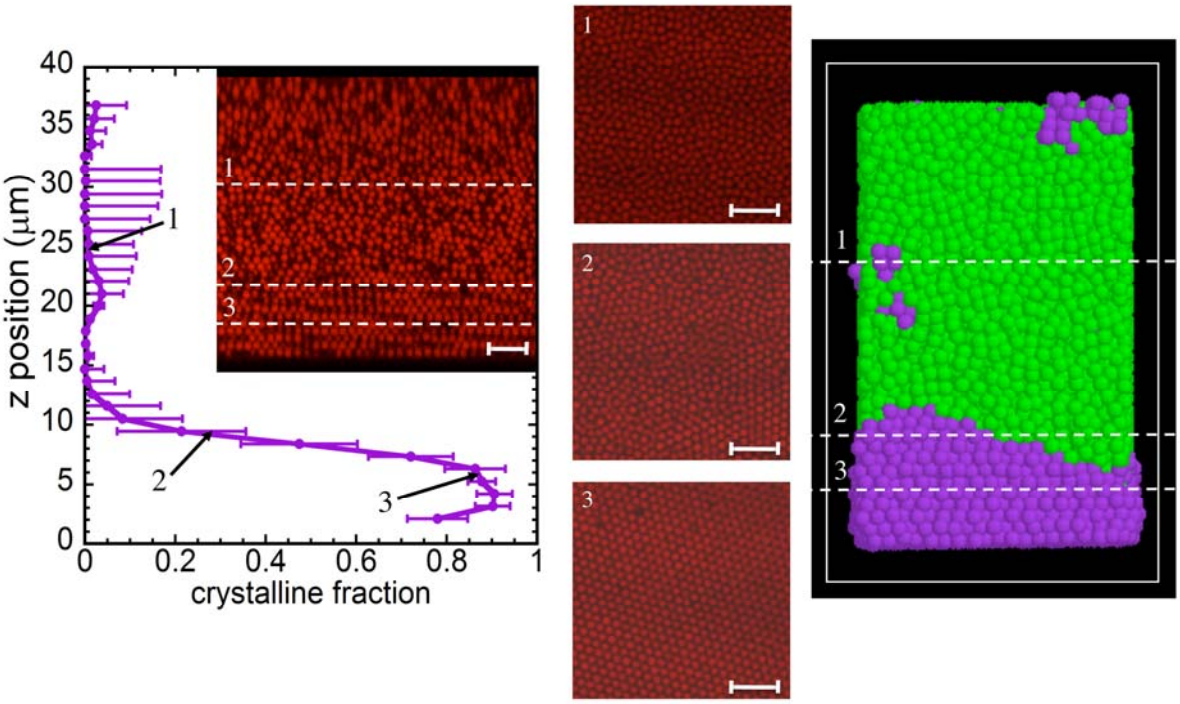

Figure 15. Axial variation in crystal quality. Samples were spin coated for 3 minutes at 600rpm. Images are r* = r/R = 0.0025 from axis of rotation. (a) plot of the crystalline fraction as a function of height in the sample (b) corresponding xz image (c) rasmol rendering of sample. The numbers 1-3 correspond to heights indicated by the arrows in (a) and the three xy images. Scale bars is are 5μm, film thickness is 41μm. Crystalline particles are purple and non-crystalline particles are green.

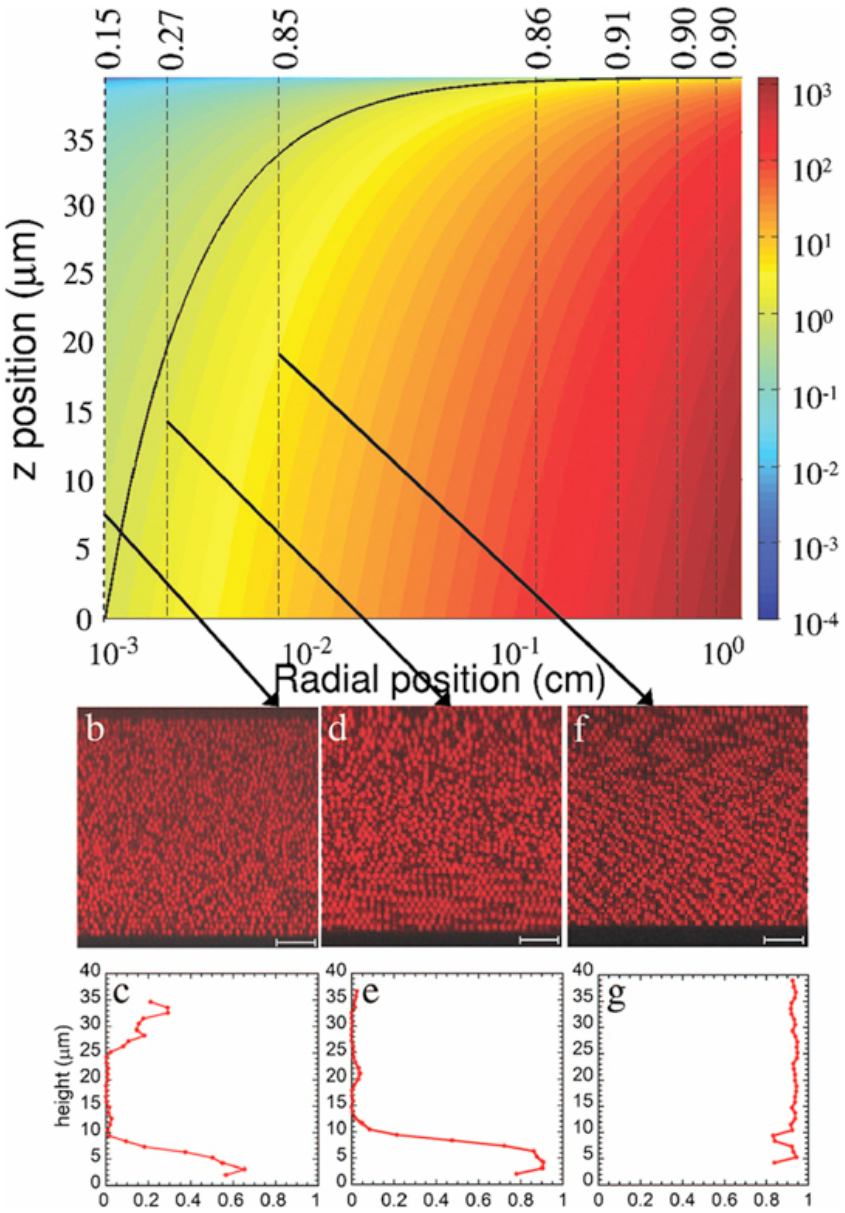

Figure 16. (a) Plot of Peclet number (color scale indicated at right) as a function of both radial and axial position in a spin-coated sample (! " 600 rpm, t " 3 min). The curve represents Peclet number of unity: dotted lines represented radii where crystal quality was investigated, and the average crystalline fraction at each of these radii is given above the corresponding line. (b), (d), (f) are 2D confocal micrographs imaged perpendicular to the substrate at radii of 0.00 m, 0.031 mm, and 0.625 mm, respectively. Arrows from (a) to these images show the corresponding radii and crystalline fractions on the plot. (c), (e), and (g) are plots of crystal quality vs z position corresponding to images (b), (d), and (f). All scale bars represent 5 μm.

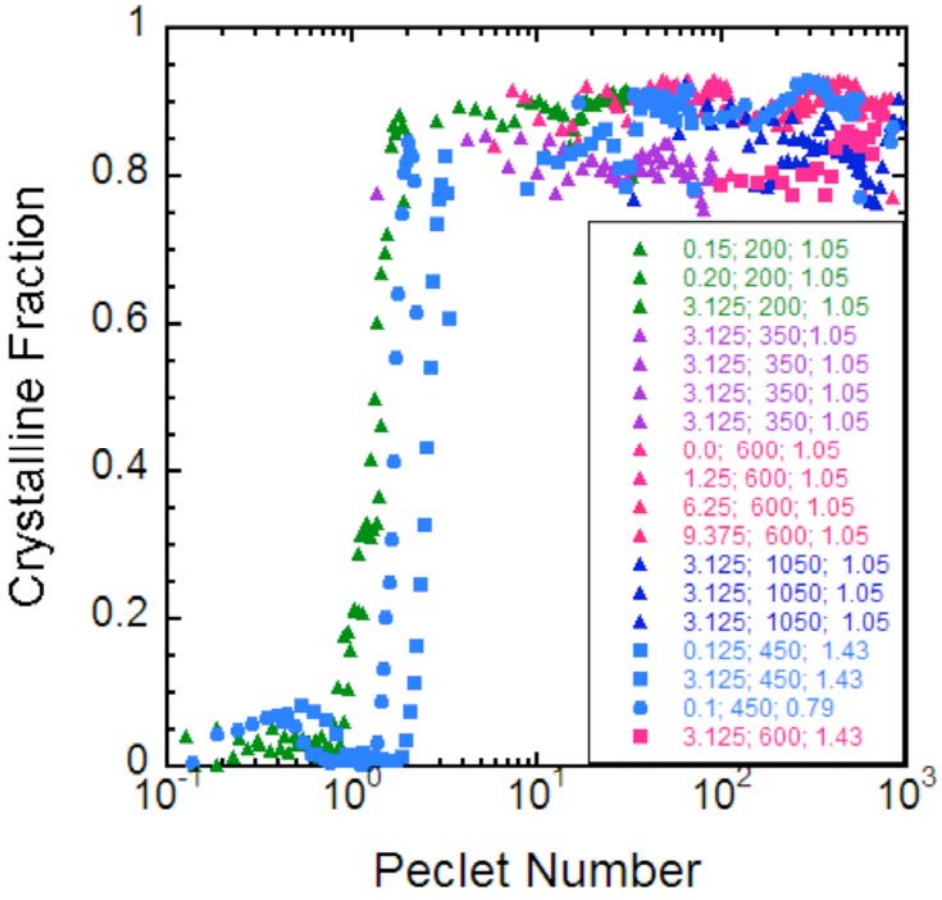

Figure 17. Plot of crystalline fraction vs local Peclet number for various particle sizes and spin speeds. The ordered triplet of values in the legend shows sample fabrication conditions of (radial position(mm); spin speed; particle diameter). Different colors represent spin speeds (200–1050 rpm) and different shapes denote different particle sizes.

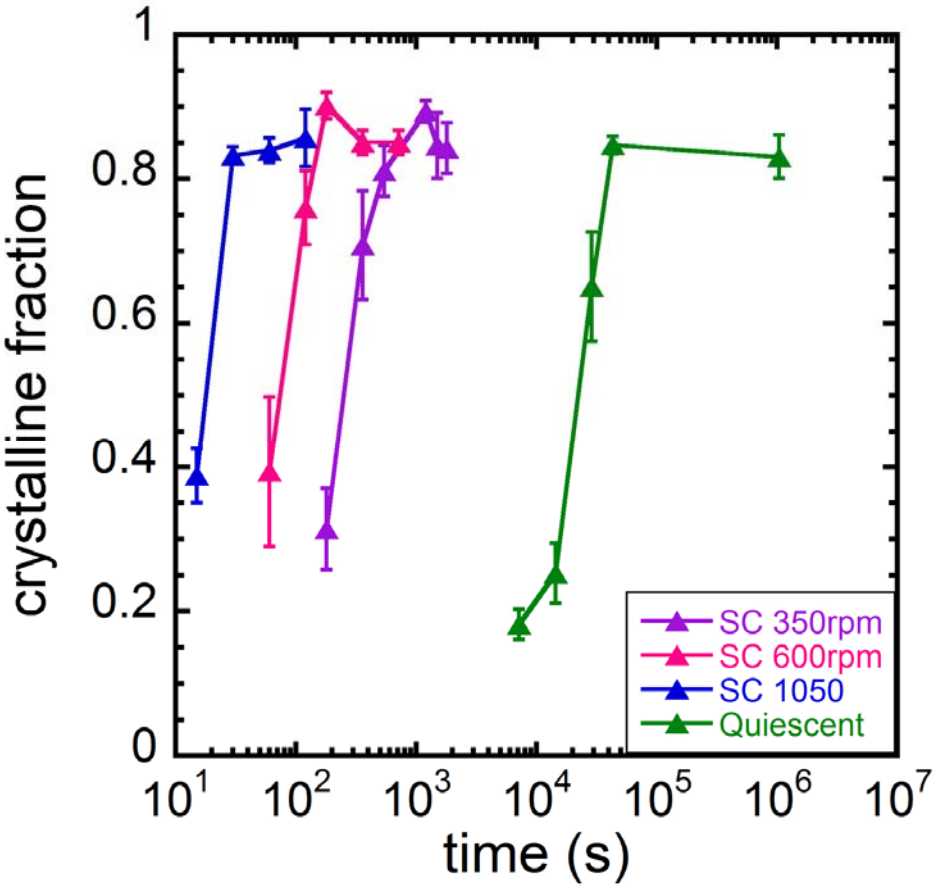

Figure 18. Comparison of time required for spin coating and quiescent crystallization of 35% samples. Spin speed of 350, 600, and 1050rpm are represented.

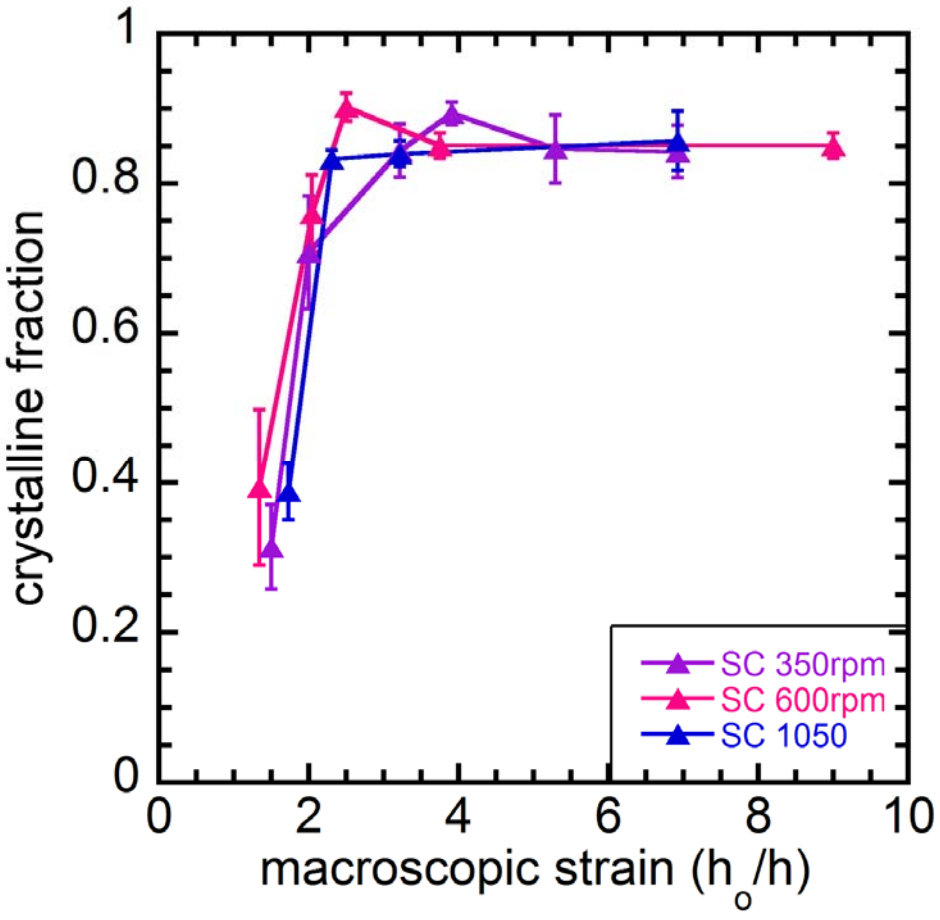

Figure 19. Plot of crystal quality as a function of macroscopic strain; the inset is a plot of crystalline fraction as a function of time for both spin-coated and quiescent samples. All experiments were imaged at r* " r=R " 0:25. Data for spin speeds of 350, 600, and 1050 rpm are shown.

CHAPTER 3

Stress and strain criteria for crystallization of concentrated colloidal suspensions undergoing step strain shear deformation

3.1 Chapter Summary

With application of simple shear flow, concentrated colloidal suspensions show shear thinning and shear thickening rheological behaviors that are of fundamental interest to colloidal crystal formation under shear flow [61]. Because of an indication from recent work [60] that crystallization occurs given only small strains in the non-uniform flow of spin coating, we here study their structural response to step strain deformation. Suspensions composed of 35% poly(methyl methacrylate) (PMMA), 7% photopolymer, 1% initiator in dioctyl phthalate (DOP) were sheared in a parallel plate assembly with a stationary bottom plate and a top plate moved by a stepper motor. Confocal microscopy was used to directly visualize and analyze both dynamic and structural transformations under flow. In this chapter we quantify the effect of strain and shear rate (Peclet number) on local crystallinity in simple shear flow. Additionally, we characterize the strain dependence of the velocity profile and correlate its shape and the movement of the crystalline boundary. We compare these data to the stress and strain criteria for crystal formation developed in our previous spin coating study.

3.2 Introduction

Above a critical volume fraction, dense colloidal suspensions undergo phase transitions in order to minimize free energy. Equilibrium crystallization has been studied extensively in model colloid systems [62]. Under equilibrium conditions, clusters of particles form preferentially on point defects as described by classical nucleation theory [62]. The rate of crystallization is determined solely by thermodynamics and interparticle interactions[1]. To accommodate interparticle forces, particles rearrange themselves into their most energetically favorable configuration.

In contrast to equilibrium crystallization, non-equilibrium crystallization is not well characterized. One aspect of non-equilibrium crystallization involves the study of phase transition kinetics resulting from the combination of interparticle interactions and hydrodynamic forces. The complicated dynamics and typically fast flows make it difficult to study non-equilibrium phase transitions. Additional complexity arises from the fact that phases formed under flow are often metastable and transient [62]. However, improved understanding can contribute to prediction of phase behavior and creation of advanced materials.

In non-equilibrium systems crystal growth is accelerated by an applied flow and the rate of crystal formation depends strongly on the strength of the applied field [63]. Application of flow leads to rich sequences of microstructural transitions and metastable phases that do not occur under equilibrium conditions [64]. In this chapter we study non-equilibrium phase transitions in concentrated colloidal suspensions under simple shear flow,

Application of shear to dense colloidal suspensions results in rheological changes such as shear thickening and shear thinning [65]. Shear banding may also be observed [66]. Because the macroscopic properties of the system are coupled to the sample microstructure, in order to understand the effect of an applied field it is important to study both. Conceivably, understanding these transitions may lead to better control of structures produced. This added control may lead to creation of advanced materials[67].

Light, x-ray, and small angle scattering have been used in most studies of crystallization kinetics to date [63]. These data provided global ensemble averaged information of samples at steady, though transient measurements are possible if the signal to noise ratio is favorable. Measurements have extracted the unit cell and average stacking probability from intensity modulation of the diffraction patterns from the periodicity of the crystal [68]. Brownian dynamics and Monte Carlo simulations have been performed for dense colloidal suspensions[69]. Studies have reported contradicting results indicating both that shear enhances the rate of crystallization and that it hinders it [69].

Much of what is known about accelerated crystallization kinetics and microstructure was reported by Ackerson et al. [67]. Ackerson described four basic non-equilibrium structures: liquid-like, string-like, sliding layers, and face centered cubic[1, 67]. He established that at low to moderate shear rates particles align into layers which slip easily past one another. Under simple shear flow he proposed that the order to disorder transition was dependent on the dimensionless Peclet number[67]. For suspensions with volume fractions above the freezing transition, a Peclet number of one

is required to induce crystallization. However, at sufficiently large Peclet numbers (Pe order 1E4) the layer structure is destroyed by the shear melting[66].

Ackerson et al. [1, 70, 71] determined global, steady-state structure of sheared samples using scattering techniques. In contrast, we here characterize local crystal structure and dynamics using direct visualization techniques. This allowed non-steady state analysis and a method to understand formation of metastable phases. Since the crystallization acceleration Peclet number theory for shear flow has been tested extensively, we will use Peclet numbers above unity and vary the distance the top plate travels to vary strain.

From previous work on spin coating [60] we determined that surprisingly low strains were sufficient for crystal formation. In the previous chapter it is reported that crystallization occurs under spin coating at a macroscopic strain of two. Spin coating and simple shear represent non-uniform and uniform shear flows respectively. Since both systems obeyed the shear disorder to order transition at Peclet number of one criterion, we proceeded to determine the strain requirements for shear-induced crystallization under simple shear flow and compared these to spin coating data. Determination of strain requirements were achieved by direct visualization of step strain deformation in a parallel plate shear cell via confocal microscopy and analysis of the resulting structures using image processing techniques described in section 2.2.6.

This chapter explores the effect of step strain at different Peclet numbers in dense colloidal systems. The velocity profile and microstructure was characterized by direct visualization.

3.3 Experimental methods

35% poly(methyl methacrylate) suspensions were subjected to step strain deformation in a parallel plate shear cell mounted on a scanning confocal microscope. The resulting structures were imaged in stacks of xy images at evenly spaced intervals in the z direction. Crystal quality was assessed for each sample using the image processing methods described previously. The experiments in the sections that follow characterize the effect of step strain deformation on the velocity profile and on overall crystal quality.

Particle synthesis and characterization were carried out in the methods described in the chapter two. Solution compositions for the experiments in this chapter are 35% by volume PMMA (d_p = 0.68 μm, polydispersity = 2.3%), 7% photopolymer, 1% photoinitiator in DOP and 11μM TBAC. Samples were imaged on the Leica SP2 confocal microscope(100x) and photopolymerization and structural analysis were also carried out as described in chapter 2.

3.3.1 Shear cell specifications

The shear cell was a parallel plate device constructed to be mounted on a Leica SP2 inverted confocal microscope. This device allowed direct visualization of both dynamics of colloidal samples under shear flow and the final structures formed. A basic schematic diagram of the shear cell from both the top and side are shown in

Figure . Design specifications are given in table 2.

	Minimum	Maximum
Velocity (μm/s)	3	10,000
Shear rate (s^{-1})	1.00E-02	1.00E+02
Peclet number	1	1.00E+04
Strain amplitude	---	67

Table 2: shear cell specifications at a gap of 150μm and particle diameter of 0.68μm.

The shear cell was a plate-plate geometry with a stationary bottom plate and a moveable top plate. The bottom plate was a glass coverslip (Fisherbrand #1, 40mm x 22mm) approximately 0.17mm thick and the top was a piece of 1/8“ thick plate glass.

The top plate was driven by a precision 5-phase stepper motor (PMM3B2, Oriental motor company ltd) mounted on a slider (537233, Coherent) to ensure smooth, precise movement at low strains. The height of the top plate was adjusted using a micrometer. The angle of the bottom plate was adjusted using the two setscrews and micrometer.

LabMotion v1.0 software from LabView was used to control the movement of the stepper motor. Programs for simple steady or oscillatory shear were written though steady shear was used preferentially for this study. A sample protocol for a step strain experiment is shown in appendix C.

3.3.2 Shear experiment setup

To mount the coverglass on the bottom of the shear cell surface, the edges of the bottom coverglass were coated with a thin layer of UV glue (Dymax, GB341UV), centered, and pressed firmly on the stainless steel block. The plate was exposed to 15W UV light (365nm) for 30 seconds, though immobilization required < 1 second. The top plate was pinned to the surface of cantilever setup using two setscrews.

The shear cell was loaded by depositing 3-4 drops (~30uL) of the suspension on the bottom plate. The top plate was lowered slowly using the micrometer until the suspension fully wetted the bottom surface. The condenser and *xyz* stage were removed from the confocal microscope and the 100x objective was lowered. The shear cell was

aligned on the stage so the open area below the bottom plate was centered over the objective. Because the *xyz* stage was removed to mount the shear cell, to change position in the *xy* plane, the objective was lowered and the cell was lifted and moved to a new location.

3.3.3 Setting the gap

After the shear cell was mounted on the confocal the z position of the bottom of the sample was brought into focus. The objective was raised 150μm from the focus by slowly turning the micrometer move the top plate until the top of the sample was 150μm above the bottom surface. The gap was verified by confirming the positions of the bottom and top of the sample to making sure no shifting had occurred by moving the micrometer.

After setting the gap the motor mounted on the shear cell was attached to the controller.

3.3.4 Parallel plate alignment

To prevent lubrication flows and drift the plates had to be precisely aligned with each other and approximately parallel to the object plane of the microscope. The method of droplet wetting was used to align the plates parallel with respect to each another. A droplet of de-ionized water was placed in the center of the bottom plate and the top plate was lowered slowly using the micrometer until the top plate made contact with the droplet the lowered further until the surface was completed wetted. In uniform wetting, when the top plate touched the droplet it appeared as a small circle at the center

of the slide. As the plate was lowered the droplet remained centered and the circle expanded evenly in all directions. Figure 20 is a sketch showing uniform wetting. If wetting was non-uniform, the top plate was raised and the bottom plate angle was adjusted. This process was repeated until the droplet uniformly wetted the surface within +/- 0.5mm.

Figure 20. Schematic of uniform droplet wetting. Images from left to right show uniform spreading of the droplet on the bottom plate as the top plate is compressed. The glass coverslip was 40mm x 22mm in size.

To determine the accuracy of this method the shear cell was mounted on the confocal and fixed at a gap of 150µm. Reflection mode was used to determine the z position where the bottom plate came into focus, this position was recorded. The objective was raised until the top plate came into focus and the z position was recorded. The objective was lowered all the way and the top plate was moved forward 500µm using the motor. The z coordinates of the top and bottom focus positions were recorded at the new position. This procedure was repeated every 500µm for 5mm and again at 1cm.

Figure 21 is a plot of the z position of each plate at position tested along the shear

direction. Error bars are present but too small to be visualized. From these data we determined the plates were parallel to each other within 0.1 μm/1cm. This error was minimal and thus the droplet wetting method was used to align the plates before each experiment.

3.3.5 Determining the velocity profile

To characterize the shear cell and make sure the plate was moving steadily it was necessary to determine the velocity profile in the cell. Because of the non-Newtonian nature of the solution, it was also necessary to determine the velocity profile of concentrated suspensions. To collect data necessary to determine velocity at a given height, the cell was loaded and the gap was set at 150μm. The objective was positioned to image a chosen *xy* plane in the sample and the confocal was setup for a time series. Images were captured at a rate of 823ms as strain was applied. This procedure was repeated for each height tested with the most points collected near the plates. In between each experiment the sample was shear melted under oscillatory shear for 30 seconds at a rate of 1000um/s to its initial amorphous state.

3.3.6 Analysis of velocity data

Velocity at a given height in a sample was calculated by particle tracking. Two consecutive frames (n and n+1) in a time series were selected and the x and y coordinates of four particles chosen in the first frame were recorded. The same particles located in frame n were located again in frame n+1. Velocity for each individual particle was calculated using equation 1:

$$v = \frac{y_2 - y_1}{t_{\exp}} \quad (1)$$

where y_1 and y_2 were the particle's y coordinates in the nth and n+1 frame and t_{exp} was . the exposure time.

In each data set this procedure was repeated for two pairs of consecutive images. Velocities of all particles assessed were averaged to obtain the velocity in that plane and determine error. The error is thus the standard error of the mean of the x measurements.

3.3.7 Motor calibration

After aligning the plates, the cell was loaded with a solution of 2.5% PMMA in DOP and the gap was set at 150μm. The top plate was brought into focus and a time series was taken for 1 minute with the motor set to 10μm/s. This was repeated for several different velocities. Velocity data were analyzed using methods described above and then the velocity entered in the controller was plotted against the actual velocity calculated using particle tracking. By applying a linear fit to the data a calibration curve was generated (Figure 22).

3.3.8 Calculating theoretical velocity

To develop a theoretical velocity profile, the velocity of the top plate was calculated and substituted into equation 2.

$$\dot{\gamma} = \frac{v}{h} \quad (2)$$

Where h is the full film thickness of the sample (150μm) and shear rate is measured in

inverse seconds. In a plate-plate geometry, the shear rate found using the top plate should be constant throughout the sample. By setting the shear rate in equation 2, different heights can be substituted in equation 2 to generate a theoretical velocity profile.

3.3.9 Surface treatment

To address the possibility of wall slip, the plates were dip coated twice in a solution of 0.5% polydisperse PMMA particles in hexane and air dried. The dried plates were moved to a vacuum oven and cooked for 3 hours at 170˚C – significantly above the glass transition of PMMA (120˚C). The glass was cooled and the resulting surfaces and small amorphous patches of melted PMMA 0.33μm < h < 0.50μm measured by reflection mode on the confocal. Figure 21 shows images of the modified surfaces.

3.3.10 Application of step strain

For step strain experiments the cell was loaded and the gap was set at 150μm. The motor was connected to the controller interface and the desired velocity in μm/s was entered under "motion" in the "axis" menu. The velocity range for the motor in table 1 was 1μm/s to 10000μm/s, however, by visual inspection it was determined that the minimum speed that produced steady plate movement was 3μm/s.

The distance the plate needed to move to achieve a given strain was calculated by multiplying the number of strain units by the gap. This value was entered into the software. Once movement was initiated, the motor moved at the designated speed until the entered displacement was achieved. Progress of the suspension was monitored (i.e.

no lubrication flows, bubbles, disturbances) live by viewing an *xy* plane as shear was applied or recording an *xy* time series. Immediately after the flow stopped the sample was photopolymerized to halt particle motion.

Steady motor velocities between 3μm/s and 10000μm/s could be achieved so in the 150μm fixed-gap system shear rates between $0.02s^{-1}$ and $66.66s^{-1}$ were accessible. Because of the non-Newtonian nature of the suspensions the viscosity was shear rate dependent. This rheology for the 35% suspension we studied here is shown in Figure 23. Since an increase in shear rate resulted in rapid shear thinning, the accessible Peclet number range was restricted to $7.8 < Pe < 2620$. At high shear rates particle velocities exceeded the camera speed and dynamics could not be studied.

To analyze the structures formed, stacks of confocal images spaced z = ~0.081μm apart were acquired starting from the substrate up to z = 75μm. Each stack contained approximately 1000 images. After each sample was imaged, the objective was lowered and the shear cell was moved manually to image the film in another location. This was repeated to obtain a total of five samples per experiment.

3.3.11 One stroke vs. two stroke strain

To determine the effect of strain amplitude on crystal quality samples were sheared for strains of 1-160. Because the physical dimensions of the shear cell limited the single stroke strain amplitude to 67 for a gap of 150μm, to reach strains necessary for full crystallization of the sample (at strain = 160) it was necessary to determine whether a one stroke shear of a specific amplitude was equivalent to two strokes with half amplitude. To determine this experimentally a strain of 40 was applied to a sample

in a single stroke. An identical sample was sheared with two strokes of 20 strain units each The results for each sample were processed and crystalline fraction was plotted for each sample as a function of height in Figure 24. Since the shape and the height of the crystalline front height were very similar for the two samples we concluded this method could be used to accommodate strain requirements exceeding 1cm. For experiments, displacement was divided into a minimum number of equal length strokes.

3.4 Experimental results

The overall goal of the experiments that follow was to better understand strain requirements for colloidal crystal formation in dense colloidal systems. For suspensions undergoing simple shear flow, we attempted to connect microstructural changes in the samples to the macroscopic properties. The following sections show the effect of strain on the velocity profile and the overall crystal quality.

From the previous chapter we know that stress requirements in shear flow are well defined, however, strain criteria have not been extensively studied, Previous experiments show thousands of strain units[72] are required for dense samples to crystallize; however,

we found significant crystallization occurred with strains well below those reported by Ackerson et al. [67]. Figure 25 shows a structure formed under simple shear at a strain of 40. Figure 25b and Figure 25c are structural renderings of the sample before and after undergoing shear. From these data it is clear that at relatively low strains a significant amount of crystallization occurs. A more detailed analysis of strain dependence of crystal quality in samples undergoing simple shear is presented later in section 3.4.3.

3.4.1 Strain inhomogeneity in the velocity profile

Using direct visualization, Wu et al. (2009) indicated that in dense colloidal suspensions the velocity profile was inhomogeneous and the velocity profiles for partially crystalline samples were non-linear. They described three regions of flow: two near the plates and one in the center of the gap. Near the top and bottom plates the shear rate was significantly higher than in the middle region. On the macroscopic level, discontinuous shear thinning occurred when the microstructure changed from a discontinuous to a sliding layer structure[73].

Because of the possibility of non-linear behavior of a dense colloidal suspension under shear, it was necessary to characterize the flow in our shear device. We explored this by finding the velocity profile for both dilute and concentrated suspensions and then determined velocity as a function of strain.

3.4.1.1 Dilute velocity profile

The velocity profile for suspensions of 2.5% PMMA (d_p = 0.68μm) in DOP was determined using methods described in section 2.2.6. For shear rates of $0.083s^{-1}$, $0.166s^{-1}$, and 0.266^{-1} with corresponding Peclet numbers of 12.9, 17.4, and 23.3, a strain of 10 was applied and imaged at several different heights to construct a velocity profile. Experimental data were plotted with theoretical data generated using equation 2 in Figure 26. The velocity profiles were linear for each of the velocities tested as expected for Newtonian fluids. Linearity near the plates confirmed that slip was not occurring and that the device was functioning properly.

3.4.1.2 Concentrated velocity profile

After establishing the linearity of the dilute velocity profile, the velocity profile for 35% PMMA (d_p = 0.68μm) suspensions was determined for plate velocities for the same three velocities evaluated above. The velocity profiles along with theoretical data were plotted for each experimental velocity in Figure 27. Clearly, the velocity data do not match the theory lines as they did in Figure 26. Near both the top and bottom plates the velocity exhibited non-linear behavior and the deviation from linearity increased with increased velocity. Because the velocity in the dilute profile was linear near the plate slip was excluded as a possible explanation for these discrepancies.

3.4.2 Stain inhomogeneity

After establishing velocity profiles for both dilute and concentrated solutions at low strains we explored the possibility of strain dependence of the velocity profile in concentrated suspensions. A velocity of 40μm/s was selected for all tests because individual particles could be resolved at this speed at all heights assessed. Additionally, since disturbances in the velocity profile were more pronounced at higher velocities it made sense to use the velocity where the discrepancies were most prevalent. Methods outlined in section 3.3.6 were used to determine the velocity for different strains by performing particle tracking at the end of each time series. Velocity profiles were developed for strains of 10, 40 and 160. The crystalline boundary at the top and bottom each sample was determined by visual inspection for each value of strain.

Velocity profiles for each strain investigated were plotted with the theory line in Figure 28. For each strain, color-coded arrows correspond to the height of the crystalline boundary at both the top and bottom of the sample. At each strain, deviation of velocity profile from the theory line were correlated with the height of the crystalline boundary, indicating that the microstructure of the sample at a given strain may be correlated with the heterogeneity of the velocity profile Under the experimental conditions, a strain of 160 yielded in a fully crystalline sample.

3.4.3 Strain dependence of crystal quality

For each strain tested a sample was imaged in five separate locations and the crystalline fraction was averaged as a function of height. Average data for all strains were plotted together in Figure 29. Error bars represent the standard error of the mean. Each curve had a similar shape – several fully crystalline layers near the plates and then a sharp drop-off to negligible crystallinity. The number of layers increased with increasing strain until a strain of 160 where the sample was fully crystalline

The shape of the curves indicated that crystal growth could be modeled as a one dimensional process. The height of the crystalline front was determined from the strain data as the height in each sample where the crystalline fraction dropped below 0.5. The height of the crystalline front was plotted as a function of strain. This was shown in Figure 30. Crystalline boundary front movement as a function of strain.

The strains could be modeled as two linear regions (Figure 30). The first region was steeper and crystallization slowed down considerably in the second region.

3.4.4 Peclet number dependence

After determining the strain required for crystallization as a function of strain at a Peclet number of 23.3 we performed the same tests on for Peclet numbers of 8, 43 and 91. Peclet number was varied by changing the shear rate. We determined the crystalline boundary height at different strains. These data were plotted with the data for Pe = 23 in Figure 31.

Data for Pe = 8 and Pe = 45 followed the same trends as the Pe = 23 data. For Peclet number of 91, the sample shear melted and crystallinity was negligible for all strains investigated. Thus melting is located somewhere between $45 < Pe < 91$ for this suspension.

3.4.5 Gap dependence

To determine whether there is a specific distance where the boundaries are able to "see" each other to slow crystallization down we determined the crystallization front as a function of height. Figure 32 shows crystallization as a function of strain for several different gap.

For each gap we found that crystallization as a function of strain could be modeled with two lines of different slope with the first line being steeper. As the gap increased the amount of strain required for crystallization also increased.

3.5 Discussion

To date, several mechanisms for shear induced crystallization have been proposed including homogenous and heterogeneous nucleation [74] and classical

nucleation theory and tested through both experiment and simulation. In our experiments local nucleation was not observed as predicted by Brownian dynamics simulations[17, 69]. From Figure 29 and Figure 30, it was clear that shear induced colloidal crystallization could not be modeled as a nucleation and growth process. Because the time scale for flow-induced crystallization was much shorter than the scale of diffusion and quiescent crystallization the crystals that were formed due to the flow not some other process. The crystalline boundary built up layer by layer as opposed to forming clusters originating from defects in the sample so heterogeneous nucleation is also not applicable. This buildup is shown clearly in Figure 29.

Characterization of the dilute velocity profile (Figure 26) provided a control for study of dense colloidal suspensions. Since the velocity profile for the dilute suspension was linear at all velocities tested two conclusions were made: first, slip was not occurring at the boundaries and second, the device was functioning properly. This allowed us to confidently conclude that the non-uniformity of the velocity profile in Figure 26 was not a result of slip.

Because of the complex, non-Newtonian rheology of the dense colloidal system, it was not surprising that the velocity profile for the suspension was inhomogeneous. Some shear systems have shown shear thinning, thickening, and shear banding[75]. From Figure 28 it was evident that deviations from linearity near the plates increased with increasing velocity. To understand the inhomogeneity of the velocity profile we studied changes in the velocity profile as a function of strain. Looking at the arrows in Figure 28, the movement of the crystalline boundary was strongly correlated with non-linearity in the velocity profile.

From Figure 28 increased strain resulted in an increase in the height of the crystalline boundary. We hypothesized that deviations from linearity were due to microstructural changes in the sample. Crystalline layers were able to slide past each other much more easily than the bulk material. The work of Derks et al. (2009) confirmed that the velocity profile in simple shear was inhomogeneous and that the shape of the profile varied with shear rate [76]. They also noted that layers with different structures had viscosities. The viscosity for a sliding layer structure was 1.5 times lower than the bulk [76], which was consistent with our velocity results. This was further confirmed by data at strain = 160. Since a strain of 160 resulted in a fully crystalline sample it was not surprising that the entire velocity profile was shifted to the right of the simple shear theory.

Figure 29 showed that strain required for crystal formation in simple shear flow was much greater than the two strain units required for crystallization in spin coating. One possible reason for this discrepancy was the way strain was defined in the two systems. For spin coating, strain was defined macroscopically as the original film thickness divided by the final thickness. However, in plate-plate shear flow, strain was defined as the distance the top plane moved divided by the gap. Because of the differences in strain definitions we may not been comparing apples to apples.

Another possible reason for the different strain requirements could have been the nature of the flow itself. In simple shear flow, the shear rate was uniform throughout the sample. However, in spin coating, shear rate varied both spatially and temporally. Because so much unknown about the behavior of non-uniform shear, it may accelerate crystallization in ways we do not yet understand.

Even though the strain required for crystallization under simple shear was much larger than the strain required for spin coating, it was still important to note that crystals formed under shear flow at much lower strains than anticipated. Although it is not entirely clear why crystallization requirements in our experiments were so much lower than experiments previously reported, one possible explanation for this discrepancy was the limited amount of information that could be gathered using technology available at the time. Most analysis of early shear work was done using light, neutron, or small angle scattering [63]. Each of these techniques provided global steady-state structural measurements. However, using confocal microscopy, we were able to obtain local information about both steady state structure and dynamic growth of the crystalline boundary - information that was unavailable in previous studies. Another possible reason for the lower strain requirements may be that strain depends on the gap. Experiments presented in this chapter were performed with a fixed gap of 150μm, however, previous studies have used gaps on the order of 0.25mm-1.0mm [77]. Gap dependence of strain will be addressed later,

Another possible explanation for the low strain requirements was that historically most shear induced crystallization experiments were performed using hard sphere systems. In these systems, a volume fraction $\Phi > 0.494$ was required to access the crystalline regime, whereas in our system $\Phi = 0.35$ was in the crystalline regime. Since the volume fraction we used was so much lower than that of a hard sphere system, the particles had increased mobility and diffusion was much higher.

Looking at the plot of crystal quality as a function of strain all of the curves have a very similar shape – several layers of high quality crystals at the plate surface that

propagate upward then a sharp drop in crystallinity to zero. Because of the shape of the curves we were able to model crystal shear-induced crystallization as a one-dimensional crystallization. The idea of one-dimensional crystallization for field-assisted assembly was proposed by Russel et al. [78] in the context of sedimentation. The model assumes that growth rather than nucleation limits the order to disorder transition. Through x-ray scattering they were able to determine the samples built up layer by layer. Here we not that the volume fraction is homogeneous in our shear flow, as opposed to previous sedimentation work, but application of the one-dimensional crystal growth idea to shear flow could prove fruitful, as we now discuss.

To model the system as one-dimensional we found the height of the front for each value of strain. Examining the plot of the crystal boundary height as a function of strain we determined that there were two distinct regions of linear growth with the first significantly steeper than the second. We hypothesized that a possible reason for this was that at a gap of 150μm, when the solution is being sheared a crystalline boundary is growing symmetrically from both the bottom and the top of the gap. As strain increased, the number of crystalline layers increased resulting in a change in velocity profile. We propose that since change in the slope in the bulk moves slower than the crystalline layers that appear to be sliding past one another at some point the bottom and top crystalline boundary layer are able to "see" each other which is where the rate of crystallization decreases significantly and remains at the same place until a sample is fully crystalline. Additionally, if some layers were highly ordered than they may have a much easier time sliding past one another than would the amorphous bulk material which may have lots of clusters that have trouble pushing past one another

Crystal quality as a function of strain was tested for four different Peclet numbers. For Pe = 8 and Pe = 45 the crystalline boundary height trend followed the same trend as Pe = 23. For Pe = 91, crystallinity was negligible. This established an upper limit for the Peclet number criteria.

In order to determine whether the two regimes of crystallization speed were due to the crystalline boundaries interacting with each other we did a set of experiments where at a fixed Peclet number we preformed the strain experiments at gaps of 50, 100, 200, and 250μm. For each gap we found that crystallization as a function of strain could be modeled as two lines with the lower strain line being steep than the higher strain line. From Figure 32 it is evident that more strain is required for crystallization as gap increases. The slopes for the different gaps are similar, however there does not appear to be a fixed distance apart that the boundaries from the two sides can sense each other resulting in a decrease in crystallization rate.

3.6 Conclusions

From the experiments presented in this chapter it was evident that crystal quality in a sheared concentrated colloidal suspension was a function of the applied strain. Experimental data showed that crystals formed at much lower strains than previously reported in literature and that the crystalline boundaries propagated from the walls. Strain was found to be inhomogeneous in the samples studied, and the inhomogeneity was correlated with the movement of the crystalline boundary. Figure 30 showed that the growth of the crystalline boundary from the bottom surface could be modeled as a one-dimensional crystallization. The one dimensional crystallization rates applied for

other Peclet numbers below the melting point. Finally, crystallization rate was shown to be a function of the gap.

References

1. Krishnamurthy, L.N., N.J. Wagner, and J. Mewis, *Shear thickening in polymer stabilized colloidal dispersions.* Journal of Rheology, 2005. **49**(6): p. 1347-1360.
2. Shereda, L.T., R.G. Larson, and M.J. Solomon, *Local stress control of spatiotemporal ordering of colloidal crystals in complex flows.* Physical Review Letters, 2008. **101**(3).
3. Gasser, U., *Crystallization in three- and two-dimensional colloidal suspensions.* Journal of Physics-Condensed Matter, 2009. **21**(20): p. 24.
4. Ackerson, B.J., *Shear induced order in equilbrium colloidal liquids* in *Physica A*. 1991. p. 15-30.
5. Vermant, J. and M.J. Solomon, *Flow-induced structure in colloidal suspensions.* Journal of Physics-Condensed Matter, 2005. **17**(4): p. R187-R216.
6. Chen, L.B., B.J. Ackerson, and C.F. Zukoski, *Rheological consequences of microstructural transitions in colloidal crystals* Journal of Rheology, 1994. **38**(2): p. 193-216.
7. Wagner, N.J. and B.J. Ackerson, *Analysis of nonequilibrium structures of shearing colloidal suspensions.* Journal of Chemical Physics, 1992. **97**(2): p. 1473-1483.
8. Wu, Y.L., et al., *Melting and crystallization of colloidal hard-sphere suspensions under shear.* Proceedings of the National Academy of Sciences of the United States of America, 2009. **106**(26): p. 10564-10569.
9. Ackerson, B.J., *Shear induced order and shear processing of model hard-sphere suspensions*, in *Journal of Rheology*. 1990. p. 553-590.
10. Holmqvist, P., et al., *Crystallization kinetics of colloidal spheres under stationary shear flow.* Langmuir, 2005. **21**(24): p. 10976-10982.
11. Butler, S. and P. Harrowell, *Kinetics of crystallization in a shearing colloidal suspension*, in *Physical Review E*. 1995. p. 6424-6430.
12. Ackerson, B.J. and N.A. Clark, *Sheared colloidal suspensions*, in *Physica a-Statistical Mechanics and Its Applications*. 1983. p. 221-249.
13. Ackerson, B.J. and T.A. Morris, *Shear induced order of concentrated suspensions*, in *Better Ceramics through Chemistry Iv*. 1990. p. 159-166.
14. Ackerson, B.J., *Shear induced order in equilbrium colloidal liquids* in *Physica A*. 1991. p. 15-30.
15. Derks, D., et al., *Dynamics of colloidal crystals in shear flow.* Soft Matter, 2009. **5**(5): p. 1060-1065.
16. Gasser, U., *Crystallization in three- and two-dimensional colloidal suspensions*, in *Journal of Physics-Condensed Matter*. 2009. p. 24.
17. Blaak, R., et al., *Crystal nucleation of colloidal suspensions under shear*, in *Physical Review Letters*. 2004.
18. Cohen, I., et al., *Slip, yield, and bands in colloidal crystals under oscillatory shear.* Phys Rev Lett, 2006. **97**(21): p. 215502.
19. Derks, D., et al., *Dynamics of colloidal crystals in shear flow*, in *Soft Matter*. 2009. p. 1060-1065.

20. Ackerson, B.J. and P.N. Pusey, *Shear-induced order in suspensions of hard-spheres* Physical Review Letters, 1988. **61**(8): p. 1033-1036.
21. Davis, K.E., W.B. Russel, and W.J. Glantschnig, *Settling suspensions of colloidal silica - observations and x-ray measurements.* Journal of the Chemical Society-Faraday Transactions, 1991. **87**(3): p. 411-424.

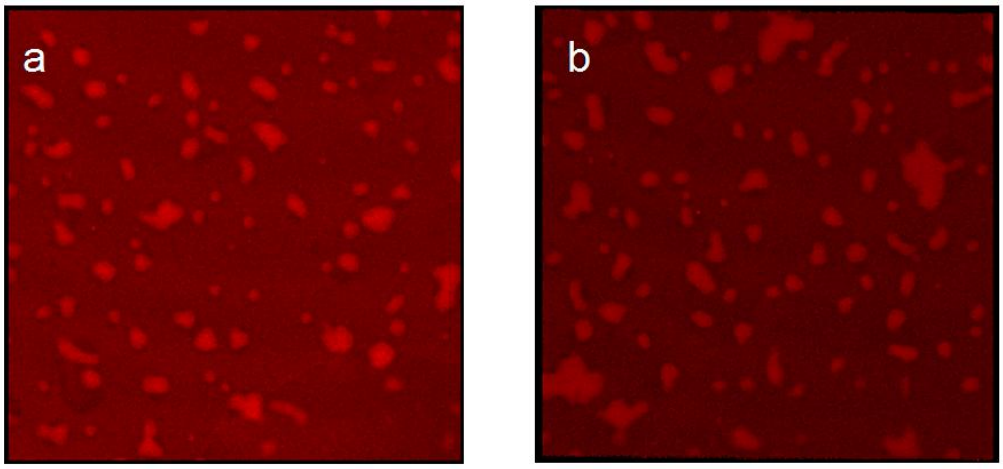

Figure 21: images of PMMA treated surfaces (a) bottom (b) top

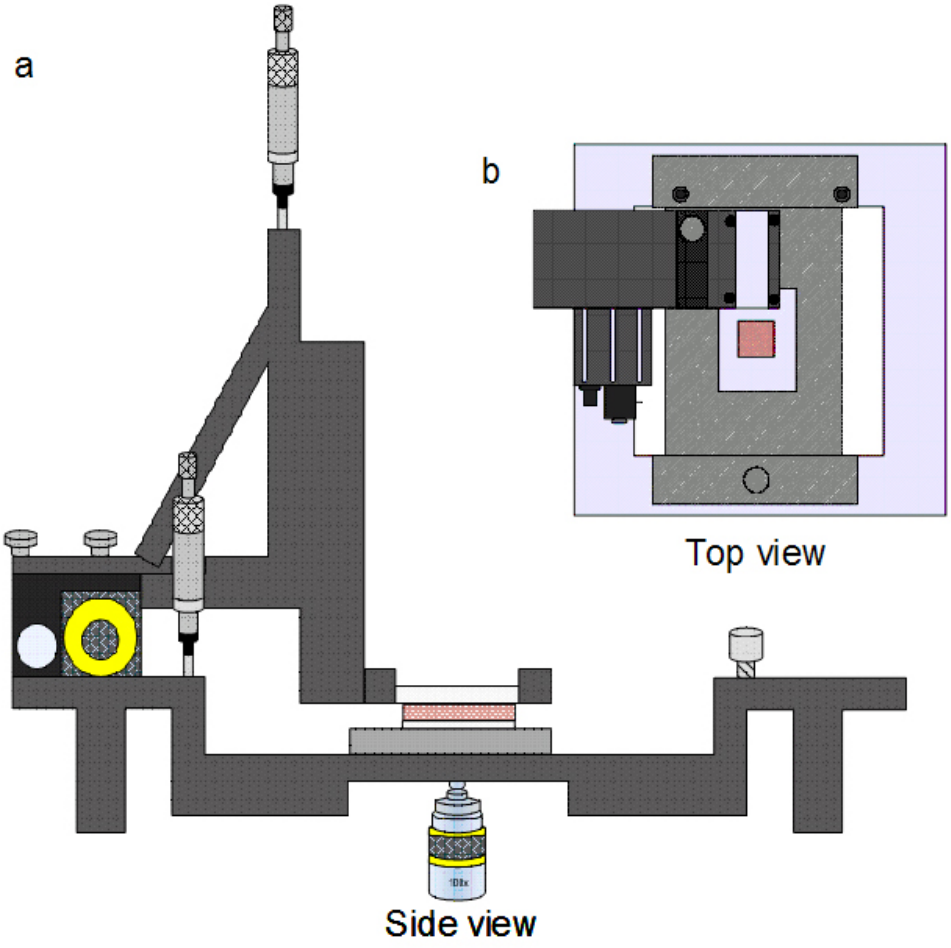

Figure 22 schematic of shear cell (a) side view and (b) top view

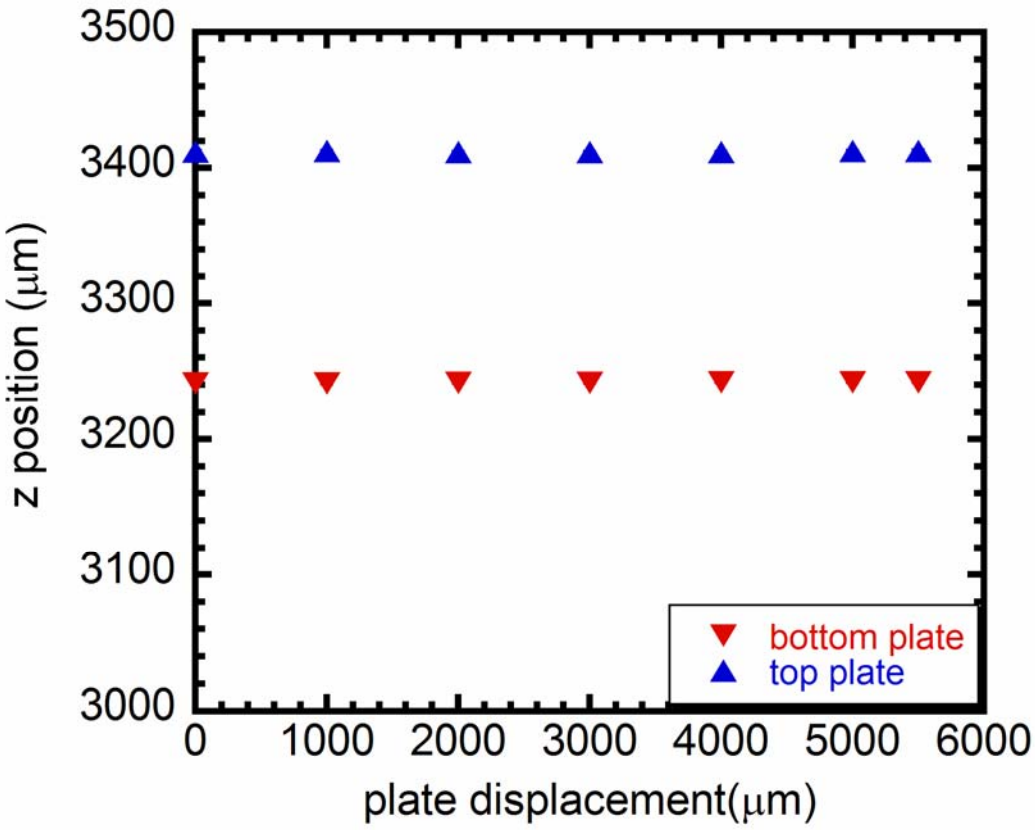

Figure 21. Parallel plate allignment in the shear direction. Plates were parallel within +/- 0.2μm per millimeter. Performed at a gap of 150μm.

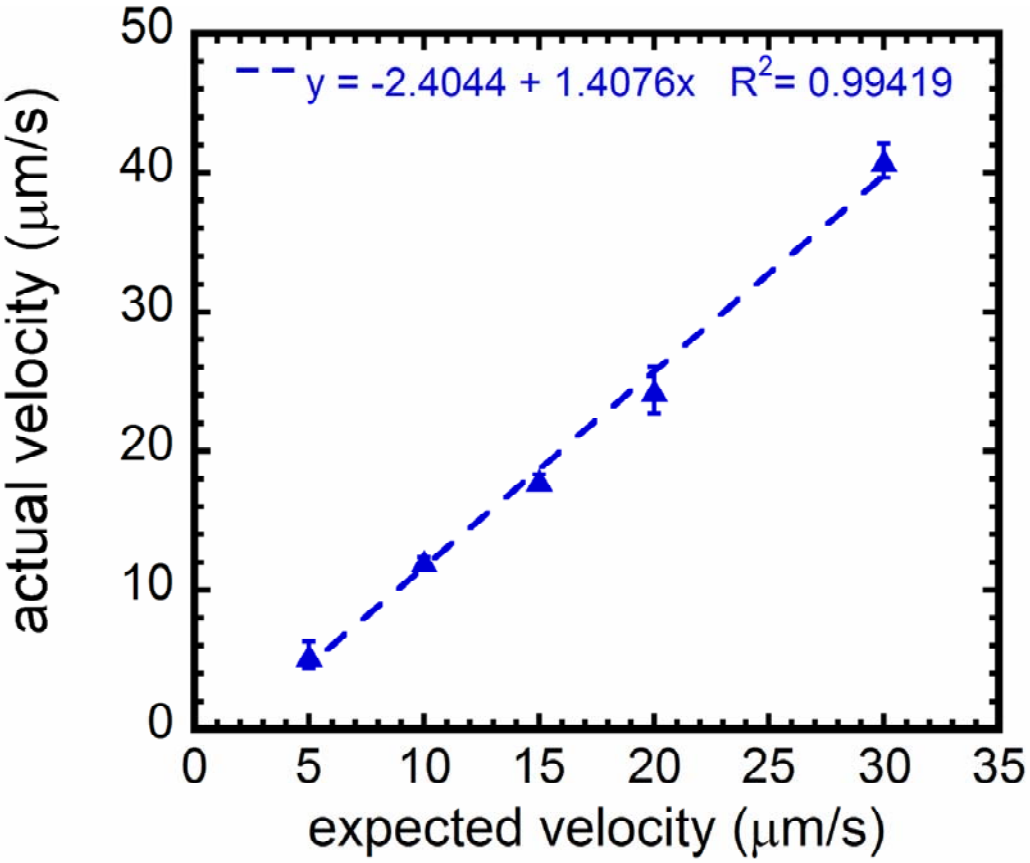

Figure 22. Calibration of plate velocity generated by the stepper motor.

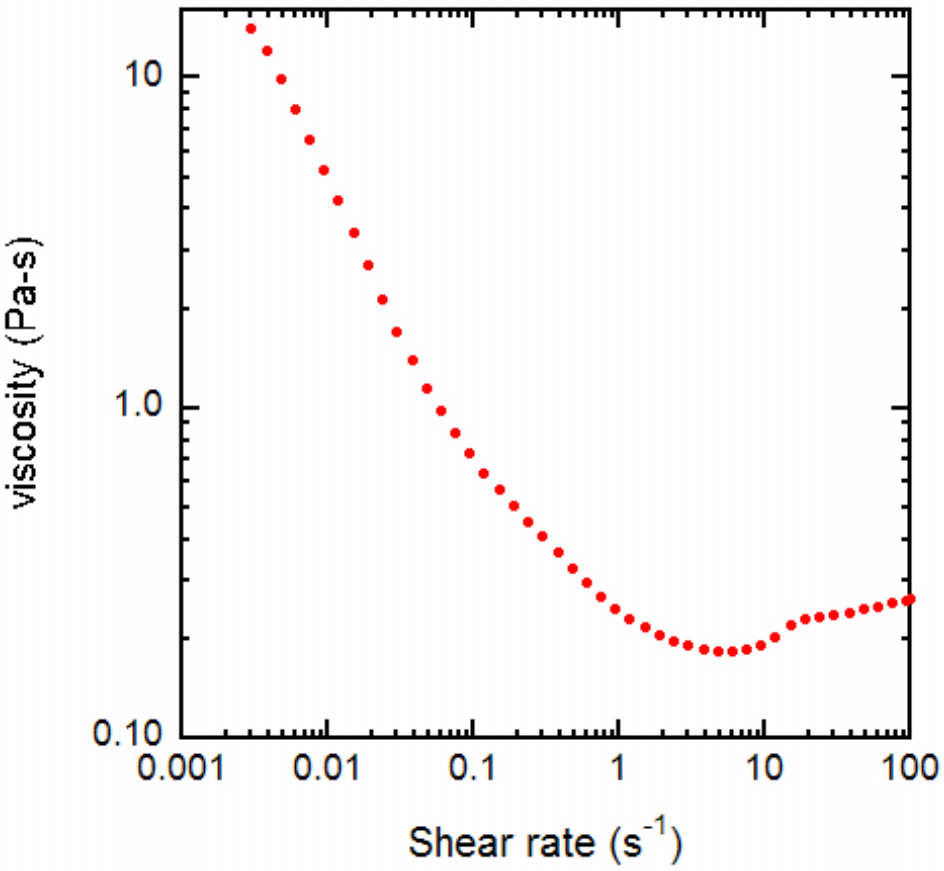

Figure 23. Viscosity as a function of shear rate in 35% PMMA , 7% photopolymer and 1% initiator in D OP. A 6cm cone geometry was used

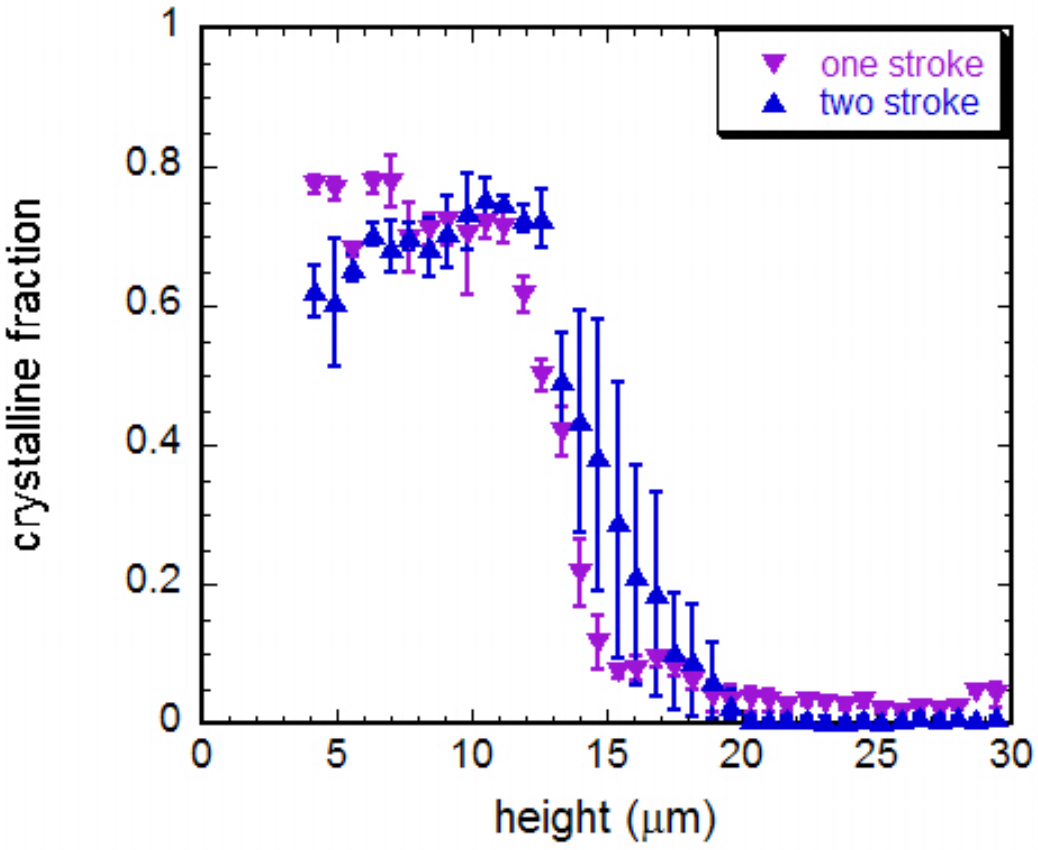

Figure 24. Comparison of structures formed by simple and oscillatory shear at identical strain. Forty strain units were applied.

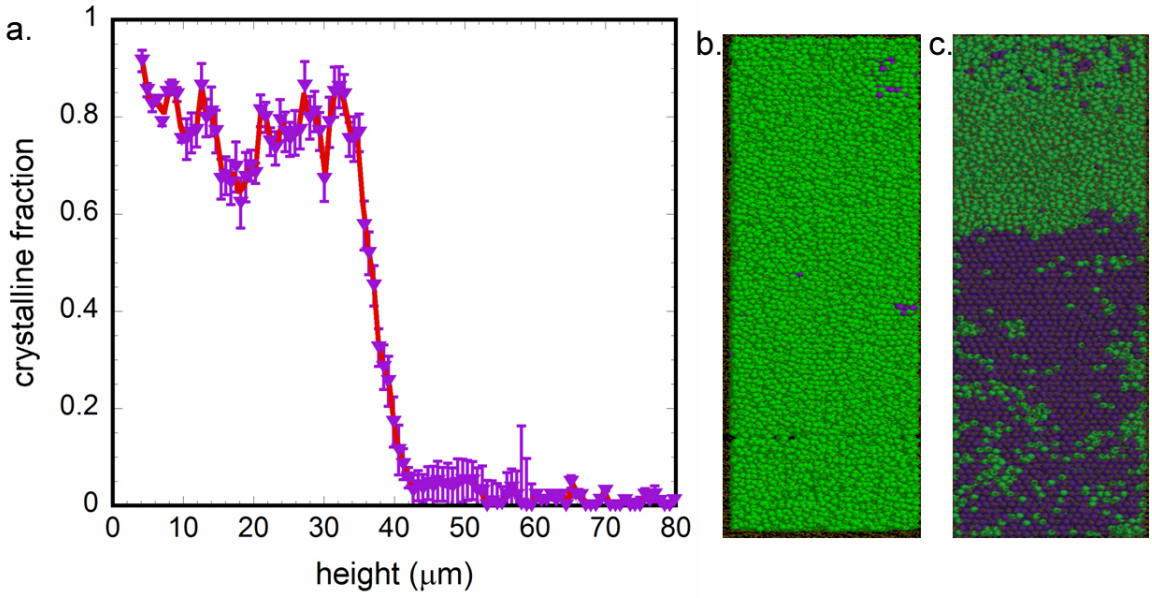

Figure 25. For an applied strain of 40 (a) crystal quality plotted as a function of height in the sample (b) rendering of the sample structure before shearing (c) rendering of structure after shearing. Green particles are amorphous and purple particles are crystalline according to the q6 algorithm. Error bars are standard error of the mean.

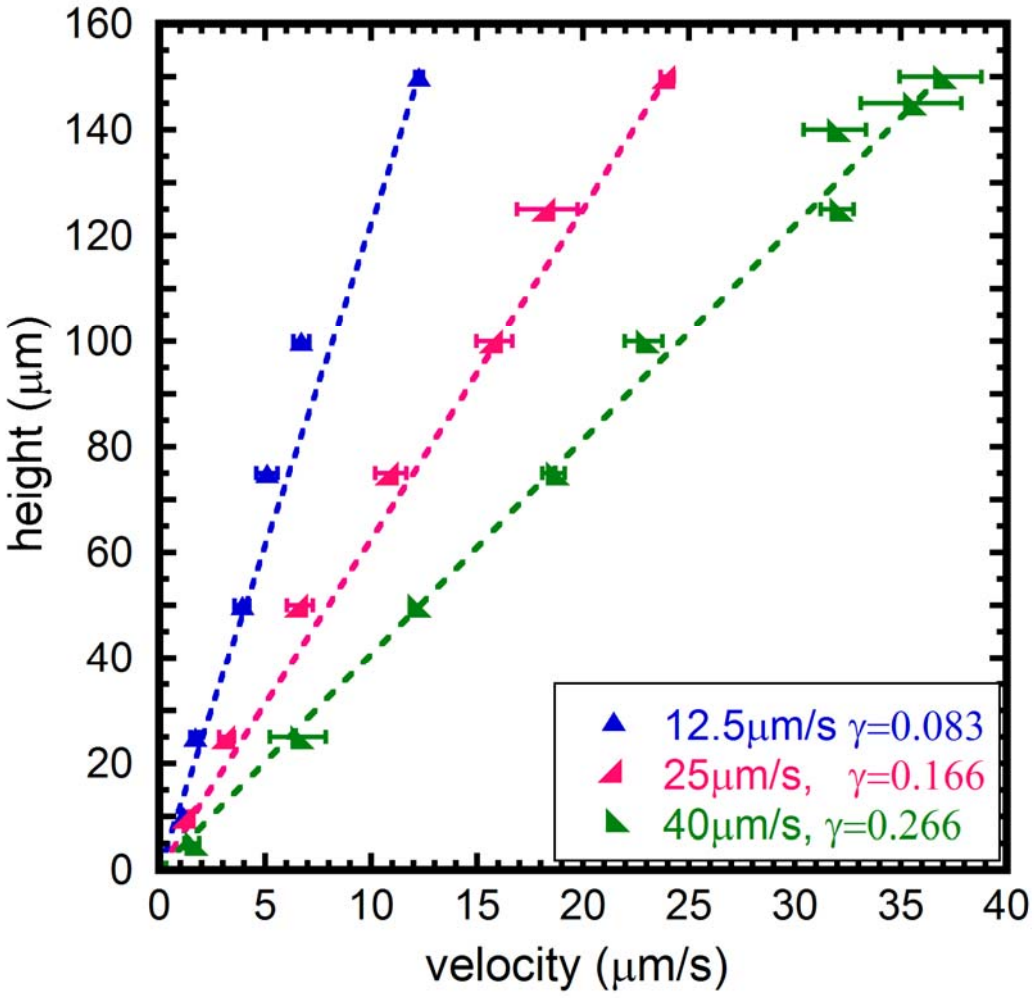

Figure 26. Velocity profile for 2.5% PMMA in DOP. Height = 0mm corresponds to the substrate and height = 150mm corresponds to the top plate

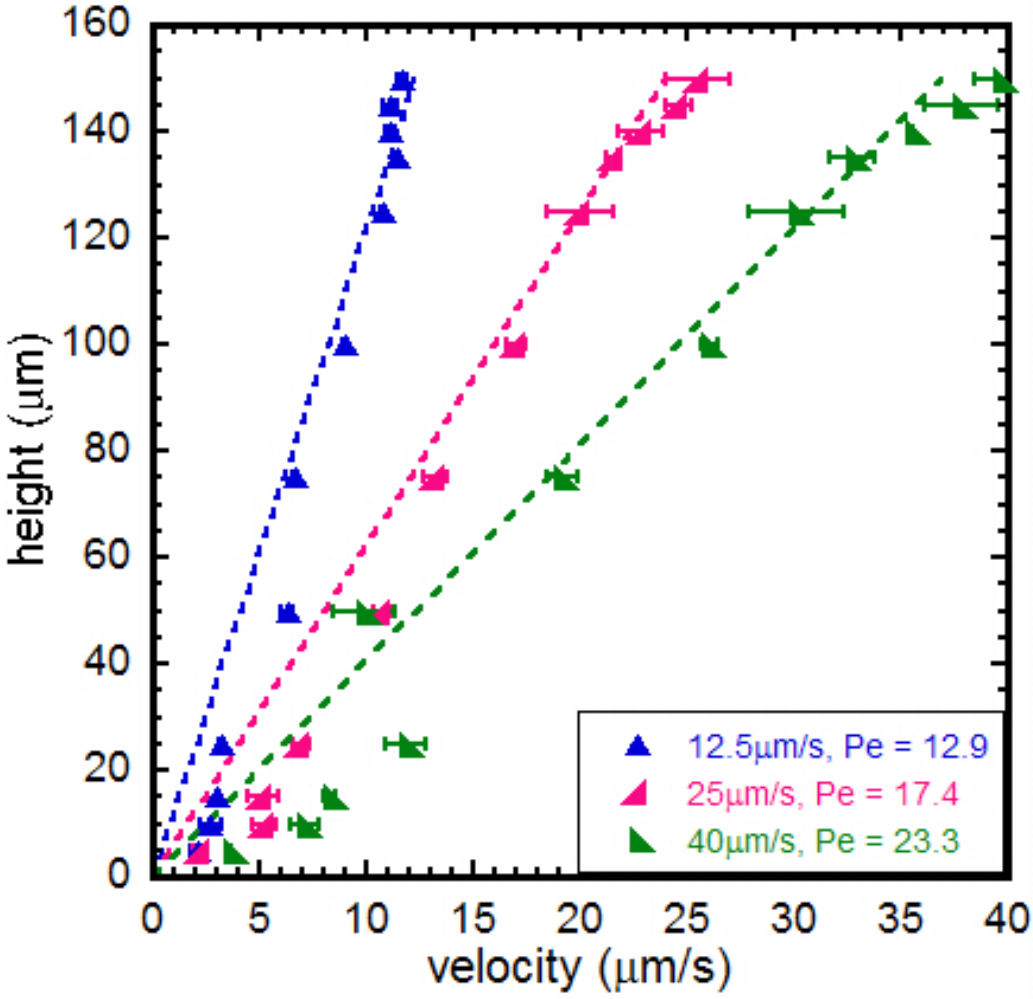

Figure 27. Velocity profile for a 35% PMMA suspensions. Height = 0 refers to bottom plate, height = 150 refers to the top plate.

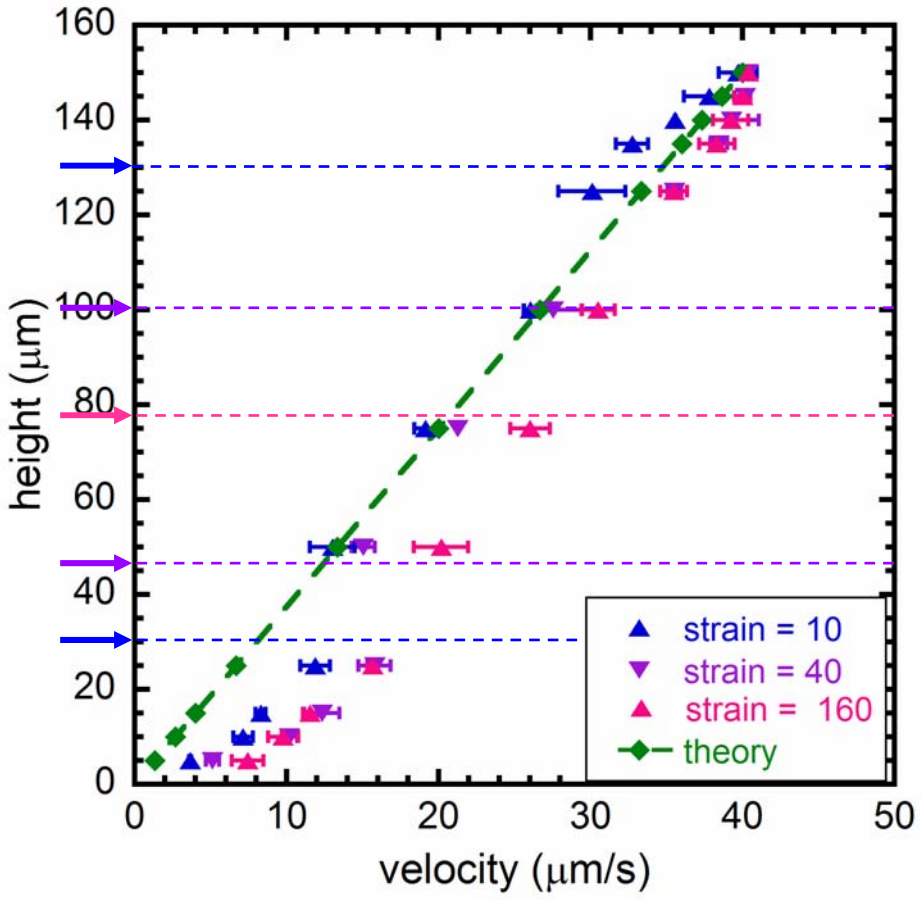

Figure 28. Strain dependence of velocity. Color coded arrows correspond to the height of the crystalline boundary at the strains used in these experiments. For all experiments gap = 150μm, shear rate = 0.266s^{-1} and Peclet = 23.3.

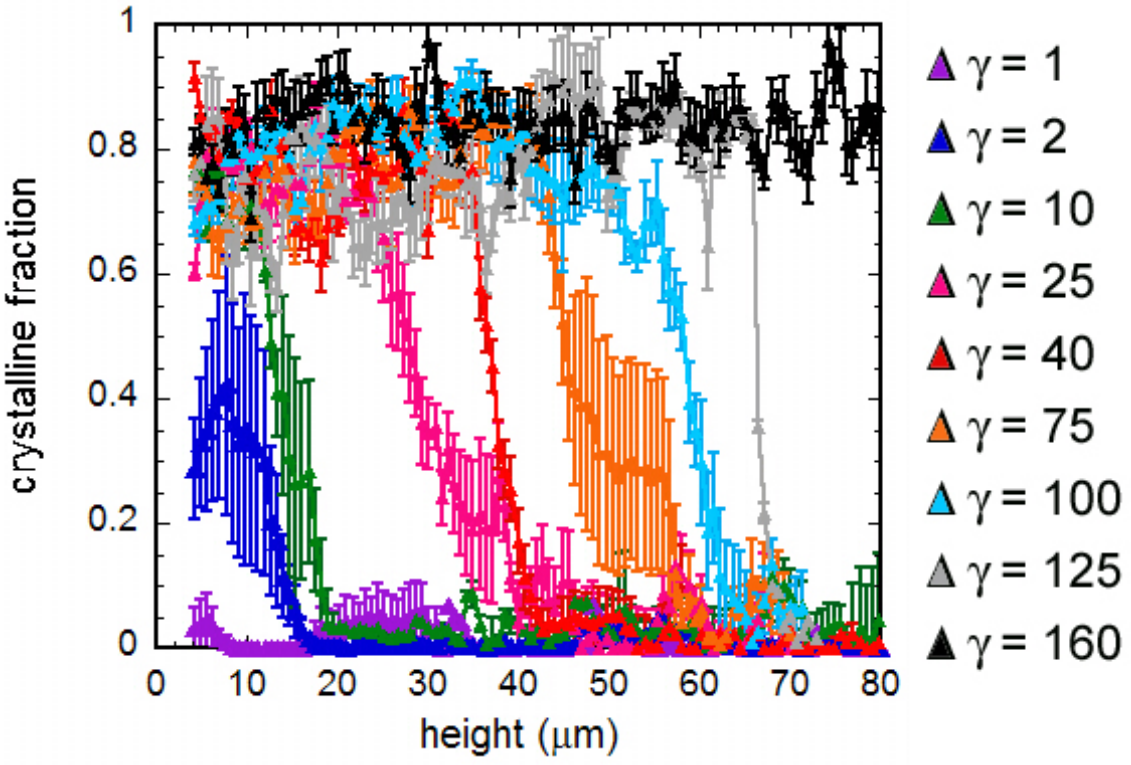

Figure 29. Variation of crystal quality as a function of strain. All experiments were performed at a gap of 150μm and Pe = 23.3. Each curve is the average of five samples and error bars are the standard error of the mean.

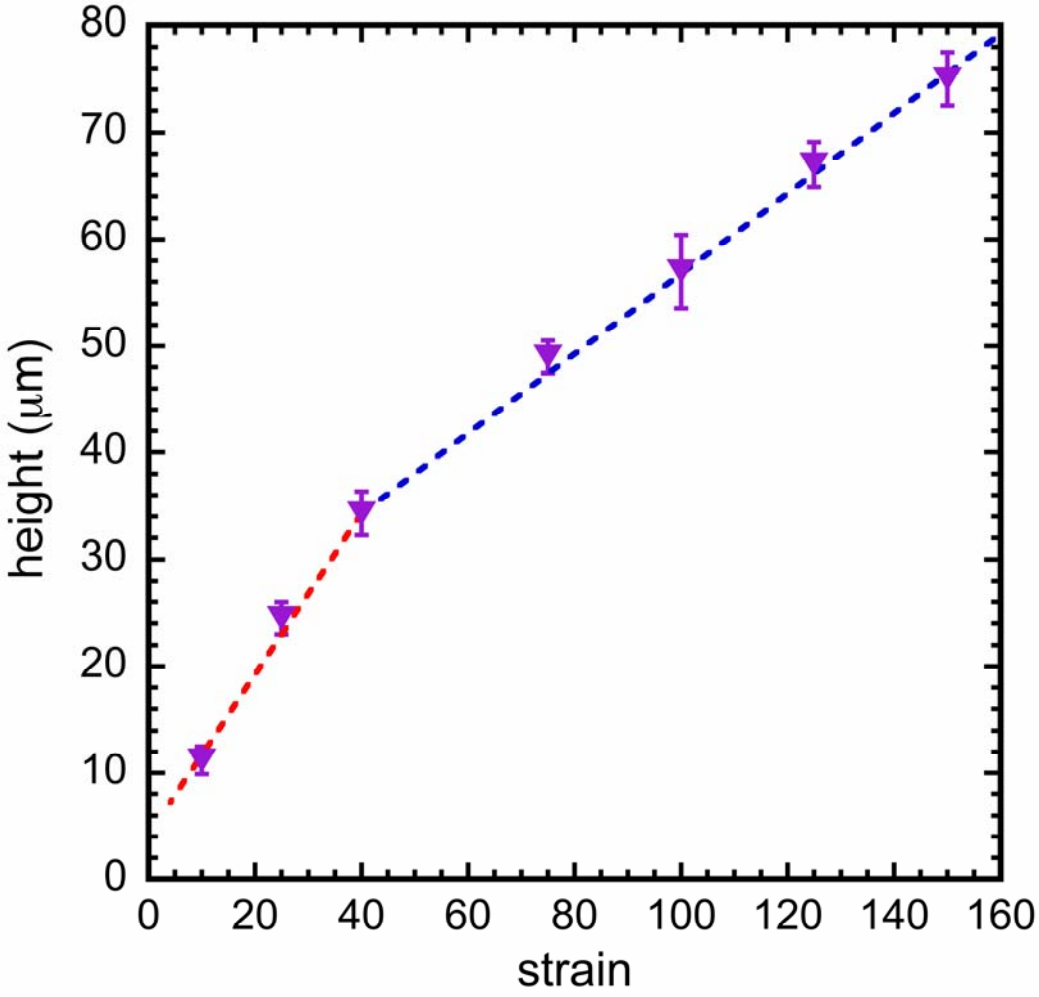

Figure 30. Crystalline boundary front movement as a function of strain. For all experiments gap = 150μm and Pe = 23.3/. Each data point is the average of five measurements. Error bars are standard error of the mean.

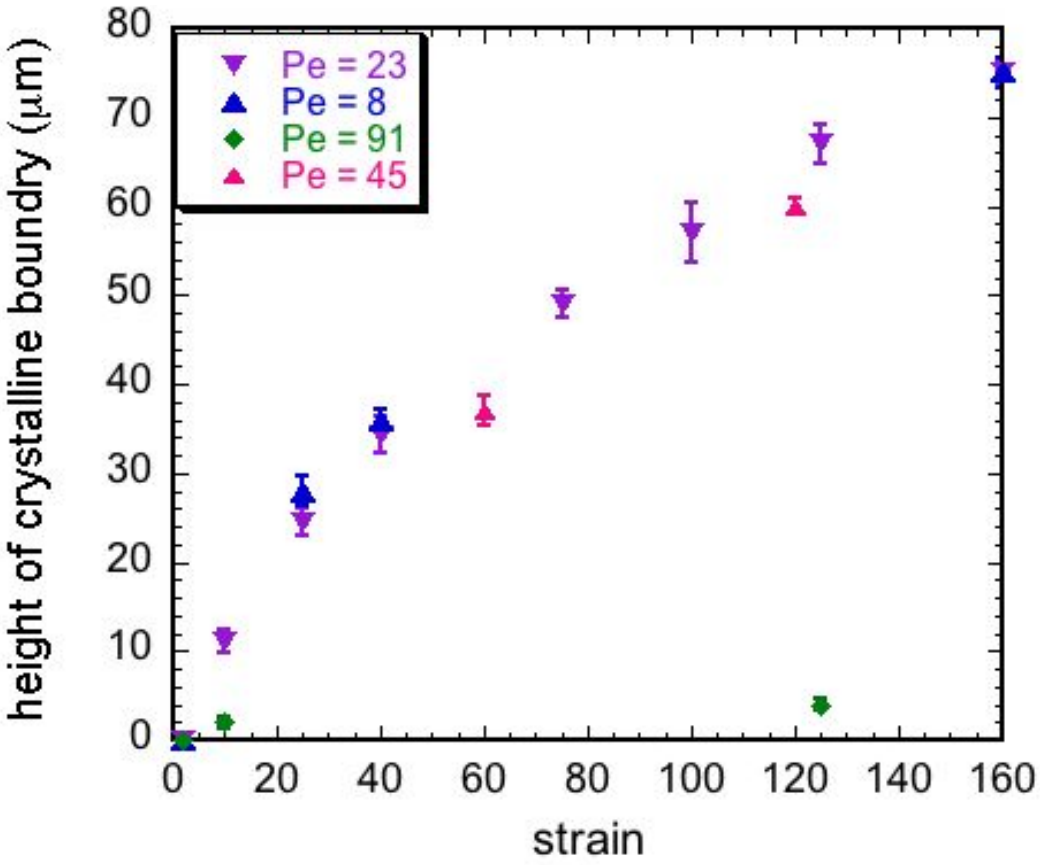

Figure 31. Strain dependence of crystal quality for varying Peclet numbers. Peclet number was varied by changing spin speed. Each data point is the average height of the crystalline boundary over five samples. Error bars are the standard error of the mean.

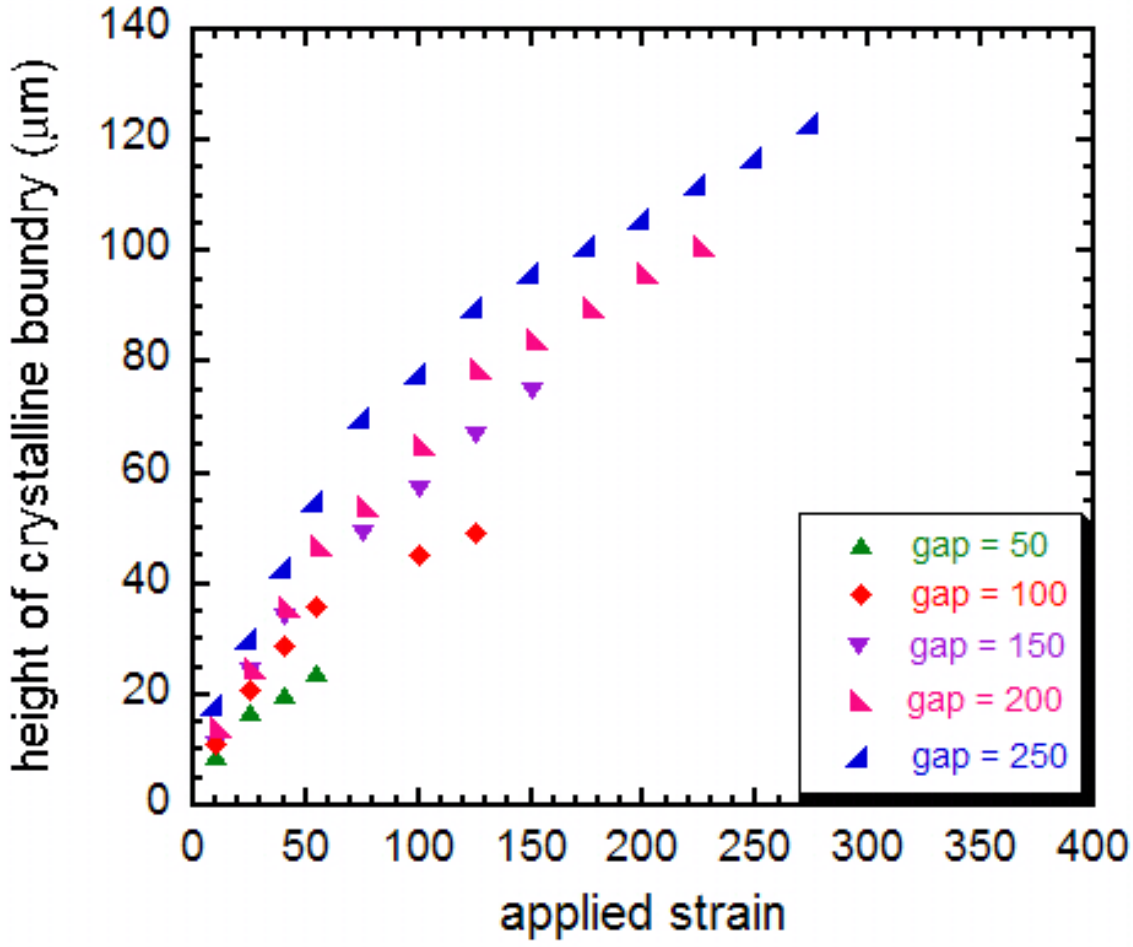

Figure 32. Gap dependence of crystal quality. All samples were studied at a Peclet number of 23.3.

CHAPTER 4

Strain accelerated formation of colloidal crystals

4.1 Chapter summary

The purpose of this chapter is to show how the rate of crystallization in a sheared colloidal suspension can be significantly accelerated by application of a step strain significantly smaller than the strain required for full crystallization. Step strain deformation was applied to the model colloidal suspensions used in chapter three. After cessation of flow, samples were allowed to continue to crystallize under quiescent conditions and the height of the crystalline boundary was recorded as a function of time. This chapter shows that application of step strain deformation less than the strain required for full crystallization results in significant acceleration of crystal growth relative to the case where no flow is applied.

4.2 Materials and methods

The suspensions used for the experiments in this chapter were the same as those used for experiments in chapter 3. The methods used for step strain deformation in the experiments that follow were described in chapter 3. Briefly, particles were sterically stabilized poly(methyl methacrylate) spheres ($d_p = 0.68\mu m$) suspended in dioctyl

phthalate with a small amount of photopolymer and initiator. Step strain shear was performed in a parallel plate shear cell.

Experiments were performed with strains of 10 and 40. All experiments had a gap of 150μm and a Peclet number of 23.3 for step strain and solution compositions are the same as those in chapter 3 (ϕ = 0.35). Strain varied from 1 – 300 for these experiments. Samples were loaded in the shear cell and a step strain deformation was applied. Upon cessation of shear, instead of quenching crystallization as in chapter 3, samples were not photopolymerized and were instead allowed to continue to crystallize until full crystallization was achieved. The height of the crystalline boundary was determined by visual inspection of confocal images and recorded as a function of time until samples were fully crystalline. Figure 35 shows a time series of images as well as the visual determination of the crystallization boundary for the case of γ = 40.

4.3 Experimental results

Crystallization occurred as in chapter 3, growing from a boundary with a consistent layer thickness. In the experiments that follow, the rate of crystal growth was determined by visually tracking the height of the crystalline boundary from confocal images after application of a step strain deformation. We estimate the error in layer height determination is based on 3 replications of the 40 μm strain case.

To determine the effect of step strain on crystallization rate we plotted the movement of the crystalline boundary for the quiescent data gathered in chapter 3 along with the crystalline boundary height movement data after the application of strains of 10 and 40. For each data point, Δh was defined as the current height of the crystalline

boundary minus the height of the crystalline boundary at the time of cessation of shear. These data are shown in figure 35.

From figure 35 was clear that application of step strain resulted in two orders of magnitude decrease in time required for crystallization. For example, for no strain to crystallize 40μm, ~24 hours was required. If a strain of 10 is applied the required time is 1800 seconds. Additionally, the crystal growth rates for both strain = 10 and strain = 40 were very similar.

After comparing the strain accelerated data to the no strain quiescent case it was also necessary to compare the rate of crystallization in partially strained systems to determine if the rate of crystal formation was significantly different from fully sheared systems. These data are shown in Figure 36.

From figure 36 it is evident that crystals do not form as quickly when a partial strain is applied as when strain is applied until the sample is fully crystalline. For example, if strain is applied continuously, the crystalline boundary reaches a height of 40μm in 325 seconds. However, when a strain of 10 is applied and the sample is allowed to continue to quiescently crystallize, 1800 seconds are required for the crystalline boundary to reach 40μm in height.

4.4 Discussion

From the data presented in this chapter it was clear that step strain deformation of amplitude significantly lower than that required for full crystallization can be used to accelerate crystal formation. Figure 35 showed that applying a small amount of step strain significantly increased the rate of crystallization from the rate of quiescent crystal

growth. A two order of magnitude increase in crystal formation was seen for the strain accelerated system. However, figure 36 showed that even though crystals formed much faster when partial strain was applied, the case where shear was continually applied until the sample was fully crystalline was the most efficient method for crystal formation.

It is interesting that an application of the two different partial strains (10 and 40) resulted in different heights immediately after cessation of shear, however the curves in figure 35 showed nearly identical slopes or rates of crystal growth. There a several possible reasons for the constant growth rates. We hypothesize that the growth rate is due to a form of templating. Application of a step strain results in formation of crystalline layers on the wall surfaces. After the step strain deformation, these layers act as a template and the particles fill in the interstitial spaces of the layer below and form new layers. The structure of the top layer of for both strains of 10 and 40 formed the same hexagonal non-close packed structure with only a difference in crystalline boundary height. Therefore, the layers would grow at the same rate since the only difference is the initial starting height. Since in figure 35 the two strain curves are normalized by subtracting out the initial sample height, it makes sense that the crystal growth rates would be nearly identical.

The templating hypothesis indicates the amount of strain applied was less important than the fact that some amount of strain was applied, forming the template for crystallization.

4.5 Conclusions

Application of a step strain deformation less than that required to fully crystallize a sample results in an increase in crystal formation speed of two orders of magnitude from quiescent crystallization. We hypothesize this is because the initial step strain deformation results in the formation of crystalline layers that act as a template for further crystallization. Though crystallization after application of step strain is significantly faster than quiescent crystallization, it is still slower than shearing until the full sample is crystallized.

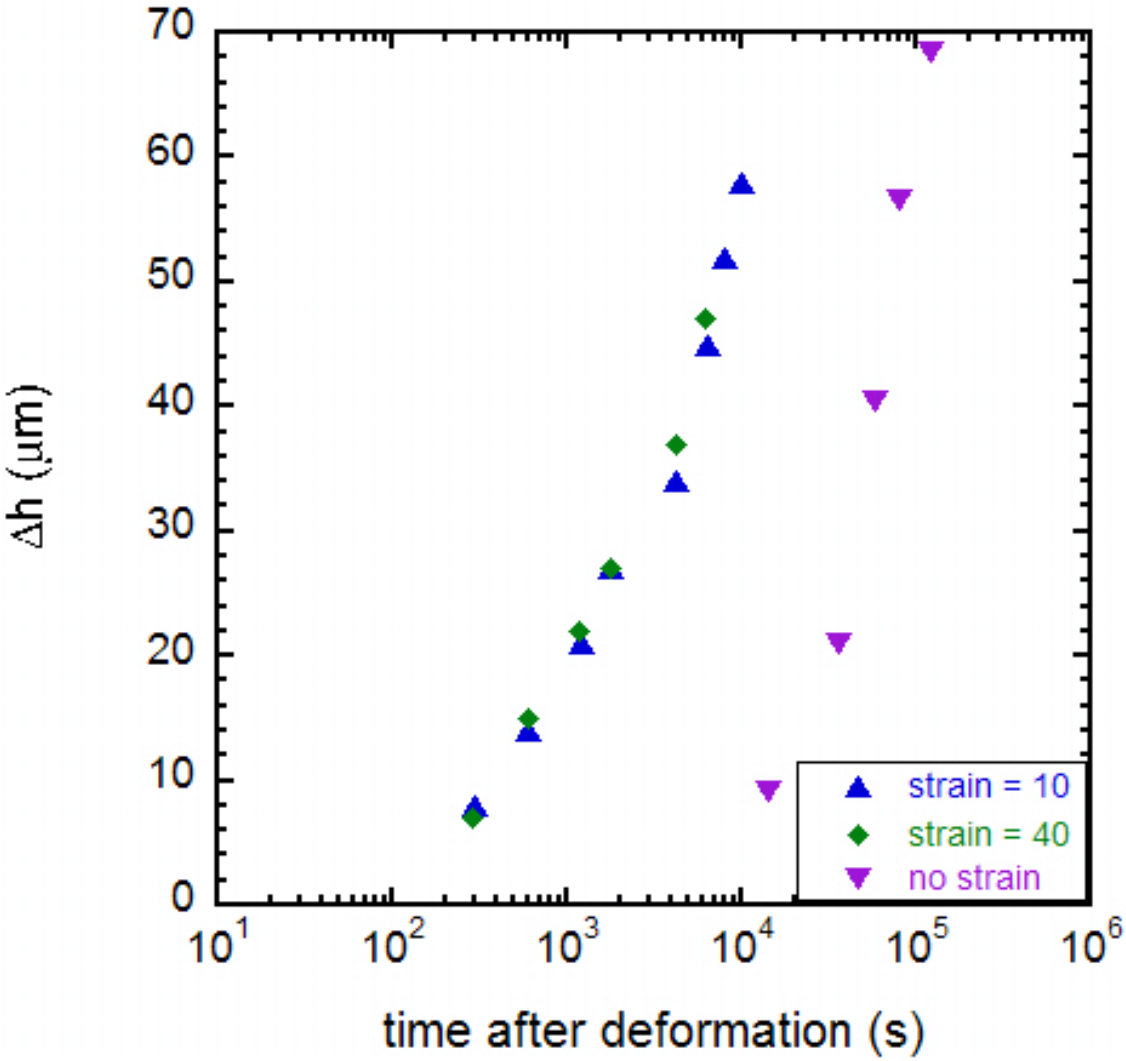

Figure 35: Crystallization as a function of time after deformation. Quiescent data was to compare time required for crystal formation. The y axis represents the difference in the height of the crystalline boundary at the given time, minus the height of the crystalline boundary immediately upon the cessation of shear.

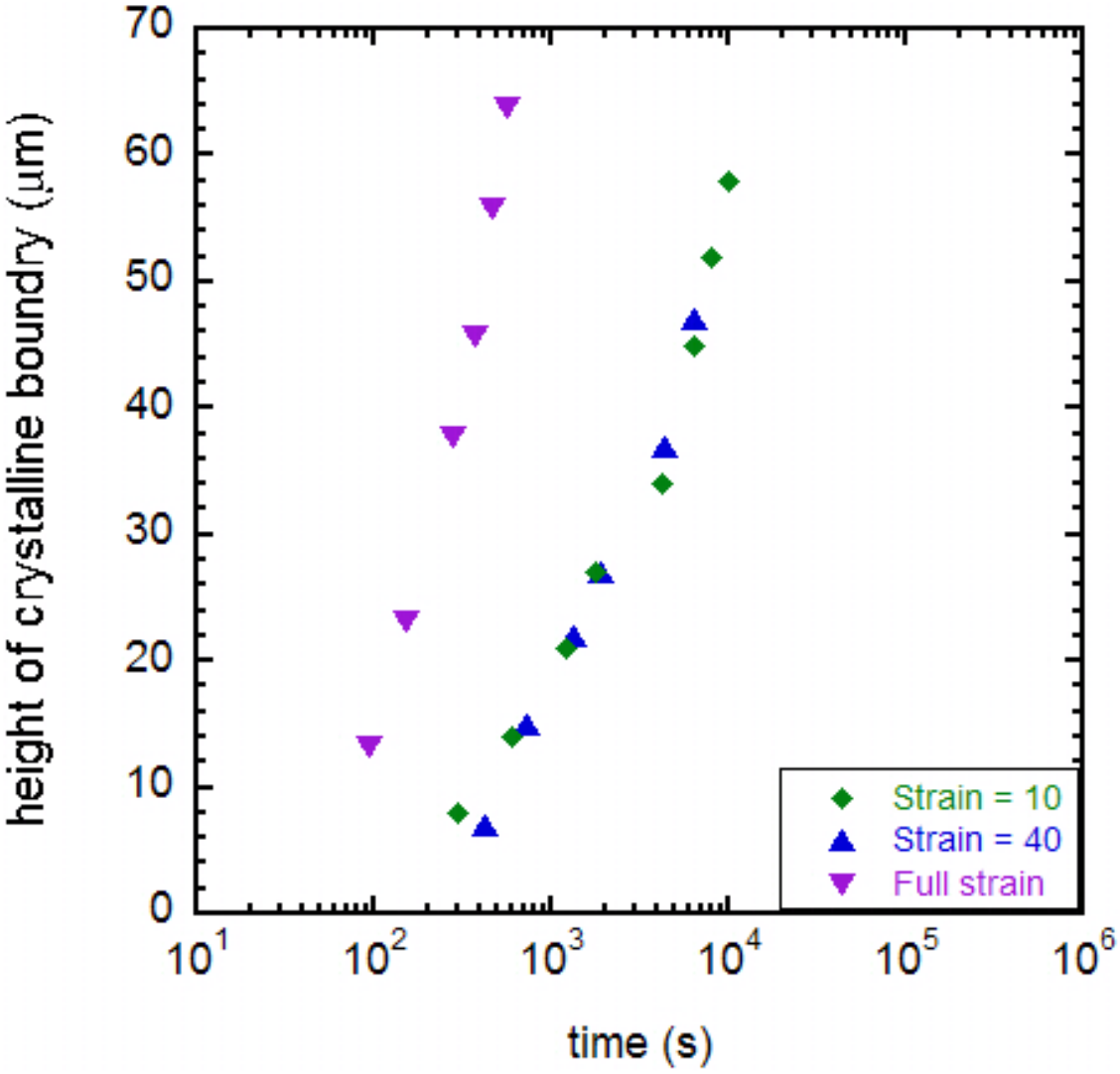

Figure 36: Movement of the crystalline boundary in fully sheared samples and strain accelerated samples. Points in the "full strain" samples were sheared for the time indicated and not allowed to crystallize quiescently.

Chapter 5
Evaluation of the spin coating Peclet number theory over a range of volume fractions

5.1 Chapter summary

The purpose of this chapter was to determine the conditions under which the spin coating Peclet number theory presented in chapter 2 could be applied. The theory predicted the kinetics of an order to disorder transition at Peclet number of unity for steady state samples. Samples with volume fractions in the glass transition, coexistence region, and crystalline regime were tested. Samples were spin coated, imaged by confocal microscopy, and processed using the techniques described in chapter 2. The results of this chapter indicate that the Peclet number theory could only be applied to samples with volume fractions in the crystalline regime. In this system the volume fraction was between $\Phi = 0.215$ and $\Phi = 0.50$ Discrepancies between experiments in chapter 2 and experiments presented in this chapter were also explored.

5.2 Materials and Methods

To further assess the applicability of the Peclet number theory presented in chapter 2, it was necessary to determine its validity at other volume fractions. The methods used for the experiments in this chapter were described in detail in section 2.2.

Each sample was spin coated for three minutes at a rate of 600rpm, photopolymerized, and imaged using confocal microscopy. Images were processed and crystal quality as a function of z position was determined for each sample. For every volume fraction tested, samples were imaged at three radial positions: 5μm, 75μm, and 1000μm from the axis of rotation. At each volume fraction five independent experiments were conducted to determine reproducibility and statistical error.

For the experiments in this chapter particles were 0.68μm in diameter with a polydispersity of 2.3%. Coexistence was determined for the batch of particles used in this chapter via the quiescent crystallization methods detailed in section 2.3.7.7. The coexistence region spanned from $\Phi = 0.175$ to $\Phi = 0.215$. The amount of salt required for the experiments in this chapter was 10μM. This was slightly less than the 13μM salt concentration used in chapter 2.

5.3 Experimental results

The overall aim of the experiments in this chapter was to determine the concentration range where the Peclet number theory could be applied. Steady state spin coated samples for volume fractions in the coexistence, crystalline, and glassy regimes were studied. Volume fractions of $\Phi = 0.25$, 0.35, 0.40, and 0.45 were studied to establish the validity of the Peclet number theory in the crystalline regime.

5.3.1. Validity of Peclet number theory in the crystalline regime

For each volume fraction, crystal quality was determined as a function of z position in the sample at each radial position tested. Peclet numbers were calculated for each data set and crystal quality versus Peclet number was plotted in figure 1.

Figure 1 showed a steep transition from negligible crystallinity to full crystallinity at a Peclet number of approximately 0.8. In the previous Peclet number study (chapter 2), the order to disorder transition occurred at a Peclet number of ~2. To determine whether there was a significant difference between the two data sets, data from figure 1 were plotted along with the data from the previous study.

Figure 2 showed that in both data sets, a steep transition occurred in all volume fractions tested, however, figure 2 confirmed that the order to disorder transition occurred at a slightly lower Peclet number than data from chapter 2.

5.3.2. Validity of Peclet number theory in the coexistence regime

Following the same experimental protocol, the Peclet number theory was tested for $\Phi = 0.19$, a volume fraction in the coexistence region, at radial positions 75μm and 1000μm from the axis of rotation. Peclet number was calculated and results are shown in figure 3.

For $\Phi = 0.19$, despite the strength of the applied force, the particles maintained a liquid structure with a few partially crystalline layers at Peclet numbers that according to the theory should be crystalline. From figure 3 it was clear that the Peclet number theory did not apply for volume fractions below the crystalline regime.

5.3.3 Validity of Peclet number theory above the glass transition

According to quiescent studies used to determine phase boundaries, the glass transition occurred at $\Phi > 0.45$. The Peclet number theory was tested for $\Phi = 0.50$, a volume fraction above the glass transition. After spin coating for three minutes at 600rpm, samples were imaged 75μm and 1000μm from the axis of rotation. The structures formed were dense and amorphous and the particles appeared to be jammed. A plot of crystal quality as a function of Peclet number shown below confirms that the Peclet number theory can not be applied to samples with volume fractions above the glass transition.

5.4 Discussion

Because crystallization rate depends strongly on concentration[[79]] it was necessary to explore the robustness of the Peclet number theory by exploring the effect of volume fraction on crystal quality in spin coated samples. From the data in figures 3 and 4, it was established that the Peclet number theory was not valid for samples with volume fractions outside the crystalline regime. For this batch of particles the theory only applied when $0.25 < \Phi < 0.50$.

For volume fractions in the crystalline regime, figure 1 showed a sharp disorder to order transition indicating that the Peclet number theory applied. Figure 2 was generated to compare the data from the spin coating study in chapter 2 to experiments in the current chapter. From figure 2 it was apparent that the two data sets were very similar in shape, however, the order to disorder transition occurred at a slightly higher Peclet number in the old data set. To determine the reason for the difference between the two data sets, we examined the spin coating Peclet number equation.

$$Pe = \frac{6\pi\rho\omega^2 r(h-z)a^3}{k_B T} \tag{1}$$

From equation 1 it was apparent that the spin coating Peclet number depended on three variables: spin speed (ω), particle size (a), and position in the sample (r, z). We assessed the effect of each of these variables individually and determined the magnitude in error required to cause the shift in figure 2.

To make the shift easier to visualize, each of the curves was fit using a inverse tangent function in the form of equation 2:

$$y = A*[\tan^{-1}\{B*(x-C)\} + E] \tag{2}$$

The fitted data sets from both chapter 5 and chapter 2 are shown in figure 5 and figure 6 respectively. Equation 2 describes an empirical fit. The parameters A,B, C, and E were varied until upon visual inspection a curve with the slope fitting the center of the data with the proper intercepts was generated. In order to determine the magnitude of difference between the data sets, the two data sets were fitted with one curve. This curve, the chapter 5 fit and the chapter 2 fit are shown along with all the spin coating data in figure 7.

Figure 7 shows that the curves from the two data sets were very similar, however, the chapter 5 data is not as steep as the data from chapter 2. When both data sets were fitted together, the curve was very similar in shape to both curves and also indicated that the difference in Peclet number was not very large between the two data sets.

5.4.1 Effect of spin speed

From equation one, the Peclet number depends on the square of the spin speed (ω^2). In experiments, the spin speed was set by entering the desired rotation rate into a digital controller. Since the two different data sets were collected two years apart it was possible that the spin coater functioning was altered in some way. To shift the data from this chapter to the right it was necessary for the actual spin speed to be higher than the value entered into the controller. However, it was unlikely that equipment aging would have resulted in an increase in spin speed. It was much more likely that the actual spin speed would be lower than the value entered into the controller due equipment aging, and wear or buildup on the motor or chuck.

Currently, we lack the means to directly measure the rotation rate of the spin coater. Therefore, in order to determine if variation of the spin speed could be responsible for the shift in the Peclet number curve we varied spin speed and calculated the corresponding Peclet number to determine the difference required to obtain the shift. For these experiments, Peclet numbers were recalculated by replacing ω with rotation rates of 1.1ω, 1.25ω and 1.5ω. Each data set was fit with an inverse tangent curve and compared to the curve fit from both the original chapter 5 fit and the chapter 2 fit. This is shown in figure 7.

To correct for a possible underestimation of the spin speed, it was evident that an increase in spin speed produced the desired rightward shift of the curve. However, we found that the steepness of the curves changed much more slowly than the shift. From figure 8, a fifty percent or greater error shift would be required for the curves to overlay. Additionally, the steepness of the curve was not affected by the spin speed

correction. This indicated that it was very unlikely that the shift would be the result of an incorrect value of spin speed.

5.4.2 Effect of particle size

An inaccurate estimate of particle radius could also contribute to the Peclet number discrepancy. Peclet number depends on particle radius (a) to the third power. Because of limitations on the quantity of particles that could be synthesized in a single batch, different batches of particles were used for the two sets of experiments. Particles used in the experiments in chapter 2 were 1.05μm in diameter and particles used in this chapter had a diameter of 0.68μm. Particle size and polydispersity for each batch were determined using scanning electron microscopy (SEM). To use SEM, a dilute sample of particles suspended in hexane were dried on an SEM stub and sputter coated with a mixture of gold and platinum to make the surface conductive. The beam was maintained at a low intensity to prevent deformation or melting of the particles, thus limiting resolution. The particles were sized from SEM images using ImageJ software. The problem with sizing particles using SEM was that the particles were dried, whereas in experiments they were being used in a suspension. Since PMMA particles tend swell or shrink in organic solvents, the actual particle size may be larger or smaller than the size determined by SEM.

Another important consideration in determining the radius was the application of the electropotential of each batch of particles. The PMMA particles were charged and repulsive in nature and tetrabutylammoniumchloride (TBAC) was added to particle suspensions in micromolar concentrations to screen the charges. The quantity of salt

added to each batch of particles was selected based one two criteria: first, at a volume fraction of 35% the particles crystallized quiescently in approximately 24 hours, and second, 35% suspensions formed steady state crystals via spin coating. The two batches of particles required different amounts of salt to meet these criteria. The batch from chapter 2 required 13μM or TBAC and the batch used in these experiments required 10μM The coexistence boundaries for the two batches were also different. In chapter 2 the coexistence range was between $\Phi = 0.17$ and $\Phi = 0.225$ compared to the coexistence range in this chapter of $\Phi = 0.175$ to $\Phi = 0.215$.

A difference in potential may also mean a difference in Debye length for the two batches and thus a different size ratio than revealed by sizing dry particles via SEM. The Debye length was defined as the repulsive layer surrounding each particle that created an excluded volume that no other particles could enter. Since no particles could enter the Debye layer, the particle radius should actually be defined as the radius of the particle plus the debye length instead of just the dry particle size. Because different amounts of salt were required to stabilize each batch, it is likely that the Debye length was different in each set of particles. Because the batch from chapter 2 required more salt, it is likely that the Debye length would be larger, skewing the particle radius even further. Also, basic properties of spheres under flow could contribute to size-related discrepancies. For example, larger particles are affected much more by convective flow than smaller particles.

To determine if the discrepancy in the two data sets could be a result of error in particle size determination, Peclet numbers for chapter 5 data we recalculated using

three different values for the radius: 1.1a, 1.25a, 1.5a. The data sets were fitted with the inverse tangent curve and plotted below along with the fits from both original data sets.

Figure 9 shows that for an error in the particle size of 25%, the curve shifts far enough to the right to overlay the chapter 5 data. However, the shape of the curve does not get steeper with the change in particle size error. Because there is not much known about the potential of charged spheres in DOP it is possible when taking into account the Debye layer thickness the error in size is significant. However, since the Debye layer thickness was not accounted for in either data set, an error of similar magnitude would occur in the particles for both chapters and both curves would shift to the right. Therefore, unless the two batches of particles have significantly different surface potentials, it is unlikely that the error would correct for the shift.

5.4.3 Effect of radial position

Peclet number is also affected by radial and axial position in the sample. Peclet number varies linearly with the radial position in the sample. Because of the precision of the z-galvo it was highly unlikely that significant error would occur in the z position of the sample. The other possibility for error would be error in judging the radial position. The uncertainty of the confocal positions was on the order of hundredths of microns so the error in position would not cause significant deviations.

5.5 Conclusions

The results in this chapter indicate that for suspensions in the crystalline volume fraction regime follow the Peclet number theory, however, for concentrations above the glass transition and in the coexistence fraction, crystallinity is negligible. After

examination of variation in spin speed, particle size, and position in the sample we determined that even though spin speed or particle size underestimates could account for the curve shifts, neither of these variables alone could account for the differences in the curves for the chapter 2 and the chapter 5 data. Curves did not become steeper with the spin speed or particle size corrections. The fit of both the data sets together indicates that there is not a significant difference between the two curves. The similarity of results indicates there may be a minor experimental difference in the two data sets causing the shift. This leads us to conclude that the Peclet number theory is applicable to both data sets and therefore all the data with volume fractions in the crystalline regime. Additionally, we conclude that the difference between the data from chapter 2 and chapter 5 is not significant.

1. Pusey PN, Vanmegen W. *Phase-behavior of concentrated suspensions of nearly hard colloidal spheres,* Nature 1986; 320(6060):340-342.

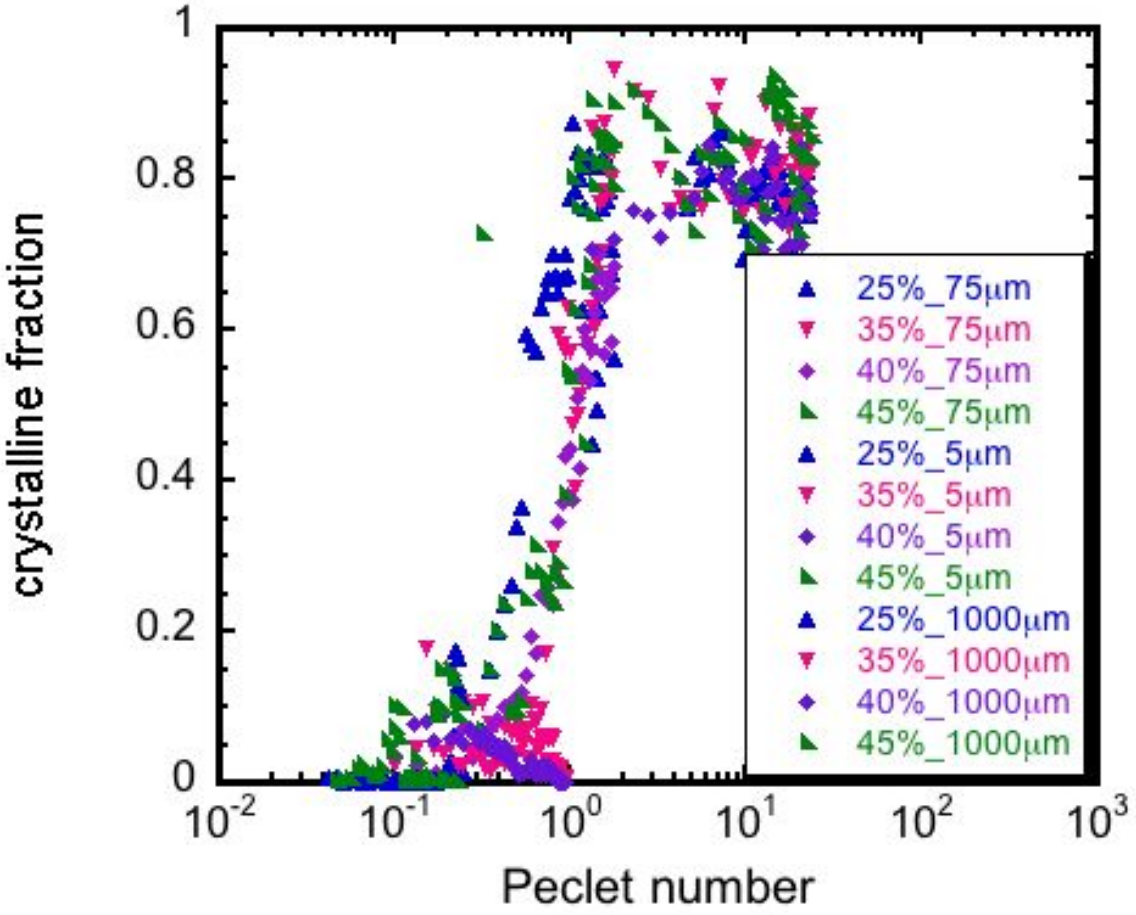

Figure 1: Crystal quality as a function of Peclet number for volume fractions in the crystalline regime (Φ = 0.25, 0.35, 0.40 , 0.45). Samples were spin coated at a rate of 600rpm for a duration of 3 minutes. Each point is an average of five different independent samples.

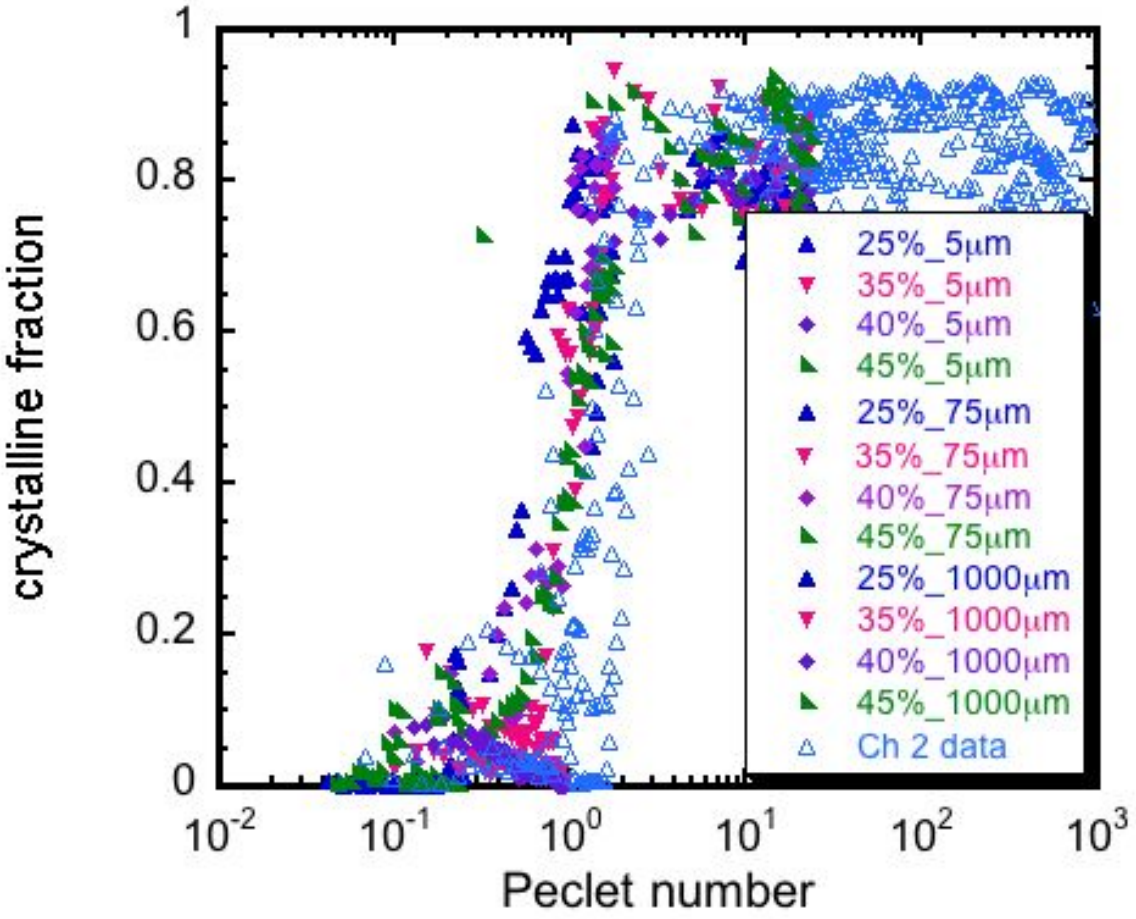

Figure 2: Spin coating data from figure 1 plotted with the spin coating Peclet number data from chapter 2. Chapter 2 data are unshaded. Each point in the new data was spin coated at a rate of 600rpm for a duration of 3 minutes and averaged over five independent samples. Old data incorporated different spin speeds, particle sizes, and radial positions.

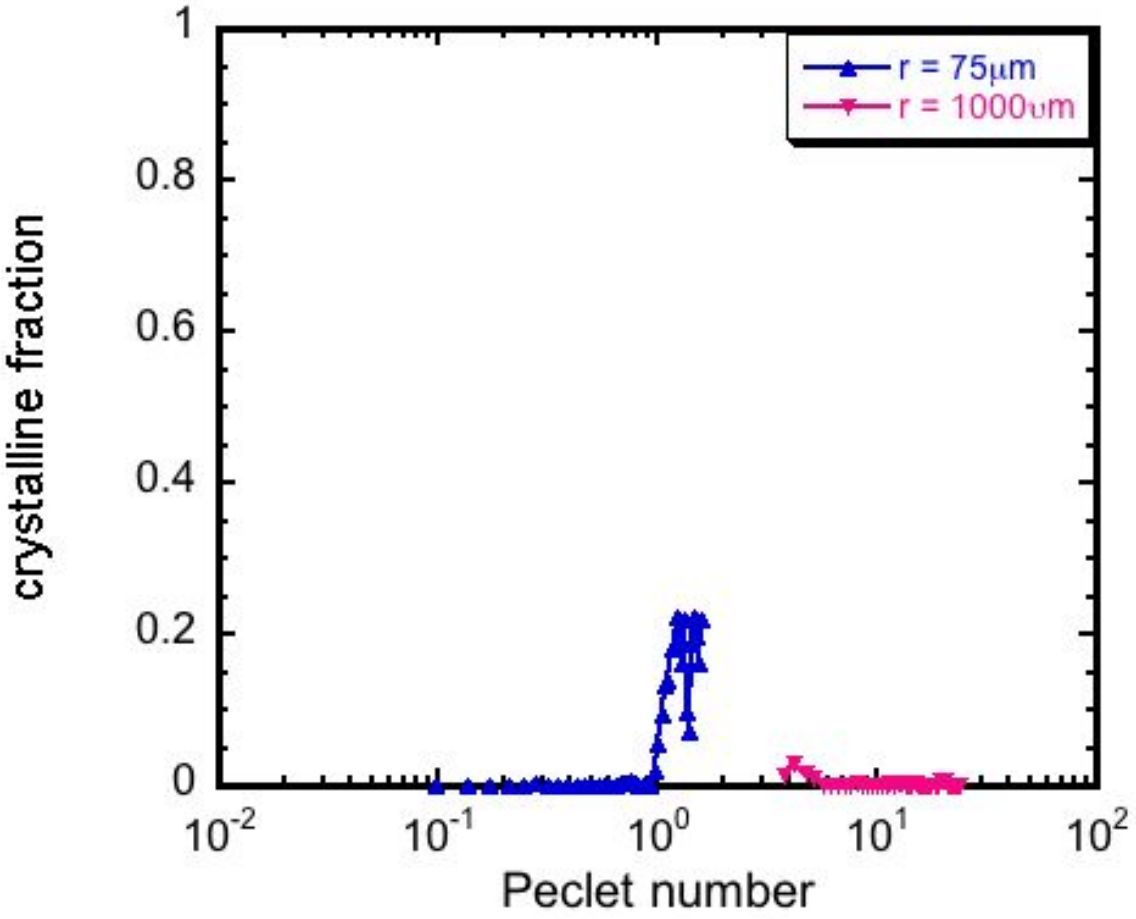

Figure 3: Crystal quality versus Peclet number in the coexistence regime. Each point in the new data was spin coated at a rate of 600rpm for a duration of 3 minutes. Samples were imaged at radial positions of 75 microns and 1000microns from the axis of rotation.

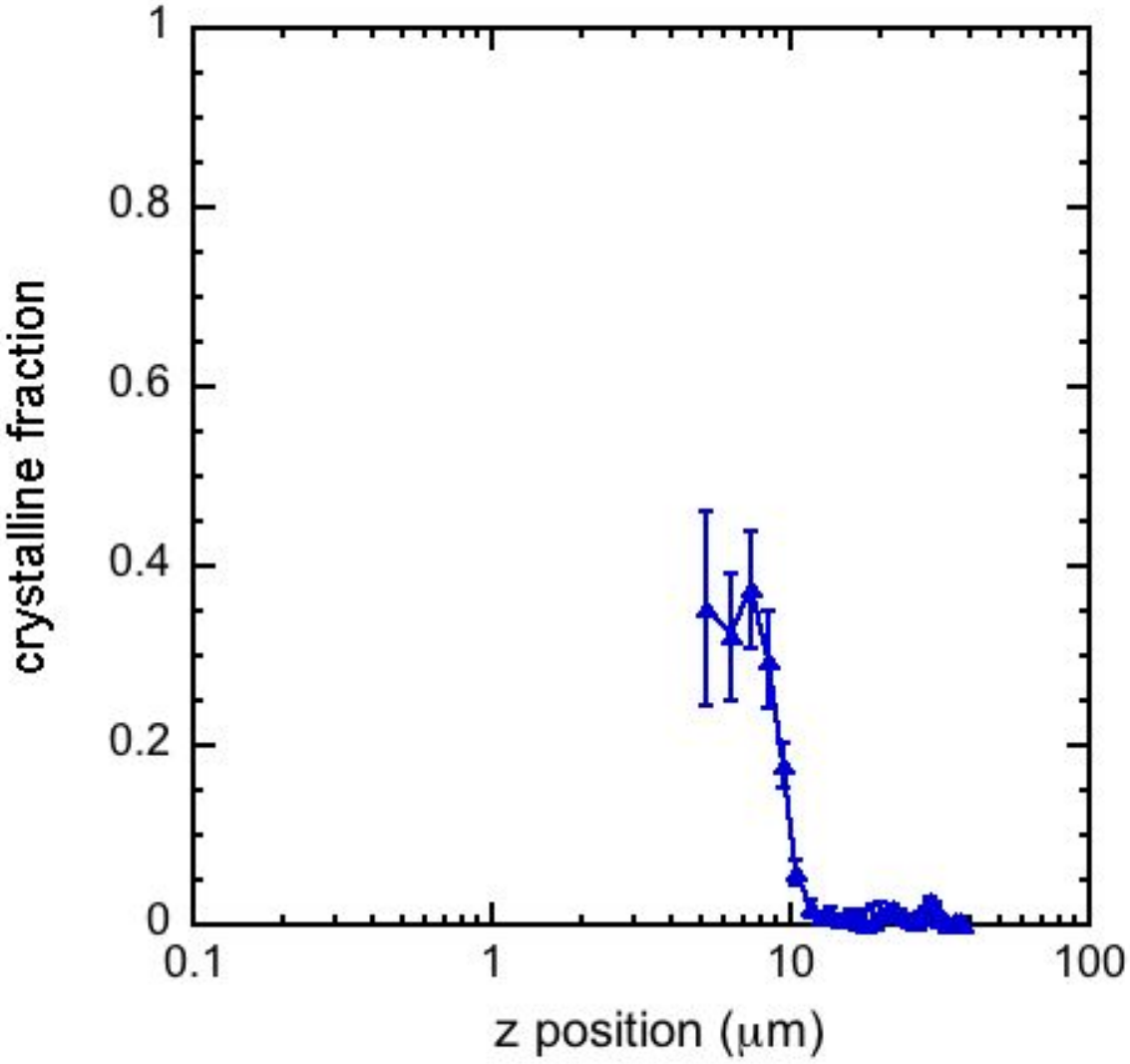

Figure 4: Crystal quality versus Peclet number for a volume fraction above the glass transition (Φ = 0.50). Samples were imaged at a radial position 1000 microns from the axis of rotation.

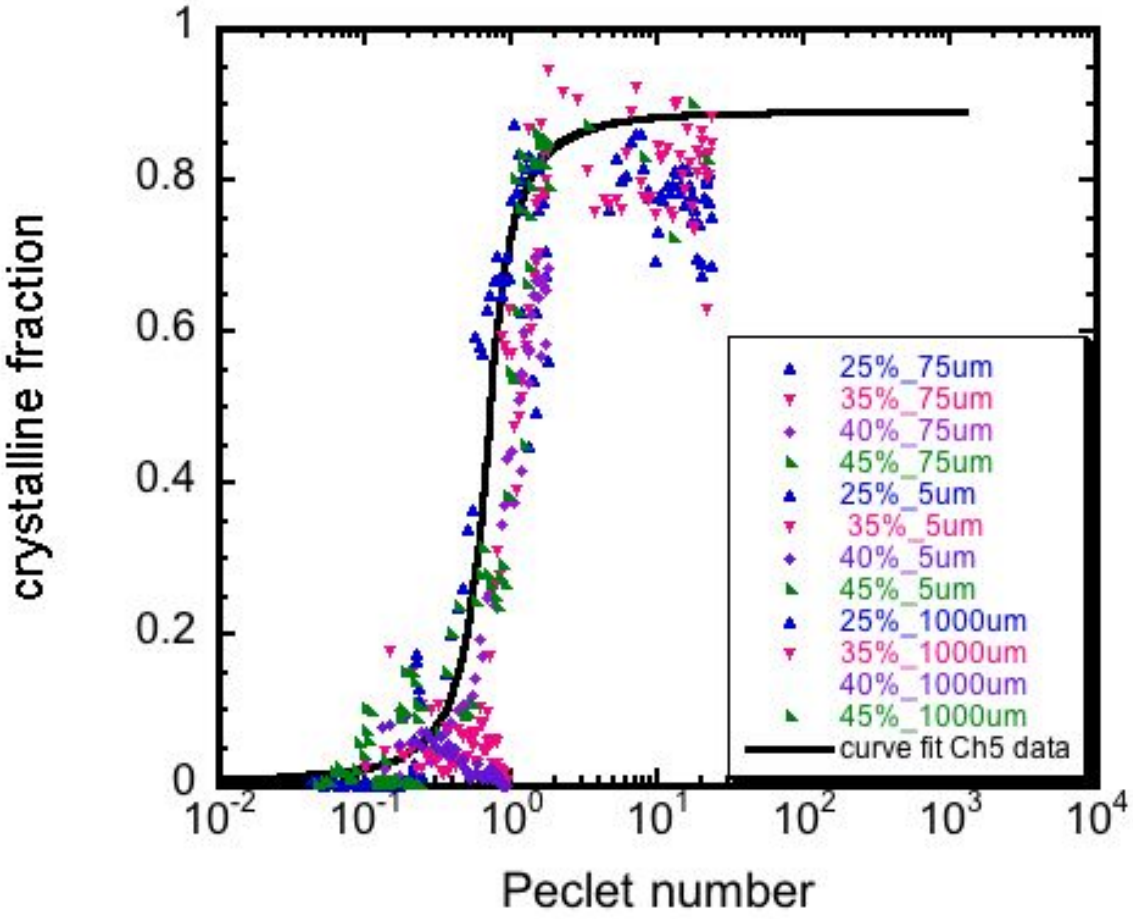

Figure 5: Peclet number data from chapter 5 plotted and fitted with an inverse tangent curve from equation 2. Only data is the crystalline regime are plotted.

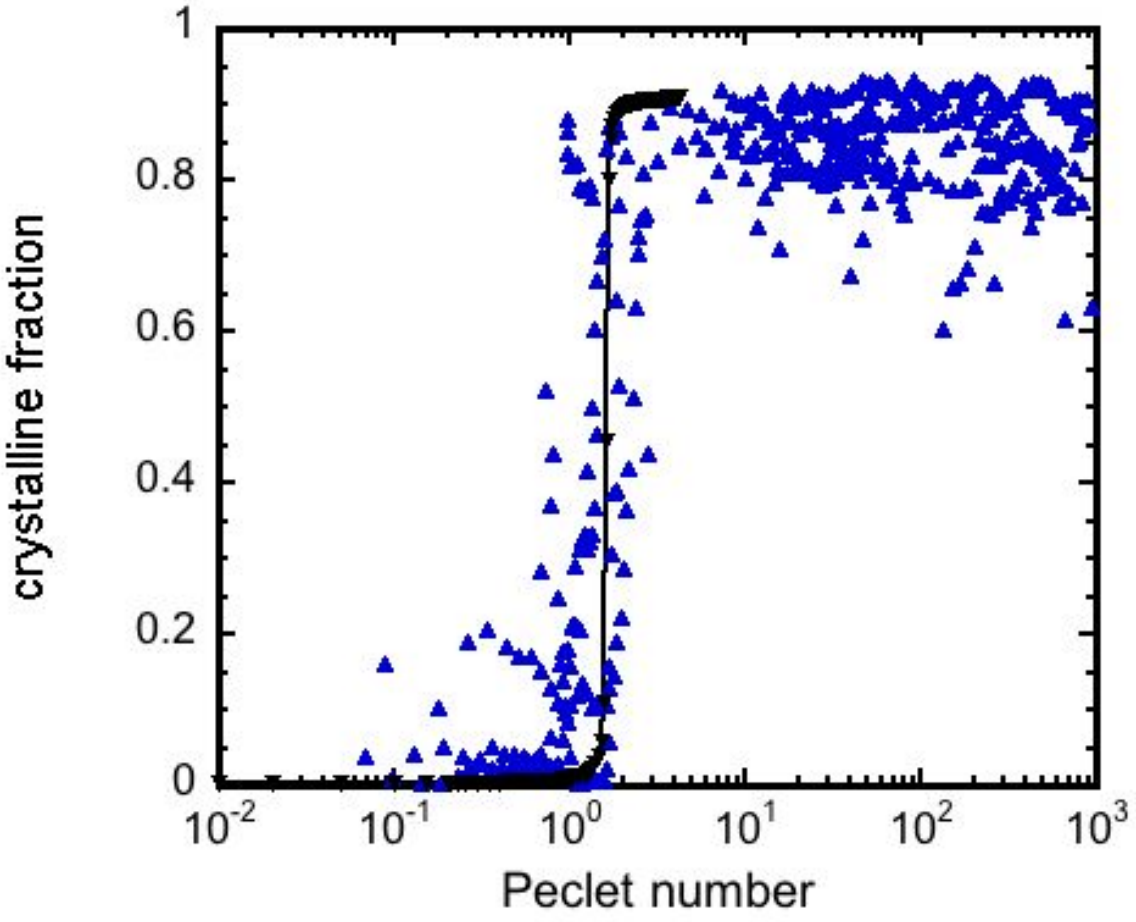

Figure 6: spin coating data from chapter 2 fitted with an inverse tangent curve. The form of the equation is given in equation 2.

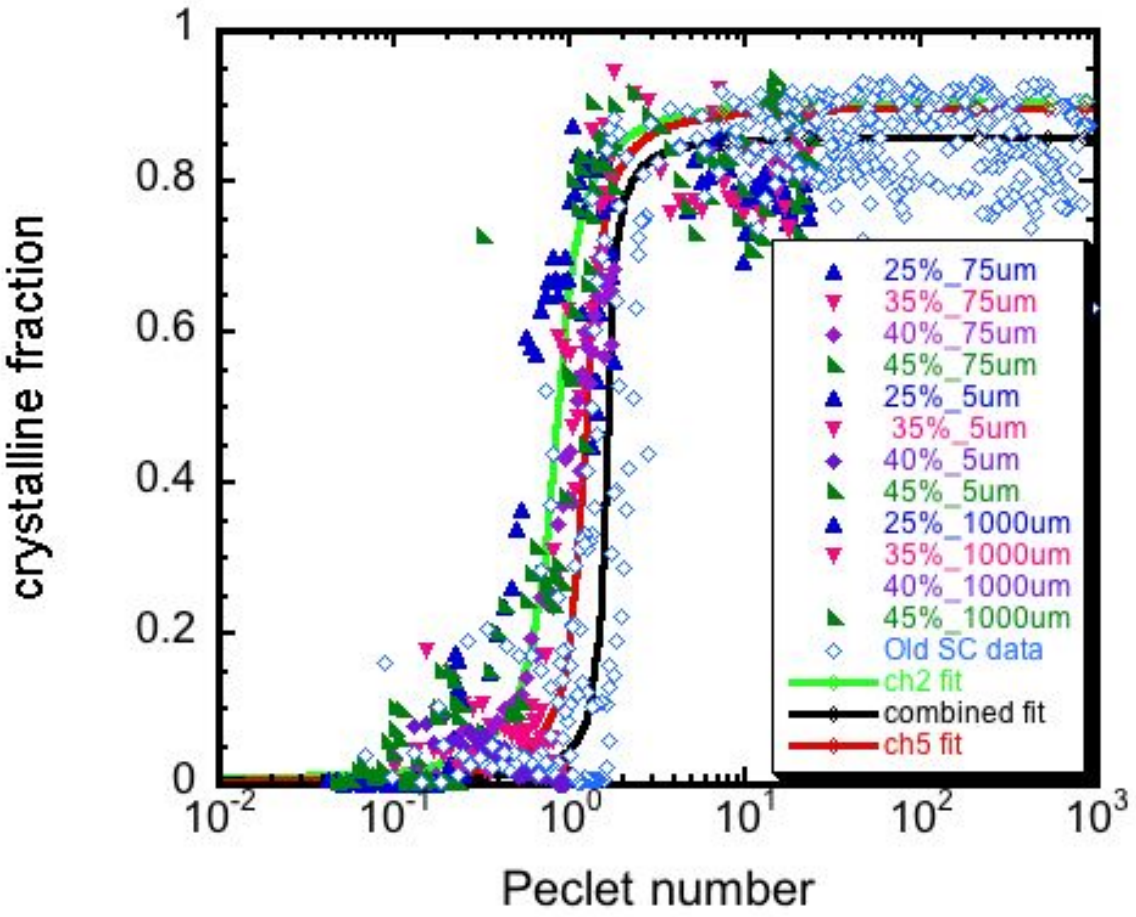

Figure 7: All chapter 2 and chapter 5 data for volume fractions are plotted as a function of Peclet number. The three curve fits represent the curve fits for both chapter 2 and chapter 5 data sets as well as an inverse tangent fit of all of the data combined.

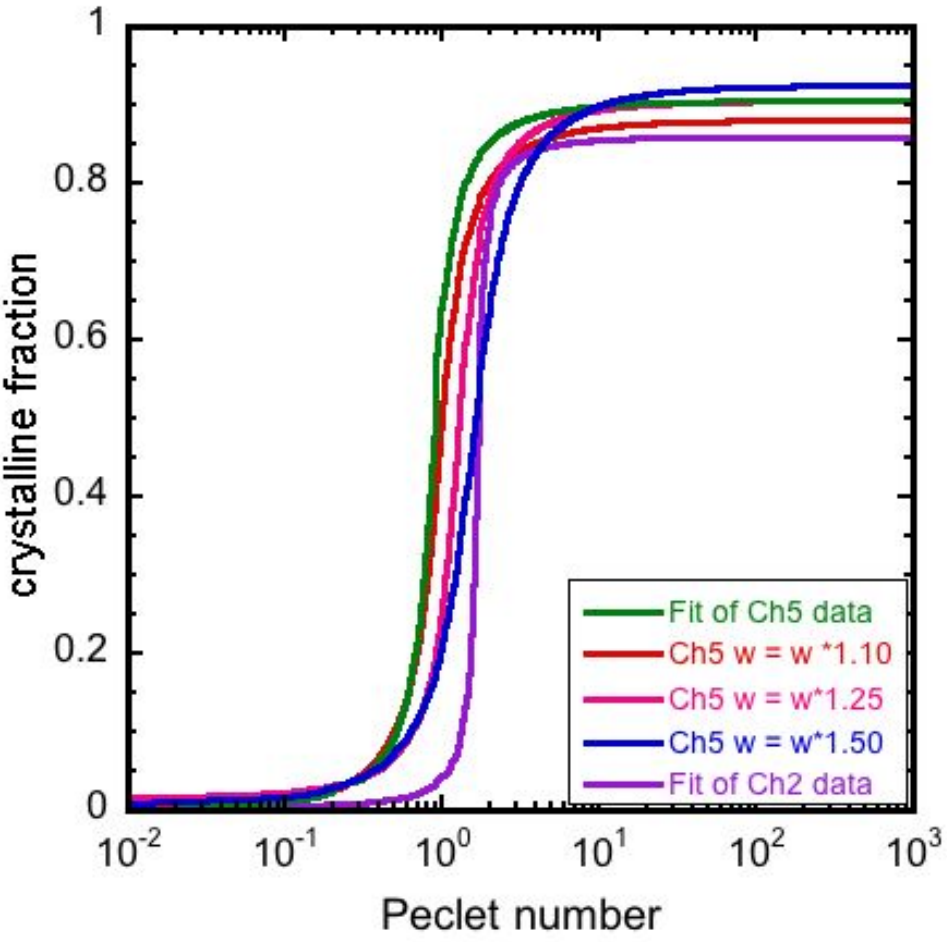

Figure 8: Determining the effect of error in estimating spin speed for spin coated samples. The curves shown are the fits for the original data from chapter 2 and chapter 5. The remaining curves show fits for a 10%, 25%, and 50% error in spin speed.

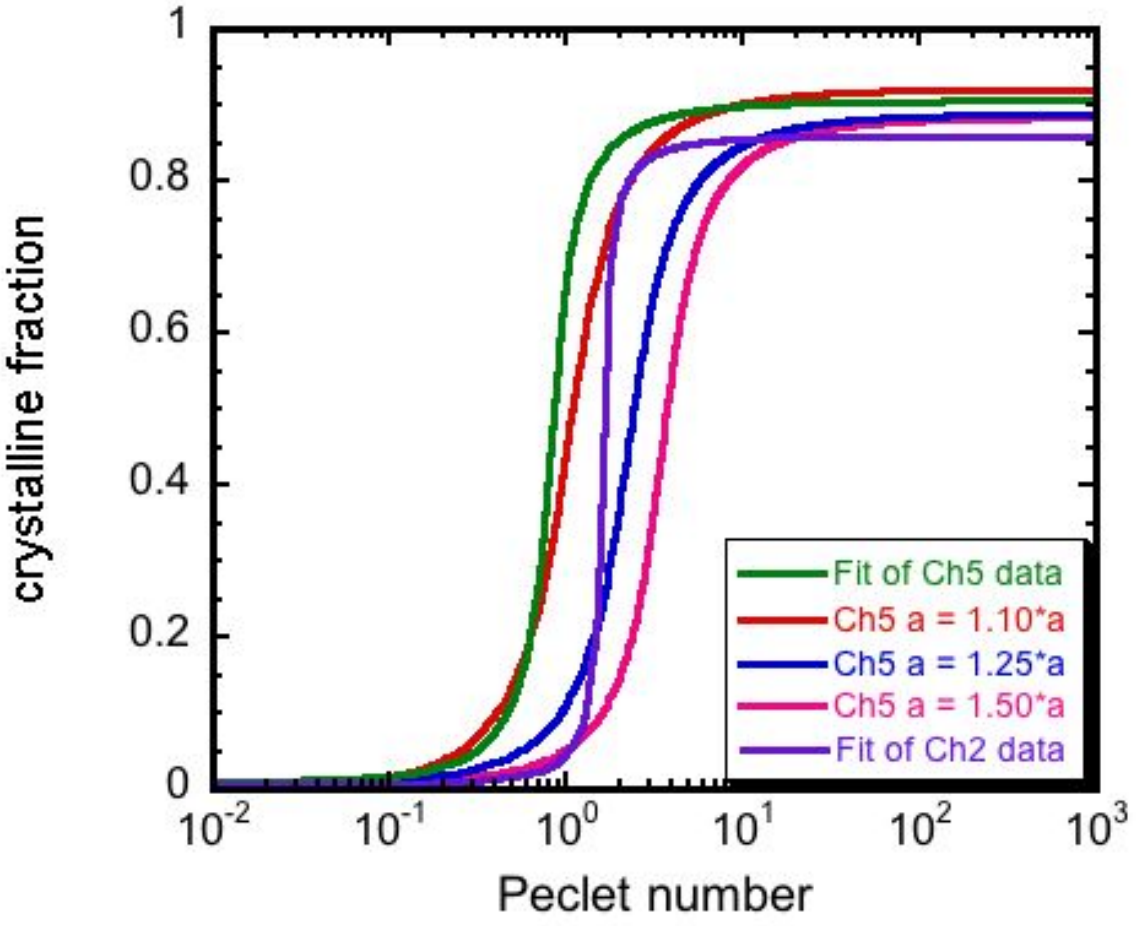

Figure 9: Determination of the effect of particle size (a) on the order to disorder transition. The green curve is the original curve where a = a. The next three curves show the corrections assuming that the particle size was underestimated by 10%, 25%, and 50%. The purple curve is the curve fit for the chapter 2 data.

CHAPTER 6

Summary and Conclusions

6.1 Conclusions

In this paper we have demonstrated that the kinetics of the order to disorder transition in dense colloidal suspensions undergoing shear flow can be predicted using the dimensionless stress-based Peclet number. We used a model colloidal system of suspensions of fluorescently stained 12-(hydroxystearic acid) stabilized poly(methylmethacrylate) particles dispersed in dioctyl phthalate, 7% photopolymer and 1% initiator for all experiments. Tetrabutylammoniumchloride was used to screen the charges. The colloid fraction remained constant at 35% with the exception of the work in chapter 5. In chapter 2, we established the critical stress and strain criteria for colloidal crystal formation in spin coating flows. In chapter 3, we determined the strain necessary to form colloidal crystals under simple shear flow. We found the strain necessary for crystal formation in simple shear flow was significantly greater than that required for spin coating. In chapter 4, we discovered that in simple shear, an application of a strain less than that required for full crystallization resulted in a significant acceleration of the movement of the crystalline boundary from the quiescent control.

From chapter 2 we concluded that spin coating is a fast way to make high quality multilayer colloidal crystals over large domains. Spin coating produced crystals four orders of magnitude faster than quiescent crystallization. Through experiments we established spin coating to be a stressed controlled process with an disorder to order transition at a Peclet number of unity. The validation of the Peclet number theory was assessed by variation of spin speed, particle size, and spatial orientation. Axial and radial variation were also determined experimentally. Local bond order measurements indicated formation of fully crystalline structures. Additionally, we determined that a macroscopic strain of two or greater was required for crystal formation. This result was surprising, as previous studies of simple and oscillatory shear had required hundreds to thousands of strain units to achieve full crystallization.

The surprisingly low strain requirements for crystal formation in spin coating brought about the investigation of strain required for colloidal crystal formation in suspensions undergoing simple shear. From the experiments presented in chapter 3 it was evident that crystal quality in sheared concentrated colloidal suspensions was a function of the applied strain. Experimental data showed that crystals formed at lower strains than previously reported in literature and that the crystalline boundaries propagated from the walls. Strain was found to be inhomogeneous in the samples studied, and the inhomogeneity was correlated with the movement of the crystalline boundary. A strain of 160 was required to achieve crystallization under the experimental conditions presented in chapter 3. Step strain deformations were investigated for varying Peclet numbers above unity. The results indicated that as long as the Peclet number was above a critical Peclet number, crystals formed at very similar rates. Additionally, we showed that the

growth of the crystalline boundary could be modeled as a one-dimensional crystallization. The height of the crystalline boundary as a function of applied strain was fitted by two lines, the steeper line at the lowest strains.

Finally, we showed crystallization rate to be a function of the gap. For each gap tested, the crystal growth rate could be fit by two lines, with the lowest strain line being steeper. We hypothesize the change in slope is due to the boundaries beginning to interact with one another.

In chapter 4 we established that application of strain less than that required for full crystallization resulted in a significant increase in crystallization rate from the quiescent rate. However, this rate was slower that the time required for full crystallization from application of shear. For the two different strains were tested (10 and 40), growth rate upon cessation of shear was the same. We hypothesize that this is a result of templating.

In these chapters we modeled both a uniform and non-uniform shear process for colloidal crystallization as stress and strain controlled. We established the critical criteria for spin coating and simple shear using the dimensionless Peclet number. This will have further implications in modeling other forms of flow-induced crystallization as well as use in creation of advanced materials.

6.2 Future work

To further pursue the fundamental study of shear flow on dense colloidal crystals, several experiments could be done. For example, further studies of the dynamics of simple shear flow could be conducted to help understand the inhomogeneous nature of the velocity profile under shear flow. Using a spinning disc confocal or a scanning

confocal microscope with a faster camera, dynamics could be studied at a much larger range of flow rates. This would allow further exploration of the strain inhomogeneity correlation with the velocity profile. It would also give a better physical understanding on how particles move under flow and if they maintain a constant z position throughout.

Rheological studies should be conducted on the samples in chapter 3 to determine how transitions in macroscopic rheological properties correspond to the microstructural changes observed by confocal microscopy. Equivalent amounts of shear could be applied in the shear cell and in a parallel plate configuration on the ARG2 rheometer to directly compare the rheological properties and microstructure. Ideally, a setup could be designed to allow direct visualization or even scattering performed simultaneously with the rheological data collection.

Colloidal crystals are already being used in sensing applications as well as tissue scaffolds, and are being explored as possible photonic materials. Work should also be done to incorporate these crystals into different applications. Once the defect density of the materials produced is established, experiments should be performed to see if these crystals can be used in highly sensitive materials like photonic crystals. Knowing the specifications desired by these application-based scientists would move colloidal crystal technology into the future.

In this thesis we have presented a comprehensive analysis of critical stress and strain criteria in both spin coating and simple shear flows. Our focus was on the fundamental science aspect of these processes, however, because these shear processes increase ordering by several orders of magnitude, the possibility for mass production and industrial use should be explored. In order to determine suitability of these methods for

various applications, it would be necessary to determine the quality of the crystals formed by each method. Not only would local structure need to be assessed – as in the experiments presented here - but assessment of global, long range order would also be required. Long range ordering could be assessed using scanning electron microscopy and cross sections could be examined by removing sections with an ion beam. Additionally, scattering and FTIR could be performed and a band gap could be determined. Local defect analysis could be completed using the methods of Solomon and Solomon[80].

Appendix A: poly(methylmethacrylate) particle synthesis

Equipment

1-250mL, 3-neck flask

1-125mL erlynmeyer flask

Ahllin condenser

4 Teflon sleeves

2 thermometers (at least 150C range)

2-100mL beakers

Dean Stark apparatus

Thermometer adapter with 24/40 fitting

1 small spatula

1 extra large spatula

Oil bath

In the table below, sample recipes for two different sizes of particles are shown.

	1.25um	2.1um
Species	Targe wt (g)	Target wt (g)
Hexane	21.98	21.38
Dodecane	10.98	10.97
PHSA stabilizer	1.75	1.74
ADIB	0.2772	0.2786
Nile red dye	0.0084	0.0071
Methyl methacrylate	32.54	34.87
Methacrylic acid	0.672945	0.72268
1-octanethiol	0.175344	0.175344

Procedure:

1. Weigh out hexane and dodecane in the 3 neck flask
2. Weigh out the desired amount of stabilizer directly into the 3-neck-flask. Shake the flask until the stabilizer appears to be dissolved.
3. Set up the apparatus as shown in figure 7. Figure 8 shows a closeup of the PMMA setup.

.

Figure A1: PMMA synthesis setup

Figure A2: closeup of PMMA synthesis setup

4. Turn on the oil bath and heat the flask to 80C. Once the flask reaches 80C allow it to remain at 80C for 30 minutes.
5. In a small beaker, weigh out the desired amount of ADIB in one small beaker and Nile red dye in the other.
6. Weigh out methyl methacrylate in the 125mL erlynmeyer flask and add approximately 30mL to each beaker and stir until the ADIB and dye are both dissolved. Use a spatula to crush the ADIB if necessary.
7. Ad the dye and ADIB solution to the flask with the methyl methacrylate.
8. Add methacrylic acid to the beaker using a micropipette.

Warning: 1-octanethiol stinks up the lab for 2 days so do not remove the bottle from the hood for at least one hour after use. Also, after dispensing the 1-octanethiol, leave your gloves in the hood for at least an hour as well.

9. Using the electronic micropipette, add the 1-octanethiol to the beaker. Remove your gloves and leave them in the hood. Get a new pair of gloves.
10. Stir the mixture gently and cover with parafilm.
11. After the flask with the solvents and stabilizer has been maintained at 80C for 30 minutes, add the mixture in the flask to the 3-neck flask through one of the side necks via a glass funnel.
12. With a large, clean spatula, mix the contents of the flask with several quick strokes.
13. Replace the plug in the side neck.
14. Once the mixture has been added, record the time. Allow the reaction to proceed at 80C for two hours.

15. After reacting for two hours, add the Dean Stark apparatus into the setup between the condenser and the flask.
16. Add dodecane to the flask through one of the side necks. The amount of dodecane that should be added is the weight of hexane added in the first step. Add 0.16g N,N-dimethylethanolamine to the flask via micropipette. Replace the glass plug quickly once the liquid is added.
17. Replace one of the glass plugs with a thermometer and thermometer adapter.
18. Submerge the tip to the thermometer in the flask into the reaction mixture.
19. Increase the oil bath temperature until it reaches 140C.
20. Distill the hexane from the Dean-Stark until the temperature inside the flask reaches 118C.
21. Maintain the temperature in the flask at 120C for 12 hours.
22. After 12 hours, allow the flask to cool and transfer particles into a glass container with a Teflon lid.
23. Clean particles at least 8 times by centrifuging the particles for one hour at 7500 RPM and removing the solvent (15 minutes per cycle is sufficient).
24. Use SEM to determine particle size and polydispersity.

** Based on the procedures outlined in the stabilizer handbook - unpublished

Appendix B: photoinitiator absorption spectrum

Absorption Spectrum
(% in Acetonitrile)

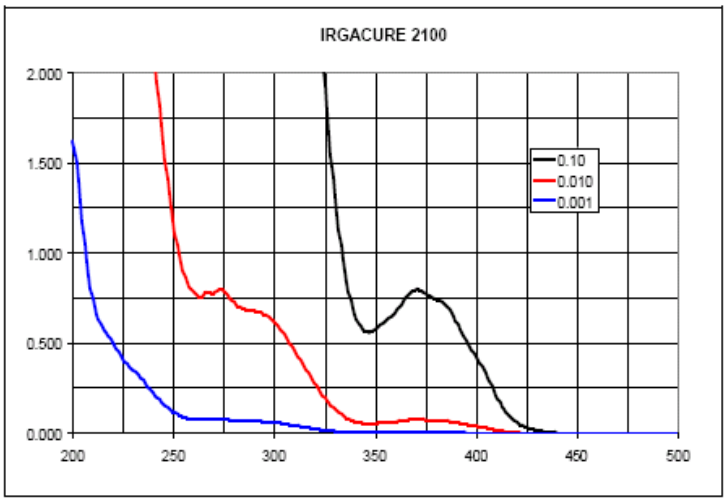

Image from Ciba Specialty

References

1. Ackerson, B.J., *Shear induced order in equilbrium colloidal liquids* in *Physica A*. 1991. p. 15-30.
2. Crocker, J.C., D.G. Grier, and Ug, *Methods of digital video microscopy for colloidal studies.* Journal of Colloid and Interface Science, 1996. **179**(1): p. 298-310.
3. tenWolde, P.R., M.J. RuizMontero, and D. Frenkel, *Numerical calculation of the rate of crystal nucleation in a lennard-jones system at moderate undercooling.* Journal of Chemical Physics, 1996. **104**(24): p. 9932-9947.
4. Dinsmore, A.D., et al., *Colloidosomes: Selectively permeable capsules composed of colloidal particles*, in *Science*. 2002. p. 1006-1009.
5. Davis, K.E., W.B. Russel, and W.J. Glantschnig, *Settling suspensions of colloidal silica - observations and x-ray measurements*, in *Journal of the Chemical Society-Faraday Transactions*. 1991. p. 411-424.
6. vanBlaaderen, A. and P. Wiltzius, *Growing large, well-oriented colloidal crystals*, in *Advanced Materials*. 1997. p. 833-& **9**(10).
7. Mezzenga, R., et al., *Understanding foods as soft materials*, in *Nature Materials*. 2005. p. 729-740.
8. Baljon, A.R.C. and M.O. Robbins, *Energy dissipation during rupture of adhesive bonds*, in *Science*. 1996. p. 482-484.
9. Lewis, J.A., *Colloidal processing of ceramics*, in *Journal of the American Ceramic Society*. 2000. p. 2341-2359.
10. Lewis, R. and R.S. Dwyer-Joyce, *Interactions between toothbrush and toothpaste particles during simulated abrasive cleaning*, in *Proceedings of the Institution of Mechanical Engineers Part J-Journal of Engineering Tribology*. 2006. p. 755-765.
11. Hong, L., S.M. Anthony, and S. Granick, *Rotation in suspension of a rod-shaped colloid*, in *Langmuir*. 2006. p. 7128-7131.
12. Cush, R., D. Dorman, and P.S. Russo, *Rotational and translational diffusion of tobacco mosaic virus in extended and globular polymer solutions*, in *Macromolecules*. 2004. p. 9577-9584.
13. Whitesides, G.M. and M. Boncheva, *Beyond molecules: Self-assembly of mesoscopic and macroscopic components*, in *Proceedings of the National Academy of Sciences of the United States of America*. 2002. p. 4769-4774.
14. Horsch, M.A., Z. Zhang, and S.C. Glotzer, *Self-assembly of laterally-tethered nanorods*, in *Nano Letters*. 2006. p. 2406-2413.
15. Graham-Rowe, D., *Tunable structural colour*, in *Nature Photonics*. 2009. p. 551-553.
16. Kubo, S., et al., *Control of the optical properties of liquid crystal-infiltrated inverse opal structures using photo irradiation and/or an electric field*, in *Chemistry of Materials*. 2005. p. 2298-2309.
17. Blaak, R., et al., *Crystal nucleation of colloidal suspensions under shear*, in *Physical Review Letters*. 2004.
18. Pusey, P.N. and W. Vanmegen, *Phase-behavior of concentrated suspensions of nearly hard colloidal spheres*, in *Nature*. 1986. p. 340-342.

19. Chen, L.B., B.J. Ackerson, and C.F. Zukoski, *Rheological consequences of microstructural transitions in colloidal crystals*, in *Journal of Rheology*. 1994. p. 193-216.
20. Russel, W.B. and W.R. Schowalter. 1989: Cambridge University Press.
21. Gasser, U., et al., *Real-space imaging of nucleation and growth in colloidal crystallization*, in *Science*. 2001. p. 258-262.
22. Larson, R.G., *The structure and rheology of complex fluids*. 1999, Oxford: Oxford University Press.
23. Prasad, V., D. Semwogerere, and E.R. Weeks, *Confocal microscopy of colloids*, in *Journal of Physics-Condensed Matter*. 2007. p. 25.
24. Hynninen, A.P., et al., *Cuau structure in the restricted primitive model and oppositely charged colloids*, in *Physical Review Letters*. 2006. p. 4.
25. Royall, C.P., M.E. Leunissen, and A. van Blaaderen, *A new colloidal model system to study long-range interactions quantitatively in real space*, in *Journal of Physics-Condensed Matter*. 2003. p. S3581-S3596.
26. Anderson, V.J. and H.N.W. Lekkerkerker, *Insights into phase transition kinetics from colloid science.* Nature, 2002. **416**(6883): p. 811-815.
27. Auer, S. and D. Frenkel, *Prediction of absolute crystal-nucleation rate in hard-sphere colloids.* Nature, 2001. **409**(6823): p. 1020-1023.
28. Velev, O.D. and S. Gupta, *Materials fabricated by micro- and nanoparticle assembly - the challenging path from science to engineering*, in *Advanced Materials*. 2009. p. 1897-1905.
29. Pronk, S. and D. Frenkel, *Large effect of polydispersity on defect concentrations in colloidal crystals*, in *Journal of Chemical Physics*. 2004. p. 6764-6768.
30. Jiang, P., *Large-scale fabrication of periodic nanostructured materials by using hexagonal non-close-packed colloidal crystals as templates*, in *Langmuir*. 2006. p. 3955-3958.
31. Wang, D.Y. and H. Mohwald, *Template-directed colloidal self-assembly - the route to 'top-down' nanochemical engineering*, in *Journal of Materials Chemistry*. 2004. p. 459-468.
32. Vermant, J. and M.J. Solomon, *Flow-induced structure in colloidal suspensions*, in *Journal of Physics-Condensed Matter*. 2005. p. R187-R216.
33. Jiang, P., et al., *Single-crystal colloidal multilayers of controlled thickness*, in *Chemistry of Materials*. 1999. p. 2132-2140.
34. Zahn, K., J.M. MendezAlcaraz, and G. Maret, *Hydrodynamic interactions may enhance the self-diffusion of colloidal particles*, in *Physical Review Letters*. 1997. p. 175-178.
35. Wen, W.J., L.Y. Zhang, and P. Sheng, *Planar magnetic colloidal crystals*, in *Physical Review Letters*. 2000. p. 5464-5467.
36. Hansen, J.P. and H. Lowen, *Effective interactions between electric double layers*, in *Annual Review of Physical Chemistry*. 2000. p. 209-242.
37. Solomon, T. and M.J. Solomon, *Stacking fault structure in shear-induced colloidal crystallization*, in *Journal of Chemical Physics*. 2006. p. 10 **124**(13).
38. Jiang, P. and M.J. McFarland, *Large-scale fabrication of wafer-size colloidal crystals, macroporous polymers and nanocomposites by spin-coating*, in *Journal of the American Chemical Society*. 2004. p. 13778-13786.

39. Ackerson, B.J., *Shear induced order and shear processing of model hard-sphere suspensions*, in *Journal of Rheology*. 1990. p. 553-590.
40. Ackerson, B.J., *Shear induced order in equilibrium colloidal liquids*, in *Physica A*. 1991. p. 15-30.
41. Ackerson, B.J. and T.A. Morris, *Shear induced order of concentrated dispersions*, in *Better Ceramics through Chemistry Iv*. 1990. p. 159-166.
42. Ackerson, B.J., *Shear induced order and shear processing of model hard-sphere suspensions.* Journal of Rheology, 1990. **34**(4): p. 553-590.
43. W.B. Russel, D.A.S., W.R. Schowalter, *Colloidal dispersions*. 1989, New York City: Press Syndicate of the University of Cambridge. 525.
44. Ackerson, B.J. and P.N. Pusey, *Shear-induced order in suspensions of hard-spheres.* Physical Review Letters, 1988. **61**(8): p. 1033-1036.
45. Bender, J. and N.J. Wagner, *Reversible shear thickening in monodisperse and bidisperse colloidal dispersions.* Journal of Rheology, 1996. **40**(5): p. 899-916.
46. Jiang, P. and M.J. McFarland, *Large-scale fabrication of wafer-size colloidal crystals, macroporous polymers and nanocomposites by spin-coating.* Journal of the American Chemical Society, 2004. **126**(42): p. 13778-13786.
47. Emslie, A.G., F.T. Bonner, and L.G. Peck, *Flow of a viscous liquid on a rotating disk*, in *Journal of Applied Physics*. 1958. p. 858-862.
48. Meyerhofer, D., *Characteristics of resist films produced by spinning*, in *Journal of Applied Physics*. 1978. p. 3993-3997.
49. Ackerson, B.J. and P.N. Pusey, *Shear-induced order in suspensions of hard-spheres*, in *Physical Review Letters*. 1988. p. 1033-1036.
50. Solomon, M.J. and M. Kogan, in *Encyclopedia of Condensed Matter Physics*.
51. Ackerson, B.J. and N.A. Clark, *Shear-induced melting*, in *Physical Review Letters*. 1981. p. 123-126.
52. Emslie, A.G., F.T. Bonner, and L.G. Peck, *Flow of a viscous liquid on a rotating disk.* Journal of Applied Physics, 1958. **29**(5): p. 858-862.
53. Antl, L., et al., *The preparation of poly(methyl methacrylate) lattices in nonaqueous media.* Colloids and Surfaces, 1986. **17**(1): p. 67-78.
54. Pathmamanoharan, C., K. Groot, and J.K.G. Dhont, *Preparation and characterization of crosslinked pmma latex particles stabilized by grafted copolymer.* Colloid and Polymer Science, 1997. **275**(9): p. 897-901.
55. Campbell, A.I. and P. Bartlett, *Fluorescent hard-sphere polymer colloids for confocal microscopy.* Journal of Colloid and Interface Science, 2002. **256**(2): p. 325-330.
56. Bosma, G., et al., *Preparation of monodisperse, fluorescent pmma-latex colloids by dispersion polymerization.* Journal of Colloid and Interface Science, 2002. **245**(2): p. 292-300.
57. Scully, P.J., et al., *Uvc laser photo-induced refractive index changes in poly-methyl-meth-acrylate and plastic optical fibres for application as sensors and devices.* 14th International Conference on Optical Fiber Sensors, 2000. **4185**: p. 854-857.
58. Solomon, M.J. and M. Kogan, *Confocal optical microscopy*, in *Encyclopedia of condensed matter physics*
2005, Oxford Academic Press.

59. Wu, LT., JHJ Brand, JLA van Gemant et al. *A new parallel plate shear c ell for in situ real-space measurements of complex fluids under shear flow*, Review of Scientific Instruments 2007 78(10)
60. Shereda, L.T., R.G. Larson, and M.J. Solomon, *Local stress control of spatiotemporal ordering of colloidal crystals in complex flows.* Physical Review Letters, 2008. **101**(3).
61. Krishnamurthy, L.N., N.J. Wagner, and J. Mewis, *Shear thickening in polymer stabilized colloidal dispersions.* Journal of Rheology, 2005. **49**(6): p. 1347-1360.
62. Gasser, U., *Crystallization in three- and two-dimensional colloidal suspensions.* Journal of Physics-Condensed Matter, 2009. **21**(20): p. 24.
63. Vermant, J. and M.J. Solomon, *Flow-induced structure in colloidal suspensions.* Journal of Physics-Condensed Matter, 2005. **17**(4): p. R187-R216.
64. Chen, L.B., B.J. Ackerson, and C.F. Zukoski, *Rheological consequences of microstructural transitions in colloidal crystals* Journal of Rheology, 1994. **38**(2): p. 193-216.
65. Wagner, N.J. and B.J. Ackerson, *Analysis of nonequilibrium structures of shearing colloidal suspensions.* Journal of Chemical Physics, 1992. **97**(2): p. 1473-1483.
66. Wu, Y.L., et al., *Melting and crystallization of colloidal hard-sphere suspensions under shear.* Proceedings of the National Academy of Sciences of the United States of America, 2009. **106**(26): p. 10564-10569.
67. Ackerson, B.J., *Shear induced order and shear processing of model hard-sphere suspensions*, in *Journal of Rheology*. 1990. p. 553-590.
68. Holmqvist, P., et al., *Crystallization kinetics of colloidal spheres under stationary shear flow.* Langmuir, 2005. **21**(24): p. 10976-10982.
69. Butler, S. and P. Harrowell, *Kinetics of crystallization in a shearing colloidal suspension*, in *Physical Review E*. 1995. p. 6424-6430.
70. Ackerson, B.J. and N.A. Clark, *Sheared colloidal suspensions*, in *Physica a-Statistical Mechanics and Its Applications*. 1983. p. 221-249.
71. Ackerson, B.J. and T.A. Morris, *Shear induced order of concentrated suspensions*, in *Better Ceramics through Chemistry Iv*. 1990. p. 159-166.
72. Ackerson, B.J., *Shear induced order in equilbrium colloidal liquids* in *Physica A*. 1991. p. 15-30.
73. Derks, D., et al., *Dynamics of colloidal crystals in shear flow.* Soft Matter, 2009. **5**(5): p. 1060-1065.
74. Gasser, U., *Crystallization in three- and two-dimensional colloidal suspensions*, in *Journal of Physics-Condensed Matter*. 2009. p. 24.
75. Cohen, I., et al., *Slip, yield, and bands in colloidal crystals under oscillatory shear.* Phys Rev Lett, 2006. **97**(21): p. 215502.
76. Derks, D., et al., *Dynamics of colloidal crystals in shear flow*, in *Soft Matter*. 2009. p. 1060-1065.
77. Ackerson, B.J. and P.N. Pusey, *Shear-induced order in suspensions of hard-spheres* Physical Review Letters, 1988. **61**(8): p. 1033-1036.
78. Davis, K.E., W.B. Russel, and W.J. Glantschnig, *Settling suspensions of colloidal silica - observations and x-ray measurements.* Journal of the Chemical Society-Faraday Transactions, 1991. **87**(3): p. 411-424.

79. Pusey, P.N. and W. Vanmegen, *Phase-behavior of concentrated suspensions of nearly hard colloidal spheres* Nature, 1986. **320**(6060): p. 340-342.
80. Solomon, T. and M.J. Solomon, *Stacking fault structure in shear-induced colloidal crystallization.* Journal of Chemical Physics, 2006. **124**(13).